Spring 2017

A Study of Reconnection Poleward of the Cusp: Cluster and Polar

Fathima M. Muzamil
University of New Hampshire, Durham

A STUDY OF RECONNECTION POLEWARD OF CUSP: CLUSTER AND POLAR

BY

FATHIMA MUZAMIL

B.S. in Mathematics and Physics, State University of New York in Plattsburgh, 2008

DISSERTATION

Submitted to the University of New Hampshire
in partial fulfillment of
the requirements for the degree of

Doctor of Philosophy

in

Physics

May, 2017

This has been examined and approved in partial fulfillment of the requirements for the degree of Doctor of Philosophy in Physics by:

Director, Charles Farrugia
Research Professor, Space Science Center

Roy Torbert
Professor, Space Science Center

Terry Forbes
Research Professor Emeritus, Space Science Center

Lynn Kistler
Professor, Space Science Center

Olof Echt
Professor, Physics Department

On May 20, 2017

Original approval signatures are on file with the University of New Hampshire Graduate School.

Dedication

To our Duddy and Mummy

Acknowledgments

Firstly, I would like to express my sincere gratitude to my advisor Dr. Farrugia. Without your support and guidance I would not have achieved this accomplishment. The time you are willing to share with any and all of your students is extraordinary. Thank you for always having an open door whenever I ran into issues and 'quick questions' that seemed like they never ended. Your jokes, your songs, and most importantly your constant motivation will always stay with me. Thank you for not letting me go off-course and get distracted by 'girlfriend problems' during my thesis writing process. Your enthusiasm for research is truly contagious and I sincerely could not have wished for a better advisor and mentor for this journey. A special mention to Mary, thank you for your positive reinforcement every time we met.

To my committee members, Dr. Roy Torbert, Dr. Terry Forbes, Dr. Lynn Kistler and Dr. Olof Echt, thank you for taking the time to read my thesis with such care. Your constructive criticisms and your insightful comments are greatly appreciated.

Thank you to all my UNH friends and colleagues in the Physics Department. Camden, Trevor, Wei, Dan Tran and Max, your friendship has truly shaped my graduate school years. Some of my best memories involve you all. I would not have survived this journey without you. Wenyuan, a special thank you to you, for always helping me out whenever I reached out. Kelly, thank you for all of the positive energy and encouragement. You are absolutely the sweetest; the best muffin maker I know. Nada and Noe, thank you for reminding me the importance of staying rooted to religion and bringing me the sense of home in NH every time we are together.

Special gratitude goes to all my best friends, Dorhani, Lahaisia, Antonette, Oscar, Angel, Frances, Rose, Ebay and Marsha. Thank you for your unwavering friendship even when I went MIA. You will always be my home away from home. Ian, thank you for always listening, and never allowing me to fall off track. Your support throughout this journey has been paramount.

Raju uncle and Sashi aunty, thank you for your continuous encouragement to achieve nothing but the best. You motivate me to push my limits. I cannot thank you enough for all of your kindness throughout these years. Mishka, my rock, our conversations always pulls me out of any and all ruts I find myself in. Thank you for always taking my side while continuing to challenge me. All my cousins, the Jaliels, the Seneviratnes, your unconditional love and support means more than you can imagine.

My cheerleader and motivational speaker, Milan Sands, I would not have gotten through this past year of thesis writing without you. I will always admire your ability to shower me with love and encouragement even when you were just as tired as I was. Thank you for always taking the street side.

And finally, last but certainly not least, thank you Mama and Dad for your constant moral and emotional support, even from continents away. Mama, thank you for allowing me to follow my goals and letting me get on that plane. Your courage and determination to always do what's best for Malli and I, and all those around you, motivates me daily. Dad, thank you for your prayers. Our conversations will always calm my nerves. Thank you for your constant reminders that some things are not always in my control. Malli, my right hand, it's an honor to be your sister. I applaud your work ethic and zest for life. Thank you for showing me the importance of being patient.

Thank you all for your encouragement and support. This accomplishment would not have been possible without you.

Table of Contents

List of Tables

List of Figures

ABSTRACT

A STUDY OF RECONNECTION POLEWARD OF CUSP: CLUSTER AND POLAR

by

Fathima Muzamil

University of New Hampshire, May, 2017

Asymmetries in plasma density and the presence of a guide field significantly alter the structure of the ion diffusion region (IDR) in symmetric, collisionless reconnection. These features have been shown by numerical simulations under moderate density asymmetries ($\sim$10), and theoretical analyses. However, very few studies have addressed these issues with in-situ observations, particularly at high magnetic latitudes. By the structure of the IDR we refer to features such as the non-colocation of the X-line and stagnation line, the distortion of the Hall magnetic and electric fields, outflow speed, outflow density etc. We have compiled a collection of Cluster crossings of the high-latitude magnetopause poleward of the cusp under northward interplanetary magnetic field in the years 2001$-$2008. We identified 18 events that fulfilled the criteria that was used as plausible evidence for an IDR crossing. A wide range of guide fields (6 to 74%) and very high density asymmetries (over three orders of magnitude) were present in this event list. The total DC electric field ranged from 10 mV/m-72 mV/m. We compared theoretical predictions for ion outflow speed and density against measured values for events with least magnetic shear and found good agreement. Peak values of both measured quantities agreed better than the average values. The separation between the X and S-lines were measured for two events. The separation was in the order of $\sim$2 ion inertial lengths.

We presented a detailed analysis of a current sheet crossing hallmarked by a density asymmetry of 2 orders of magnitude ($\sim$140) [Muzamil et al., 2014, JGR]. This event was measured by the Polar spacecraft, also at high latitudes poleward of the cusp. Data agreed well with simulation results, especially the observation of density cavities together with isolated electric fields in the normal direction at both separatrices. This has not been observed in previous observational studies.

Effect of the guide field on both sides of the X-line was examined using two events with jet reversals and similar guide fields. A sunward-tailward asymmetry in the Hall magnetic field structure was observed due to the guide field in the two outflow regions. The Hall field was weakened and changed polarity in the vicinity of the X-line due to an electron velocity shear layer. Using three other crossings with high guide fields, we measured a 40-60% enhancement in the Hall magnetic field showing consistency with simulations.

We then presented a case study of large episodic magnetic field depressions in the magnetosheath boundary layer region near the magnetic separatrix. We identified specific characteristics and compared them to possible generating mechanisms. The most plausible one was kinetic Alfvén waves.

Thus, we have provided observational evidence for the structure of the IDR in poleward of the cusp under several different asymmetric conditions and guide fields.

Chapter 1

Introduction

1.1 The Earth's Magnetosphere

Our Earth is surrounded by a region that is dominated and controlled by the terrestrial magnetic field known as the magnetosphere (MSP). Why is it sometimes that the MSP is extremely active with storms, substorms, and strong aurorae observed at low latitudes, while sometimes, the MSP is extremely calm and quiet? The geomagnetic indices (K-index), auroral electrojet index (AE index), disturbance storm time index (Dst index) for example, continuously reveal the varying geomagnetic activity of the MSP. What causes these geomagnetic disturbances in the MSP?

Plasma plays an important role in the universe, especially in these geomagnetic disturbances. Plasma is an ionized gas consisting of positively and negatively charged particles with approximately equal charge densities. Plasma exhibits collective behavior and represnts 99% of the matter in universe, including the interstellar medium. The interplanetary magnetic field (IMF) and plasma that are covected away from the Sun by the solar wind (SW), encounters the interplanetary medium which includes the Earth's MSP.

Figure 1-1 shows the various regions of the MSP and surrounding environement, that are categorized by different magnetic topology, and plasma strengths and behaviors, that are of interest to us in this thesis.

The SW is a supersonic flow with a typical speed of $\sim$ 400$-$800 km/s which may vary near the Earth. It is the interaction between the SW and the Earth's magnetic field that forms the shape of our MSP. As the SW expands, a curved shock in the shape of a bullet named the bow shock, is formed as an obstacle to the supersonic SW, by the Earth's magnetic field. At the bow shock, the solar wind slows from supersonic to subsonic velocities. The dayside terrestrial magnetic field gets compressed while the nightside MSP gets stretched out forming an elongated tail called the magnetotail. The magnetotail extends to hundreds of Earth radii (R_E).

The outer edge of the MSP closest to the Sun is the magnetopause (MP) and represents a layer in pressure balance. This is the location where the flow pressure of the SW is equal to the magnetic pressure of the MSP. The MP is a current sheet; the $\vec{J} \times \vec{B}$ force acts to deflect the SW plasma. The outermost point of the MP where the solar wind first encounters the MSP is referred to as the subsolar point. Observations have revealed that the standoff distance, i.e., the location of the MP is $\sim$10 R_E, although the location is constantly changing with changing interplanetary conditions, i.e., dynamic pressure and northward/southward component of the magnetic field (B_Z).

The magnetosheath (MSH) is the region between the bow shock and the MP that contains the shocked solar wind plasma. The plasma density typically decreases from the bow shock to the MP; however, it is always higher than the MSP plasma density. The mean and most probable density in the MSH are 34.8 cm^{-3} and 20 cm^{-3} [*Gosling*, 2007] while the typical ambient density in the MSP is $\sim$0.1 cm^{-3}. In the MSH, the SW plasma is subsonic with a typical bulk velocity of $\sim$ 250 km/s.

The region of focus in this thesis is the MP at the polar cusps, specifically poleward of the cusps in both northern and southern hemispheres. Polar cusps are the funnel shaped high latitude regions where the Earth's dipolar magnetic field fan out from the magnetic

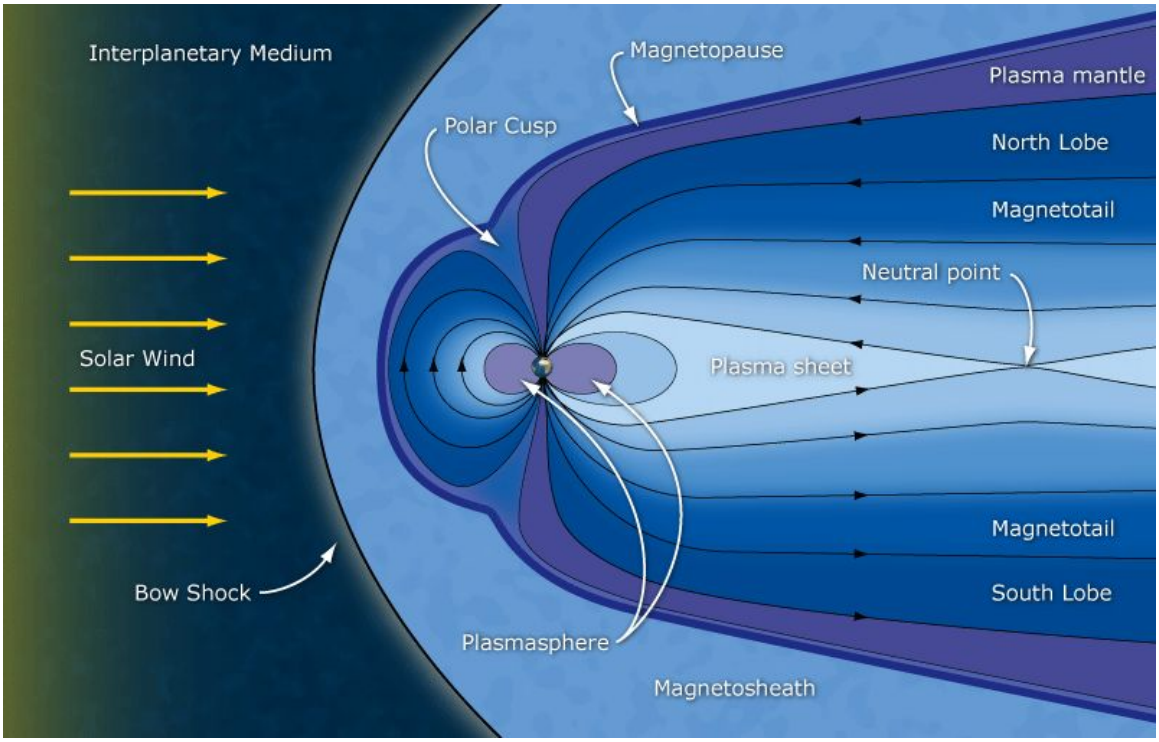

Figure 1-1: Earth's magnetosphere with the regions of interest (www.nasa.gov)

poles with a depression in magnetic field strength.

Let's get back to the cause of disturbances in the MSP. This is where the theory of magnetic reconnection takes center stage. This was a concept that was introduced by *Giovanelli* [1946] who studied explosive solar flares. Later *Hoyle*, [1949] suggested that this concept may be applicable to the MSP as well. It was James Dungey, Hoyle's student who first coined the phrase "Magnetic Reconnection" and ascribed it as the major cause of disturbances in the MSP. Oppositely directed magnetic field lines break and reconnect at a current sheet, allowing plasma transport across boundaries. This explosive process transfers the potential energy of the magnetic field to kinetic energy and heating of the plasma [*Priest and Forbes*, 2002; *Birn and Priest*, 2007]. Today, magnetic reconnection is widely accepted as a process that changes magnetic topology and is also considered as the dominant process for mass, energy and momentum transfer from the Earth's MSH to the

MSP.

As a corollary to Dungey's [1961] initial claim (Figure 1-2(a)), one expected to see disturbances in the MSP to increase when the orientation of the MSH magnetic field was opposite to that of the earth at the day side. And indeed early studies showed this, giving credence to the hypothesis that a disturbed MSP tends to occur when the IMF has a strong southward component [*Fairfield and Cahill*, 1966]. Additionaly, the fact that the orientation of the IMF determined the location of the reconnection site on the MP was for example, confirmed by *Aubry et al.*, [1970], *Gonzalez and Mozer*, [1974], *Fuselier et al.*, [2005], and *Trattner et al.*, [2007], although their ideas were different.

When the IMF is strongly northward, however, magnetic reconnection occurs poleward of the cusp. This so-called "lobe reconnection" may take place either simultaneously in both hemispheres [*Song and Russell*, 1992], or sequentially [*Cowley*, 1984; *Crooker*, 1992]. The latter is a case of open−open flux transfer. At the polar cusps, the MSH plasma has direct access to the ionosphere at both hemispheres [e.g., *Reiff et al.*, 1977; *Marklund et al.*, 1990; *Yamauchi et al.*, 1996]. This narrow region has recently "opened" or merged magnetic field lines mapping to the high-latitude ionosphere, just poleward of the last closed field line on the dayside.

Lobe reconnection was predicted at a very early stage, also by *Dungey* [1963] (Figure 1-2), and its presence was confirmed by isolated in−situ data examples [*Gosling et al.*, 1991, 1996; *Kessel et al.*, 1996; *Safrankova et al.*, 1998; *Avanov et al.*, 2001; *Phan et al.*, 2003; *Twitty et al.*, 2004, *Retino et al.*, 2005] and will be discussed later.

Reconnection at the dayside MP can occur under two models; (i) the anti-parallel merging model [*Crooker*, 1979; *Luhmann et al.*, 1984], where the shear angle of the magnetic fields on the two sides of the CS is $\sim 180^o$, and (ii) the component merging model [*Sonnerup*, 1974; *Gonzalez and Mozer*, 1974], where the shear angle is much smaller, i.e., reconnection

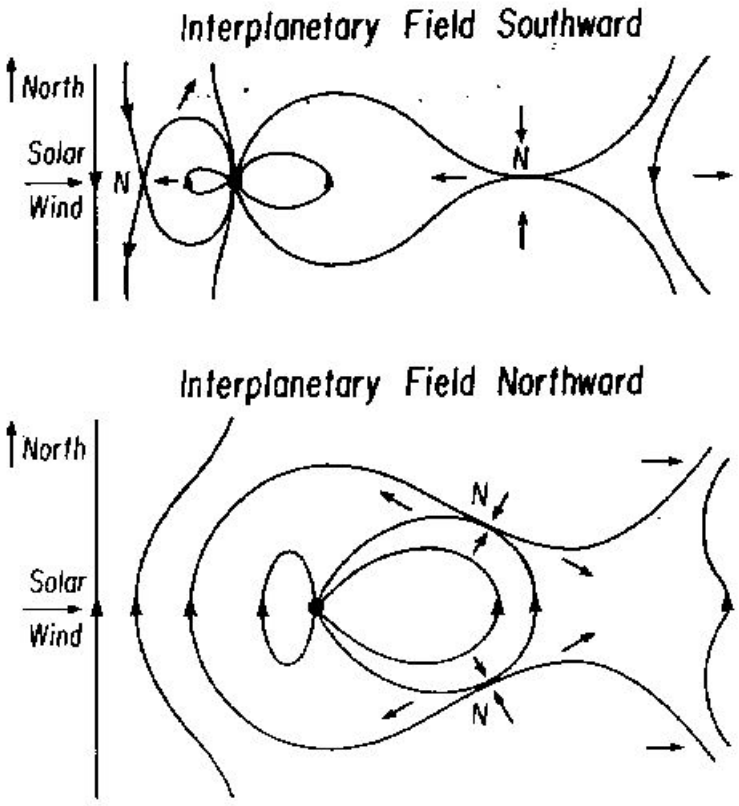

Figure 1-2: Original schematic for MP reconnection during (a) southward IMF and (b) northward IMF by *Dungey* [1961,1963]

can occur even if only one component of the MSH and MSP magnetic field is oppositely directed.

Reconnection on the dayside opens magnetic flux and erodes the dayside MSP, leading to an earthward retreat of the MP [*Aubry et al.*, 1970]. The magnetic flux is then convected into the geomagnetic tail. In the tail, open magnetic flux accumulates and the current sheet becomes thinner until reconnection convects this flux back to the dayside. This is called the "Dungey convection cycle" which depends on two sources, i.e., one on the dayside and one on the nightside.

Under southward IMF, the ionospheric convection pattern over the polar cap exhibits an *anti-sunward* convection at high latitudes, with return sunward flows at lower latitudes.

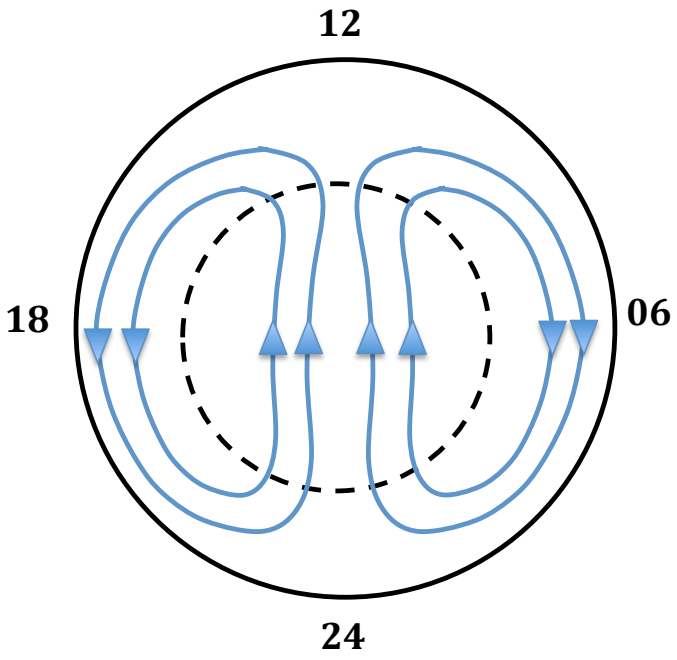

Figure 1-3: Ionospheric convection pattern over the polar cap under strictly northward IMF conditions. Dashed circle represents the polar cap boundary.

However, this pattern changes under northward IMF. Lobe reconnection drives *sunward* plasma convection over the polar cap [*Maezawa*, 1976; *Reiff*, 1982]. Hence, compared to the flow pattern under southward IMF, the direction of the ionospheric convection is reversed and is appropriately called "reverse convection" [*Crooker*, 1992]. Thus, observations of reverse convection are a direct monitor of lobe reconnection. Figure 1-3 shows an idealized two cell picture for the ionospheric convection pattern for reconnection under strictly northward IMF. Note that deviations can occur to this symmetric two cell pattern due to several different reasons which in turn causes a multiple asymmetric cell pattern [*Heelis et. al.*, 1986]. If the clock angle is not exactly -90^o, i.e., if there is an east-west component (B_Y), the two cells will not be of equal size.

Magnetic reconnection is now the widely accepted mechanism of energy release in solar flares [*Priest & Forbes*, 2002]. Reconnection has also successfully explained observations in

the solar wind [*Gosling et al.*, 2005; *Phan et al.*, 2007], the Earth's MP [*Paschmann et al.*, 1979; *Mozer et al.*, 2002], the magnetotail [*Nagai et al.*, 2001] and in laboratory plasmas [*Yamada*, 1999].

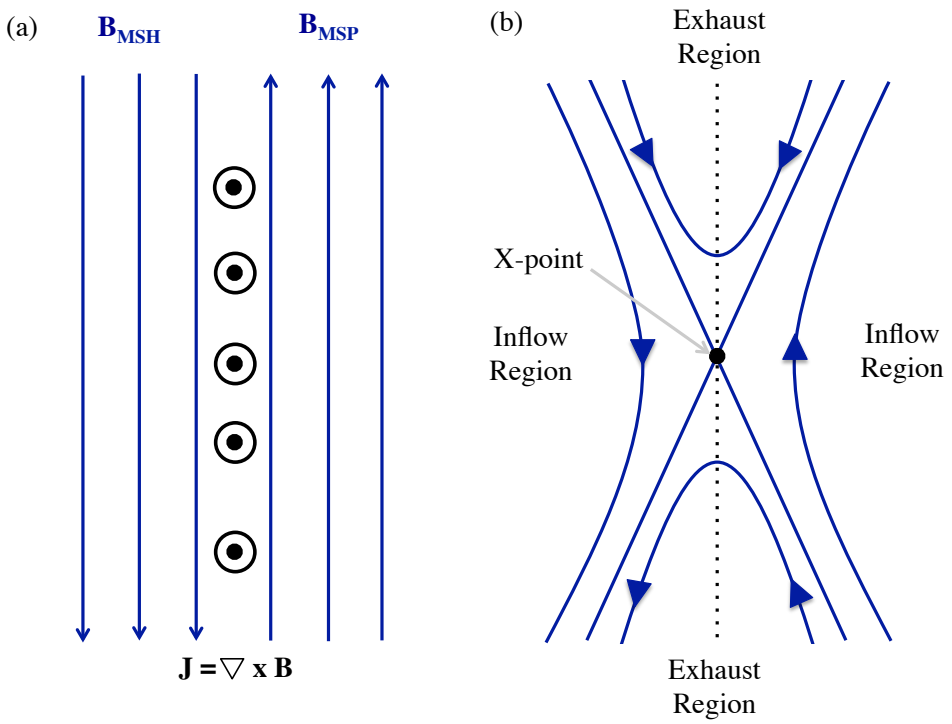

Figure 1-4: (a) Quiet current sheet. (b) Current Sheet during Reconnection

Now that we have an understanding of magnetic reconnection and its effects in a global perspective, lets now turn our attention to the local reconnection site and review briefly the basic theorectical background.

1.2 Fundamental Concepts of Magnetic Reconnection

Figure 1-4(a) shows a schematic of a quiet current sheet, such as the MP, before reconnection and Figure 1-4(b) the same current sheet during reconnection. There is a change in direction

of the magnetic field lines across the MP that creates a current, $\mathbf{J} = \nabla \times \mathbf{B}/\mu_0$ and will be directed tangentially. When reconnection occurs, the field lines convect inward and form an X−line. The stored energy of the magnetic field is converted to heat and kinetic energy of the outflow jets. The reconnected field lines are kinked and convect outwards into the exhaust region. The straightening of the bent magnetic field lines contribute to the acceleration of the outflow jets [*Parker*, 1963]. The first field line opened by reconnection is the separatrix.

The localized breakdown of the *frozen-in* condition provides us with the most general definition of magnetic reconnection [*Axford*, 1984; *Schindler et al.*, 1988; *Hesse and Schindler*, 1988; *Birn and Priest*, 2007]. Let's investigate this further by considering the electron equation of motion written in terms of the electric field $\mathbf{E}$, also known as the generalized Ohm's law [*Vasyliunas*, 1975],

$$\mathbf{E} + \mathbf{v} \times \mathbf{B} = \frac{1}{ne}\mathbf{J} \times \mathbf{B} - \frac{1}{ne}\nabla \cdot \mathbf{P}_e + \frac{m_e}{ne^2}\frac{\partial \mathbf{J}}{\partial t} + \eta \mathbf{J} \tag{1.1}$$

where $\mathbf{E}$ is the electric field, $\mathbf{v}$ is the bulk flow velocity, $\mathbf{B}$ is the magnetic field, n is the number density (which we assume equal for ions and electrons), e is the electron charge, $\mathbf{P}_e$ is the electron pressure tensor, m_e is the electron mass, and η is the resistivity.

The current density is defined as $\mathbf{J} = \nabla \times \mathbf{B}/\mu_0$. The first term on the right hand side is the Hall term, which results from the decoupling of ions and electrons and their relative motion towards the reconnection site; we will discuss this in detail in Section 1.3. Next is the electron pressure gradient, the electron inertia term, and finally the resistive term. In the electron inertia term, the electron velocity $\mathbf{v}_e$ is replaced by $-\mathbf{J}/ne$ which only becomes important at small scales where the ion bulk motion is relatively unimportant.

When the terms on the right hand side becomes negligible, we achieve ideal MHD. Ideal plasmas follow the *frozen-in* condition: $\mathbf{E} + \mathbf{v} \times \mathbf{B} = 0$. The plasma elements preserve their

magnetic connections and the field is said to be frozen to the plasma. The magnetic flux and magnetic field line connections are preserved leading to conserved magnetic topology. A region where this condition is broken, $\mathbf{E} + \mathbf{v} \times \mathbf{B} \neq 0$, is called the diffusion region (DR).

Depending on the term that dominates in the right hand side of the equation, we arrive at several reconnection models. The Sweet-Parker model [*Parker*, 1957] describes collisional MHD reconnection for 2D steady-state incompressible reconnection. In this model, for Lundquist numbers $S = \mu_0 L c_A/\eta$ below 10^4, where L is the length scale and c_A is the Alfvén velocity, the resistive term dominates. In this model, the reconnection rate is $\sim S^{-1/2}$ which was quickly found to be too slow to explain observations [*Parker,* 1963]. *Petschek* [1964] developed another MHD model, that predicted a faster reconnection rate $M_A = \pi/8lnS$. In this fluid model, the acceleration of the plasma jets could happen at two boundary layers depending on the upstream conditions; (i) at a slow shock, where the magnetic field lines are weaker, density and pressure increases or (ii) at a rotational discontinuity, where the magnetic field rotates and the flow gets faster without the change in plasma density and pressure. Additionally, Petschek's model requires a non-uniform resistivity, which becomes challenging to find evidence in observations and simulations [*Priest & Forbes*, 2002].

Resistivity is usually negligible in space plasmas which leads us to the collisionless model which incorporates the kinetic effects of plasmas. Under this model, the remaining three terms become important at various scales. The length scales associated with each term were compared to determine which term is dominant.

A comparison between the convection term $\mathbf{v} \times \mathbf{B}$ and the Hall term, $\mathbf{J} \times \mathbf{B}/ne$ revealed that the critical length scale for the Hall term to be important is the ion inertial length,

$$\begin{aligned} d_i &= \frac{c}{\omega_{pi}} \\ &= \left(\epsilon_0 m_i c^2/nq_i^2\right)^{1/2} \end{aligned} \tag{1.2}$$

where q_i is the ion charge. This quantity is also referred to as the ion skin depth. It is equivalent to the gyroradius of an ion traveling at the Alfvén speed, $d_i = c_A/\Omega_{ci}$, where $\Omega_{ci} = q_i B/m_i$ is the ion cyclotron frequency. Thus, the Hall effect alters the structure of the reconnection site, at and below ion gyro-scales [*Sonnerup*, 1979]. Furthermore, when comparing the length scales derived from ambient average value in the reconnecting region, collisionless effects become important long before collisional effects.

If reconnection has a very strong out-of-plane magnetic field, a guide field, (discussed in Section 1.5) in order to maintain the pressure balance, the Hall effect couples to the ion pressure in the momentum equation. Here the length scale becomes the ion Larmor radius, $\rho_s = c_s \Omega_{ci}$, where $c_s = [(\gamma_e k_B T_e + \gamma_i k_B T_i)/m_i]^{1/2}$ is the ion acoustic speed, γ_j is the ratio of specific heats and T_j is the temperature for species j [*Zakharov and Rogers*, 1992; *Kleva et al.*, 1995; *Rogers et al.*, 2001]. Hence, the two length scales are related by $\rho_s = (\beta/2)^{1/2} d_i$. For guide fields strengths that fall between the two extremes, there will be a smooth transition between scales ρ_s and d_i.

Let us now review the features of the so called diffusion region under symmetric reconnection.

1.3 Diffusion Region under Symmetric Conditions

Reconnection is characterized as *symmetric* when the antiparallel components of the reconnecting magnetic fields are equal, and the plasma parameters such as density and temperature have the same values on both sides of the CS. While this thesis's primary focus is on asymmetric reconnection, we start with an understanding of the features of the 2D symmetric DR, through a sketch of the widely accepted two scale structure given in Figure $1-5$.

Here, it is assumed that the field and plasma conditions (density, temperature) on either

side of the MP is the same, while the the magetic field lines on the MSH side are oppositely directed to the magetic field lines on the MSP. In the upstream/inflow region in Figure $1-5$, the inflowing plasma is frozen-in to the magetic field such that $\mathbf{E}+\mathbf{v}\times\mathbf{B}=0$. Here the electric field is dominated by the $\mathbf{v}\times\mathbf{B}$ term $(-v_X B_Z)$ which is in the $+Y$ out-of-plane direction and is called the convective electric field.

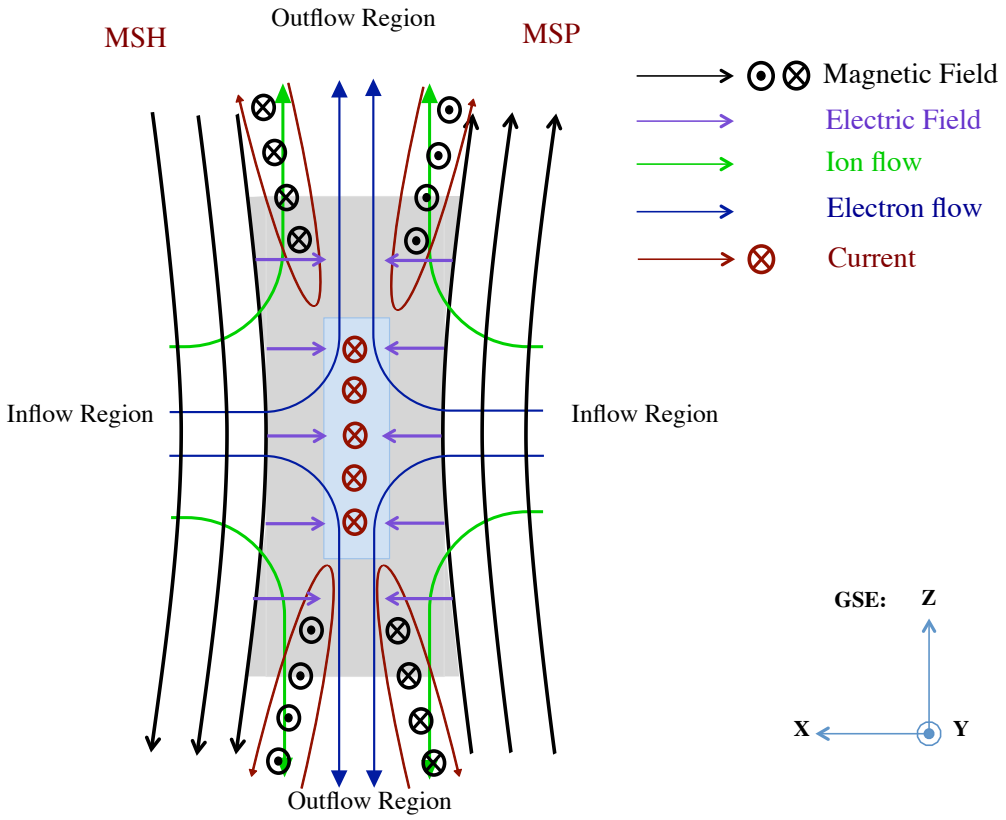

Figure 1-5: Sketch of 2D collisionless DR under symmetric reconnection. Recreated Figure 1 of *Mozer et al.,* [2002]

The flow stagnation line (S−line), where the inflow goes to zero, is also at the center of the DR.

When the ions reach a distance of their gyroradius, they decouple from the magnetic field where $\mathbf{E}+\mathbf{v_i}\times\mathbf{B}\neq 0$. Due to the much smaller mass, electrons have a much smaller gyroradius so they remain frozen to the magetic field. This region (large grey area) is

referred to as the ion diffusion region (IDR) with thickness in the order of the ion inertial length, d_i. After decoupling from the field, the ions follow a Speiser orbit [*Speiser*, 1965] with very little bulk motion while the electrons have a directed bulk flow towards the MP. With $\mathbf{J} = q_i n \mathbf{v}_i - q_i n \mathbf{v}_e$ there is a net current directed away from the MP. This is the in-plane Hall current (red curved arrows in Figure). Here, the Hall $\mathbf{J} \times \mathbf{B}/ne$ is the main contributor to the reconnection electric field. $J_X B_Z$ term creates the reconnection electric field in the $+Y$ direction (same direction of the upstream convective electric field). The ions are accelerated by the reconnection electric field, and exit the IDR at the ion Alfvén speed ($c_{A,i} = B/(\mu_0 m_i n_i)^{1/2}$).

The relative motion of the ions and electrons towards the DR give rise to in-plane current loops. This current gives rise to an out-of-place quadrupolar magetic field structure [*Sonnerup*, 1974, 1979; *Pritchett*, 2001; *Mozer* et al., 2002, and references therein]. This structure is called the Hall magnetic field structure. In addition, charge separation produces in-plane bipolar electric fields which emerge from the non-zero $J_Z B_Y$(marked by purple arrows); these are the Hall electric fields, pointing toward the CS in the ±X direction [*Shay et al.*, 1998].

Eventually, the inflowing electrons decouple from the magnetic field when they reach a distance of their gyroradius where $\mathbf{E} + \mathbf{v_e} \times \mathbf{B} \neq 0$. This region is called the electron diffusion region (EDR: blue rectagular area). This is where the magnetic field lines actually break and reconnect. The EDR has a thickness on the order of the electron inertial length, $d_e = \frac{c}{\omega_{pe}}$ where ω_{pe} is the electron plasma frequency. The EDR thickness is ∼43 times smaller than the IDR. The electrons are expelled out of the EDR at the electron Alfvén speed in the outflow direction. Ion flow is much slower than the electron flow speed in the IDR but they approach an equal speed when they exit.

Note that under symmetric upstream conditions, the X−line is colocated with the

S−line, at the center of the IDR.

Discussions in this thesis will be limited to this 2D structure, with primary focus on the characteristics of the IDR. We assume a translational symmetry in the third dimension. So far we have discussed features of the IDR under symmetric reconnection as in the case of reconnection in the magnetotail. However, as numerous observational studies show, this is not the case in reality in most other regions in the MSP.

1.4 Asymmetric Reconnection

At the dayside MP and at high latitudes poleward of the cusp, reconnection occurs between two topologically distinct regions: the cold, dense magnetosheath (MSH) on open field lines and the hot, tenuous MSP on closed field lines. The asymmetries in plasma density, temperature, field, and flow give rise to significant differences from features observed in symmetric reconnection.

To list a couple of major structural differences, (i) Hall magnetic field on the MSH side of the MP dominates the Hall magnetic field in the MSP side, $B_{H,MSH} > B_{H,MSP}$, and gives a bipolar appearance compared to the quadrupolar stucture in symmetric reconnection [*Mozer et al.*, 2008b; *Tanaka et al.*, 2008, and references therein], (ii) Hall electric field on the MSP side is stronger than the MSH side, $E_{H,MSP} > E_{H,MSH}$, [*Mozer et al.*, 2008a], (iii) the X−line is not colocated with the S−line at the center of the DR (Figure 1-6) [*Cassak and Shay*, 2007], (iv) the outflow jet is biased towards the MSP side [*Tanaka et al.*, 2008], (v) parameters such as reconnection rate, thickness of the current sheet, outflow speed and outflow density are affected [*Swisdak et al.*, 2003; *Borovsky and Hesse*, 2007; *Cassak and Shay*, 2007, 2009; *Doss et al.*, 2015]. Many of these effects have been demonstrated in particle-in-cell (PIC) simulations [e.g., *Tanaka et al.*, 2008; *Pritchett*, 2008, 2013; *Pritchett and Mozer*, 2009] and in some observations, mostly on the dayside [*Deng and Matsumoto*,

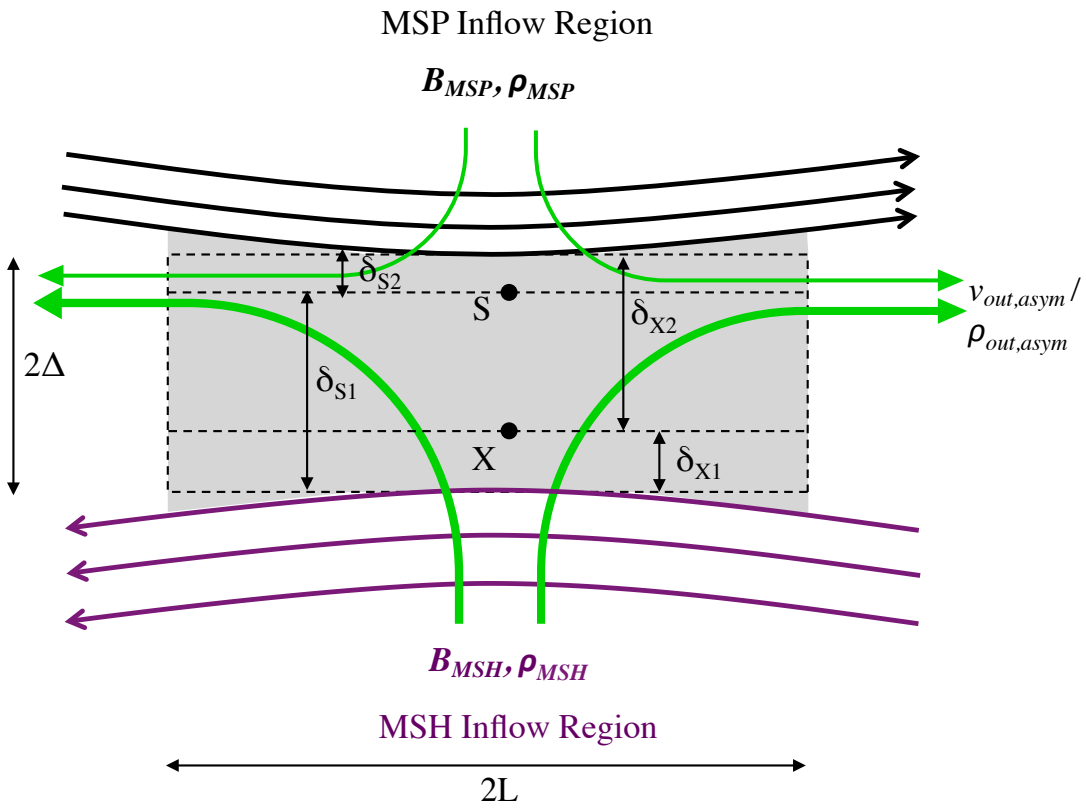

Figure 1-6: Schematic diagram of the DR during asymmetric reconnection (Recreated Figure 1 of *Cassak and Shay*, [2007])

.

2001; *Swisdak et al.*, 2003].

The seminal work of *Cassak and Shay* [2007], who performed a Sweet-Parker type analysis on the DR in the reference frame in which the X−line is stationary, motivated several efforts to understand various aspects of the structure of the DR under asymmetric conditions. They put a box around the DR with half-width Δ and half-length L (Figure 1-6) and balanced the mass, energy, and magnetic flux into and out of the box in terms of the inflowing reconnecting magnetic fields (B_{MSP}, B_{MSH}) and densities (ρ_{MSP}, ρ_{MSH}). The subscripts '1' and '2' in Figure 1-6 denote the upstream conditions of the MSH (bottom)

and MSP (top) sides of the DR respectively. Quantities describing the outflow have 'out' subscripts. The points X and S mark the X−line and the S−point, which are not colocated. The distance from the top (MSP side) and bottom (MSH side) edges of the DR to the X−line is defined as δ_{X2} and δ_{X1}, respectively. Similarly, the distances from upstream edges to the DR to the S−line is defined as δ_{S2} and δ_{S1} respectively. The green arrows indicate the velocity flow.

The scaling relations that resulted from the analysis for the outflow density ($\rho_{out,asym}$), outflow velocity ($v_{out,asym}$), and reconnection rate ($E_{0,asym}$) is as follows;

$$\rho_{out,asym} \sim \frac{(\rho_1 B_2 + \rho_2 B_1)}{(B_1 + B_2)} \tag{1.3}$$

$$v_{out,asym} = c_{A,asym} = \sqrt{\frac{B_1 B_2}{\mu_0}} \sqrt{\frac{B_1 + B_2}{\rho_1 B_2 + \rho_2 B_1}} \tag{1.4}$$

$$E_{0,asym} \sim \left(\frac{B_1 B_2}{B_1 + B_2}\right) \frac{2\Delta}{L} v_{out} \tag{1.5}$$

where Δ/L is the aspect ratio of the DR which is ∼0.1. The X−line offset scales as a ratio of the reconnecting magnetic fields, $\frac{\delta_{X2}}{\delta_{X1}} \sim \frac{B_2}{B_1}$, while the S−line offset scales as, $\frac{\delta_{S2}}{\delta_{S1}} \sim \frac{\rho_2 B_1}{\rho_1 B_2}$.

The offsets from the center of the DR imply that the greater mass density inflowing from the MSH (bottom) causes the MSH plasma to flow (green arrows) across and past the X−line before they are turned at the S−line towards the exhaust/outflow region. Thus, the S-point is displaced towards the low mass-flux (MSP) side, i.e., the side with the smaller ρ/B side. The X−line is displaced towards the high β (MSH) side. This separation reflects an earlier result by *Levy et al.* [1964] who extended Petchek's earlier analysis. Originally, *Petschek* [1964] had postulated only a slow shock to do most of the energy conversion in reconnection. In *Levy et al.* [1964], they addressed the issue as to what happens under

asymmetric density and magnetic fields. The result was that the slow shock splits into rotational discontinuity (i.e., CS) and a slow expansion fan.

The thickness of the DR under asymmetric conditions, Δ_{asym} [*Cassak and Shay*, 2009] scales as

$$\Delta_{asym} = \frac{1}{2}\left(\sqrt{\frac{B_1}{B_2}} + \sqrt{\frac{B_2}{B_1}}\right) d_{i,asym} \tag{1.6}$$

which was based on the ion inertial length,

$$d_{i,asym} = \left(\frac{m_i^2}{\mu_0 e^2 \rho_{out,asym}}\right)^{1/2} \tag{1.7}$$

This indicates that the thickness of the DR Δ_{asym}, will always be greater than or equal to $d_{i,asym}$. This is because an increase in one of the magnetic fields increases the outflow speed, which increases the gyroradius. These scaling relations apply regardless of the dissipation mechanism (collisional or collisionless). Limitations and assumptions to this theory were, (i) purely 2D analysis, (ii) reconnecting magnetic fields were anti-parallel, i.e., no guide field, (iii) no upsteam flow parallel to the reconnecting magnetic field (no velocity shear considerations) (iv) no out-of-plane bulk flow.

The theory was verified in a number of 2D simulations, with resistive MHD [*Borovsky and Hesse*, 2007; *Cassak and Shay*, 2007; *Birn et al.,* 2008], and two-fluid [*Cassak and Shay*, 2008, 2009]. Using PIC simulations under varying densities and magnetic fields, *Malakit et al.,* [2010] showed that (i) kinetic electron and proton physics beyond the Hall term does not fundamentally alter the gross properties of the asymmetric DR since $E_{0,asym}$, $v_{out,asym}$ and $\rho_{out,asym}$ showed consistency with the scaling predictions and, (ii) that the theory overpredicts the reconnection rate, $E_{0,asym}$ and outflow speed $v_{out,asym}$ by a factor of 2. *Gonzalez and Parker*, [2016] notes that this could be due to the compression effects

[*Birn et al.*, 2010] or kinetic effect in which the reconnected magnetic field preferentially heats the downstream plasma parallel to the field [*Drake et al.,* 2006; *Schoeffler et al.,* 2011]

We continue to discuss these specific structural changes of the IDR due to asymmetric upstream conditions in more detail throughout the thesis. In Sections 1.3 and 1.4, we have assumed that the reconnecting magnetic fields on the opposite sides of the CS are antiparallel. Let's now review cases when this is not so.

1.5 What is a Guide Field?

When the magnetic field lines, represented by the orange and purple lines in Figure 1-7 are not antiparallel, we decompose the magnetic field into a reconnecting component perpendicular to the X−line and a guide field component along the X−line. A detailed study of symmetric reconnection with a guide field was done by *Eastwood et al.*, [2010]. They studied a DR in the presence of a moderate guide field (20% of the reconnecting field) made by Cluster in the near earth magnetotail. Through in-situ data coupled with numerical simulations they showed that the guide field considerably distorts the pattern of the observed quadrupolar Hall fields. The Hall magnetic field perturbation was not simply superimposed on the guide field, but was asymmetric and shunted away from the current sheet.

We have established that asymmetries in density and magnetic field alter the DR structure observed in symmetric reconnection. As expected, the presence of a guide field can lead to distortions of the field and flow pattern over and above the features produced by the asymmetries and this has been analyzed via numerous studies as well [e.g., *Pritchett*, 2008; *Mozer et al.*, 2008b; *Pritchett and Mozer*, 2009; *Eastwood et al.*, 2013].

An example of this was as follows; observations by *Mozer et al.* [2008b] and the 2D PIC simulations by *Pritchett and Mozer* [2009], discussed a case of asymmetric reconnection in

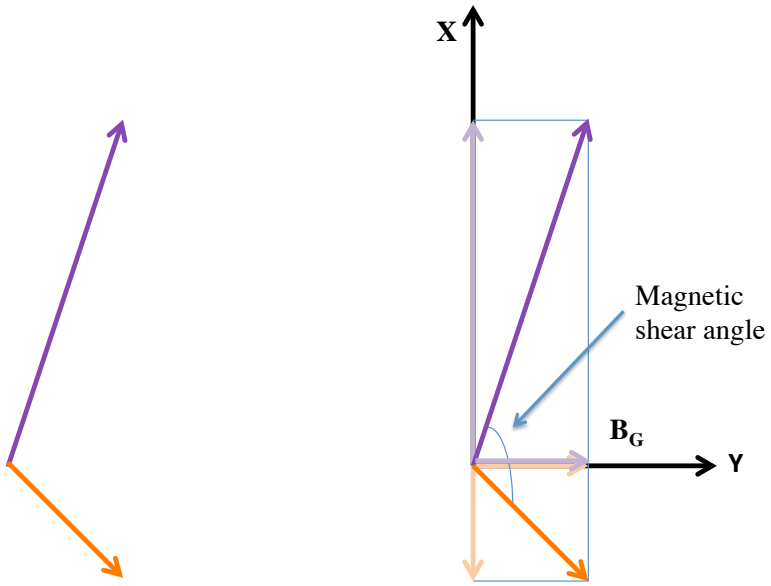

Figure 1-7: Decomposition of two magnetic field lines that are not antiparallel to obtain the guide field

the presence of a guide field, in the subsolar region. In this study, the most significant effect of the guide field was to introduce a distinct asymmetry in the bipolar Hall magnetic field structure about the X−line. We shall discuss these features further, in more detail in the following chapters.

1.6 Motivation

Currently, we have a set of theories, simulations, and fortuitous but limited set of data examples that explain how the structure reacts to different boundary conditions. In these studies, density asymmetries and guide fields are referred to as “small”, “moderate”, “large”. But what values fall under these categories? At what value of density asymmetry and guide field do the observed features in an ideal symmetric IDR start to change? How do these events compare against current theoretical scaling predictions and simulations? Are the trends observed in isolated in-situ examples representative of events poleward of the cusp?

Additionally, there is ongoing debate in the magnetic reconnection community on a rigorous definition for the DR. Over the years researchers have come up with a set of plausible criteria to identify what we currently refer to as the diffusion region. In-situ observations of such diffusion regions are not easy to come across. The spacecraft has to be in the right place at the right time and follow specific trajectories to allow examination of the different features of this comparatively small region. It gets even more complicated when investigating a structure that is strongly dependent on the boundary conditions, in this case, plasma asymmetries and the existence of a guide field.

In order to demonstrate experimentally how the features of the IDR change as a function of varying boundary conditions, we picked a region at the Earth's MP, that exhibits a wide spectrum of asymmetries between the two reconnecting regions; high latitude poleward of the cusp region. The first observation of magnetic reconnection at high latitudes were obtained only relatively recently from spacecrafts with polar orbits [eg.*Gosling et al.,* 1991; *Kessel et al.*, 1996]. Thus, only very few studies have addressed these structural features with in-situ observations. So we extend these studies through a collection of Cluster crossings under northward IMF in the years 2001-2008.

1.7 Thesis Outline

The overall goal of this study is to present and analyze data examples to arrive at an average observation-based picture of reconnection at high latitudes poleward of the cusp.

The thesis is organized as follows; Chapter 2 describes the data and instrumentation that was used in this study. A description of the coordinate system used as well as how parameters such as the density asymmetry and guide field were calculated for all events in the thesis are defined here. We also present a list of criteria that was used to identify an IDR and illustrate it via an example. Most importantly, here we present a list of events

poleward of the cusp with associated density asymmetries, magnetic field asymmetries and guide fields. From our list of events, we test predictions for outflow density and outflow velocity from *Cassak and Shay* [2007, 2009]'s theoretical study with measured values of ten events with low magnetic shear. Chaper 3 presents a detailed analysis of an event measured by the Polar spacecraft, hallmarked by a large density asymmetry [*Muzamil et al.*, 2014].

Two case studies with similar guide fields and low values of density asymmetry are used to study the effect of a guide field on the IDR in Chapter 4. These two events have jet reversals that allow us to examine and compare both sides of the X−line. This is followed by a study of three other crossings on one side of the X−line with a high guide field (greater than 60% of the reconnecting MSH field). The three events were used to examine the changes caused by the guide field on the Hall magnetic field.

In Chapter 5 we examine an interesting event that is outside the IDR and in the separatrix region which shows episodic large (90%) field depressions that are unlike other magnetic nulls observed in the MSH boundary layer. We compare the features with theories that address mangetic nulls to come to a plausible conclusion of what causes these interesting feature. We end with a summary of major results and motivation for future work in this area of research, in Chapter 6.

Chapter 2

Instrumentation and Data

2.1 Spacecraft Data

For this study, data was primarily obtained from Cluster satellite mission. For the detailed study presented in Chapter 3 data from the Polar mission was used. The intrumentation and resolution of the data used throughout the thesis are briefly introuduced in the following Section.

2.2 Cluster Mission

Cluster II satellite mission consists of four identical spacecraft named Salsa, Samba, Rumba, and Tango, also referred to as C1, C2, C3 and C4. The mission was led by ESA/NASA and was launched into a polar orbit in two stages, with the first pair reaching orbit on 16 July, 2000 and the second on 9 August, 2000. Cluster has a perigee of 4 R_E and an apogee of 19 R_E. The main goal for the Cluster mission is to study small and medium plasma structures in the range 100 km to 2-3 R_E, during the interaction between the SW and the Earth's MSP [*Escoubet et al.*, 2001]. They fly in approximate tetrahedral formation creating a three-dimensional volume that allows for the separation of spatial and temporal variations. The separation between spacecrafts ranges from 20 km$-$36,00 km [*Escoubet et al.*, 1997]. Cluster data acquisition operates in nominal mode ($\sim$ 80% of the time), but can

be switched to a high data rate (burst mode), for higher time-resolution measurements.

Each Cluster spacecraft carries 11 identical instruments, and a brief introduction to the instruments that were used for this study is as follow;

2.2.1 Instrumentation

FGM

The fluxgate magnetometer (FGM) [*Balogh et al.*, 2001] instrument consists of two triaxial magnetometers that measure the three components of the DC magnetic field. The full-resolution magnetic field data has a time resolution of 22 Hz and 67 Hz in the normal and burst modes, respectively. It has 6 ranges and resolutions according to the magnetic field features where the spacecraft are located. The largest measurement range is [-65536, 65536] nT with a resolution of ±8 nT. The time resolution for the data in this study is mostly 0.04s with units in nT.

EFW

Electric field measurements are taken from the Electric Field and Waves (EFW) instrument, which has four spherical probes on two pairs of long wire booms, which are orthogonal to each other spanning 88 m tip-to-tip [*Gustafsson et al.*, 1997]. Each axis lies in the spin plane of the spacecraft and measures the 2D electric field. Third component is calculated based on the assumption of $\mathbf{E} \cdot \mathbf{B}$=0. This reconstruction requires that B_X/B_Z and B_Y/B_Z are not too large, and that B_Z itself is not too small, so errors in E_X and E_Y are not amplified. $\mathbf{E} \cdot \mathbf{B}$=0 is an accurate assumption at most times except in the very small electron diffusion region which is not a focus of this study. The sampling rate is 25 Hz in nominal mode and 450 Hz during burst mode. Spacecraft potential measurements are also obtained from the EFW instrument, which is calculated as the potential difference between the spacecraft and

the probe, with a full resolution of 5 Hz. The time resolution for the electric field data used is 0.04 s in units mV/m.

EDI

Electron drift instrument, (EDI) has two instrument modes: "Electric Field" and "Ambient" mode [*Paschmann et al.*, 2001]. In electric field mode, electrons emitted by an electron gun drift perpendicular to the magnetic field until they are captured by the Gun Detector Units (GDUs) on the opposite side of the satellite. In ambient mode, electron counts from 0.5 keV and 1.0 keV electrons at pitch angles of 0^o, 90^o, and 180^o are measured.

PEACE

Electron moments and distributions are taken from the Plasma Electron And Current Experiment's (PEACE) [*Johnstone et al.*, 1997; *Szita et al.*, 2001]. It has two sensors: HEEA (High Energy Electron Analyser) and LEEA (Low Energy Electron Analyser). PEACE has 88 energy channels in the range of 0.6 eV−26 keV, and energy range in usage is adjusted mainly according to the spacecraft potential. Each sensor has 12 pitch angle sectors separated by 15^o. Moments and distribution functions are calculated once per spin.

CIS

Full, 3D ion distributions of the MSP are gathered by the Cluster Ion Spectrometer (CIS) [Rème et al., 1997, 2001] with two instruments; (i) The Composition and Distribution Function analyser (CODIF) that can distinguish between H+, H++, He++, and O+ ions with different mass per charge values. It has an energy range of 40 eV/e−40 keV/e and medium angular resolution of 22.5^o. (ii) Hot Ion Analyzer (HIA), is made up of 62 energy channels that has an energy range of 5eV/e−32keV/e. The Hot Ion Analyzer (HIA) instrument does not distinguish the ion species. The time resolution for the ions' full 3D distribution ranges

between 4 and 16 s. Ion moments used in this study are at a 4 s resolution. We only used data from the HIA instrument for this study.

2.2.2 Accurate density measurements in the MSP

As discussed in the introduction, the primary focus of this study is the effects of asymmetric boundary conditions on the reconnection site. The region poleward of the cusp is an ideal location to study the effects of such asymmetries since they cover a wide range. Due to the very low densities in the lobe region, HIA may not be able to obtain accurate plasma density measurments there. *Pederson et al.*, [2008] noted that variations of photoelectron emission must be included in such estimates. For electron densities in tenuous regions such as the polar cap and lobe regions, *Lybekk et al.*, [2012] deduced empricial formulas to obtain the electron density from the spacecraft potential that takes into account the photoelectron emission during the whole solar cycle. Therefore these formulas are based on the current balance between the ambient electrons travelling towards the spacecraft, and the photoelectrons emitted from the spacecraft. When the average number density recorded by HIA was below 0.5 cm^{-3}, electron density estimates were derived from the high resolution spacecraft potential measurements from the EFW instrument [*Lybekk et al.,* 2012; as done in *Wilder et al.,* 2015].

We used the N_e formulas in Table 2.1 to estimate the density using spacecraft potential measurements from the EFW instruments categorized by year. U represents the measured spacecraft potential and A and B are constants.

2.3 Coordinate system used

The minimum variance analysis (MVA) method is used in most studies to determine the boundary normal coordinates which best locates the direction of the maximum varying

Year	U (V)	Ne (EFW) = A× exp (-U/B) (cm^{-3})
2001/2002	8-12	40.0×exp(-U/3.55)
	12-30	4.3×exp(-U/10.5)
	30-50+	20.84×exp(-U/6.76)
2003/2004	8-12	30.0×exp(-U/3.83)
	12-30	3.5×exp(-U/10.5)
	30-50+	16.97×exp(-U/6.76)
2005/2006	8-11	9.0×exp(-U/4.55)
	11-17	2.8×exp(-U/8.75)
	17-30	2.03×exp(-U/10.5)
	30-50+	9.84×exp(-U/6.76)
2007/2008	8-12	Same as 2005/2006 but with A×0.8
	12-30	
	30-50+	

Table 2.1: Foumulas to estimate N_e in the low density MSP. U represents the measured spacecraft potential from EFW instrument, while A and B are constants.

magnetic field component. However, since the boundary conditions vary largely, this method is not as suitable for events under asymmetric reconnection, i.e., at the dayside MSP or the highlatitude poleward of the cusp. The normal direction is estimated incorrectly under MVA since the method forces the normal component to be constant [*Mozer et al.*, 2008b]. Therefore we rotate the data in Geocentric Solar Ecliptic (GSE) coordinates to obtain current sheet (CS) centered coordinates (LMN) by performing a cross product between the average ambient fields in the inflow MSP and MSH regions.

Here, **N** represent the direction normal to the CS, and points from the MSP to the MSH., i.e., N-axis lies along the MP normal. **L** represents the direction of the reconnecting fields, the positive direction always chosen to be tailward of the cusp, i.e., L axis lies along the MSP magnetic field lines. The **M** component complete the right handed triad in the out-of-plane direction. More details on how the coordinate system is determined is illsutrated through case study below.

2.4 Plausible evidence for an Ion Diffusion Region (IDR) crossing

Figure 2-1 portrays two ways in which a SC can enter the IDR. Spacecrafts that crosses the MP observing only one exhaust is common in most observational studies. In such cases, it becomes difficult to estimate the distance to the X−line or be certain that it is an IDR crossing. As discussed in Chapter 1, we have no rigorous definition for an IDR but have several criteria to serve as plausible evidence of an IDR crossing. The main diagnostic for entries into the IDR is when the ions do not follow the frozen-in condition $\mathbf{E} + \mathbf{v} \times \mathbf{B} \neq 0$, while the electrons do.

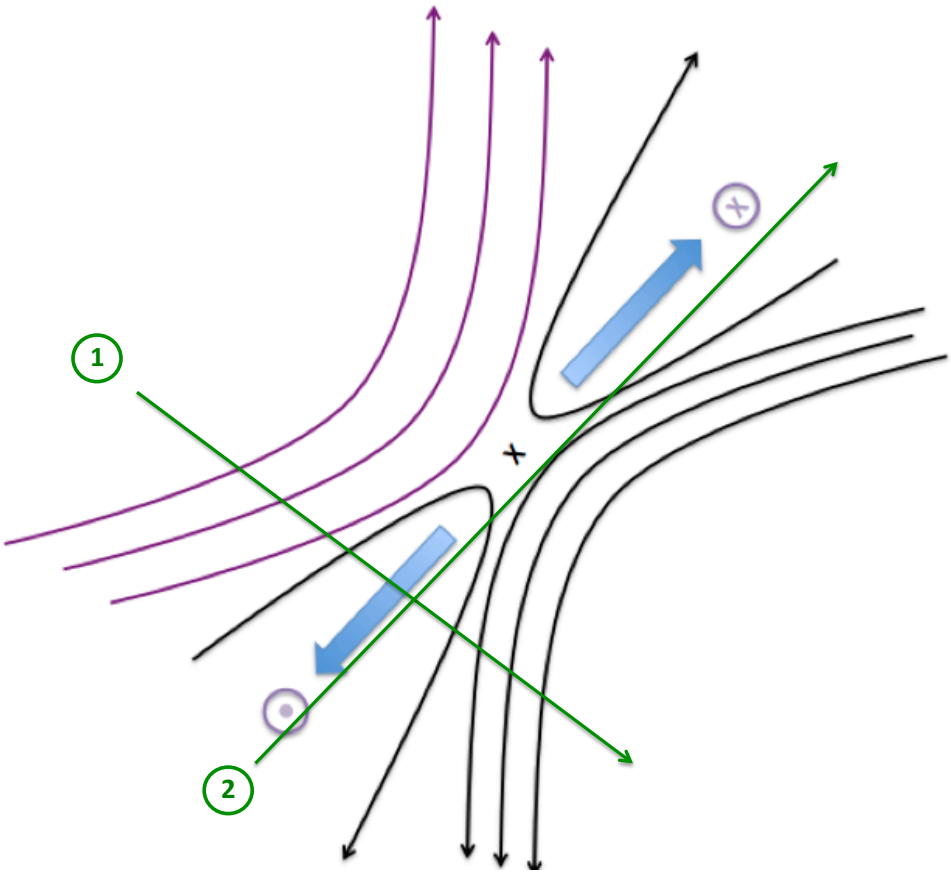

Figure 2-1: Cartoon of spacecraft crossing (i) one side of the X−line, while observing the exhaust region and (ii) from one side of the X−line to the other while observing jet reversal. Here the purple lines represent magnetic fields in the MSH while the black lines represent the magnetic field lines in the MSP. The thick blue arrows are the outflow jets.

Another diagnostic that arises from this condition, is given by the adiabatic expansion parameter, δ_i [*Scudder et al.*, 2008; see also *Maynard et. al.*, 2012]. This quantity is defined as $\delta_i \equiv \frac{|E_\perp + V_i \times B|}{w_{\perp i} B}$ where $w_{\perp i} \equiv \sqrt{2kT_{\perp i}/m_i}$ represents the mean thermal speeds of ions. Quantity δ_i is therefore the ratio of perpendicular electric to magnetic force experienced by a thermal particle in the fluid′s rest frame. If $\delta_i \ll 1$, the ions are magnetized and thus their motion is described well by the guiding center theory, and the magnetohydrodynamic (MHD) approximation to the generalized Ohm's law applies. Therefore, when $\delta_i \gtrsim 1$ at the

crossing, we assume that the ions are demagnetized from the magnetic field and conclude that the IDR has been crossed.

The presence of Hall magnetic fields, represented through the out-of-plane component B_M, deviating from the quadrupolar pattern in symmetric reconnection and portraying a bipolar pattern under asymmetric conditions is another criterion we have used in this study. The Hall electric field pointing towards the MP is another measure. However, the Hall features need to be coupled with other measurements since Hall fields have been reported to be observed far from the X−line and outside the IDR [Fujimoto et al., 1997; Nagai et al., 2001].

Eastwood et al., [2010] studied the properties of the IDR in the Earth's magnetotail. The field and plasma conditions in the inflow regions in the magnetotail vary very little compared to dayside reconnection and therefore serve as an excellent natural laboratory to study average properties of symmetric reconnection. One of the most significant signatures they noted was the total DC electric field attaining peak values of several tens of millivolts per meter (mV/m).

On the other hand, we come across a few fortuitous times where the spacecraft travels from one side of the X−line to the other, primarily implied by the observation of an outflow jet reversal. Such flow reversals in V_L, especially with no bifurcation, gives direct evidence that the spacecraft was traversing very near the X−line (Figure 2-1). The flow reversal coupled with a correlated reversal in the normal component of the magnetic field, B_N, strengthens this inference.

We now present a data example of a reconnection event poleward of the southern cusp to demonstrate how the parameters such as the density asymmetry N_{asym}, the magnetic field asymmetry B_{asym}, and the guide field B_G are defined and calculated for all events in this thesis.

2.5 Case study to show how calculations are done

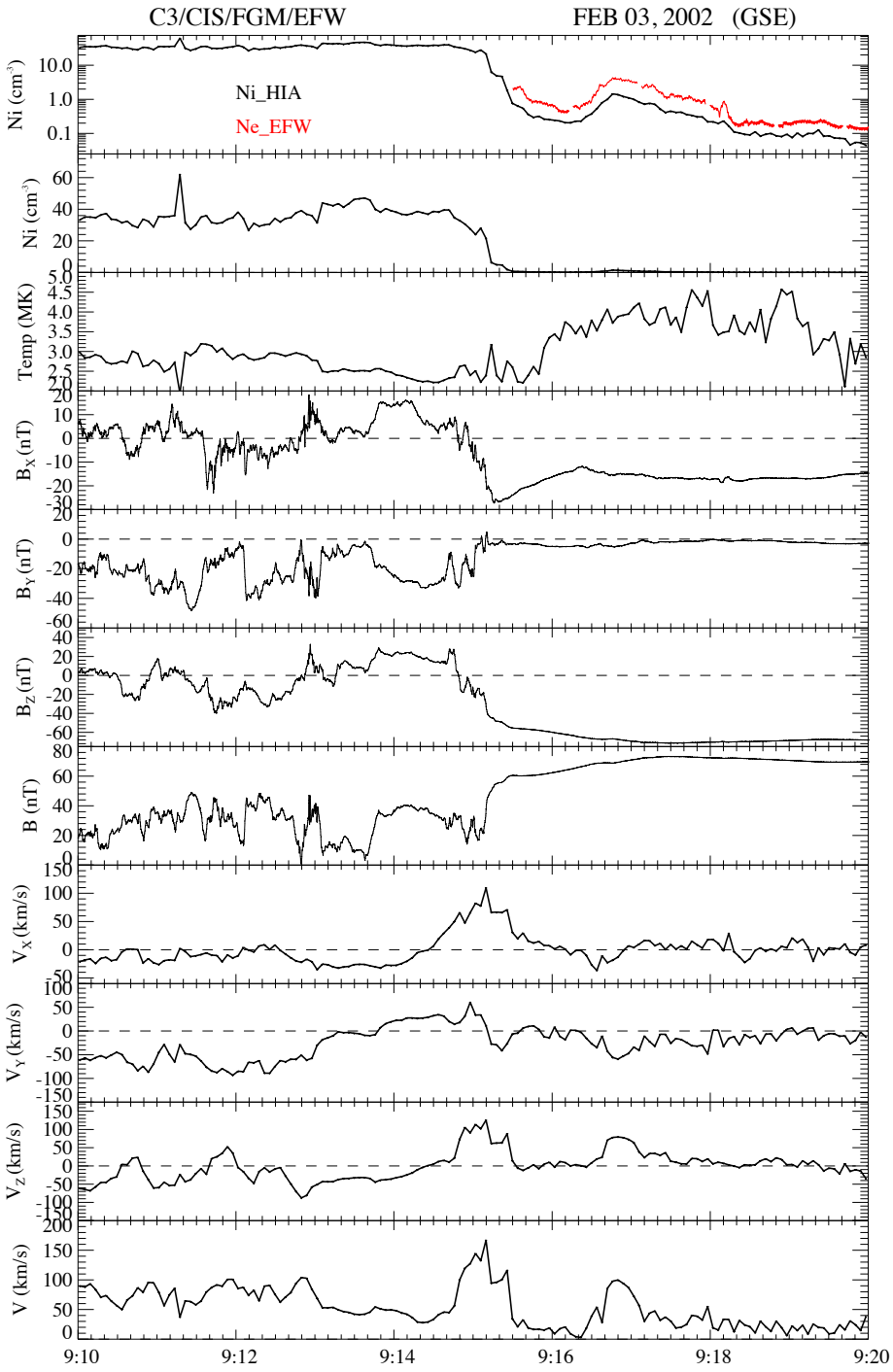

Figure 2-2: Magnetic field and plasma data from FGM and CIS instruments in GSE coordinates on February 03, 2002. Electron density derived through the spacecraft potential is overlaid in red for the low density MSP region on the first panel.

Figure 2-2 presents plasma and magnetic field measurements made by C3 on February 03, 2002 during a 10 minutue interval, 09:20−09:30 UT. The plot shows, from top to bottom, the ion density measured by CIS on a log scale (with the electron density derived through the spacecraft potential overlaid in red for the low density MSP region), ion density on a linear scale, ion temperature, XYZ components of the magnetic field in GSE coordinates and total magnetic field, the XYZ components of the ion velocity in GSE coordinates and total velocity. As discussed in Section 2.1.2, when the density measurements from CIS was less than 0.5 cm^{-3}, density derived from the spacecraft potential from the EFW instrument was used.

C3 crossed from a high density, low temperature region to a low density, high temperature region as seen in the top panel. The reversals in the B_X and B_Z components at $\sim$ 09:14:50 UT indicate that this was an inbound MP crossing. The peak in the total velocity was mainly due to the peak in the positive v_X and v_Z components, measured very near the CS crossing. The v_X component peaked at a value of 143 km/s. This may be a reconnection jet.

The coordinate system from GSE to CS-centered coordinates were rotated as follows. We obtain the CS normal $\mathbf{N}$ by forming a cross product between the ambient MSH and MSP fields, taking averages over 09:13:50−09:14:30 UT for the former and 09:16:20−09:17:20 UT for the latter. The average of the magnetic fields measured during these times intervals, $\mathbf{B_{MSH}}$ and $\mathbf{B_{MSP}}$ were used to construct the coordinate system: $\mathbf{N} = \mathbf{B_{MSH}} \times \mathbf{B_{MSP}} / |\mathbf{B_{MSH}} \times \mathbf{B_{MSP}}|$, $\mathbf{L} = \mathbf{B_{MSP}} - \mathbf{B_{MSH}} / |\mathbf{B_{MSP}} - \mathbf{B_{MSH}}|$, and $\mathbf{M} = \mathbf{N} \times \mathbf{L}$ as done in *Eastwood et al.* [2010]. In GSE coordinates, $\mathbf{L} = (-0.279, 0.247, -0.928)$ points antisunward and contains the reconnecting fields, $\mathbf{M} = (-0.179, 0.936, 0.303)$ is the out-of-plane component containing the guide field, and $\mathbf{N} = (0.943, 0.251, -0.217)$ points normal to the CS.

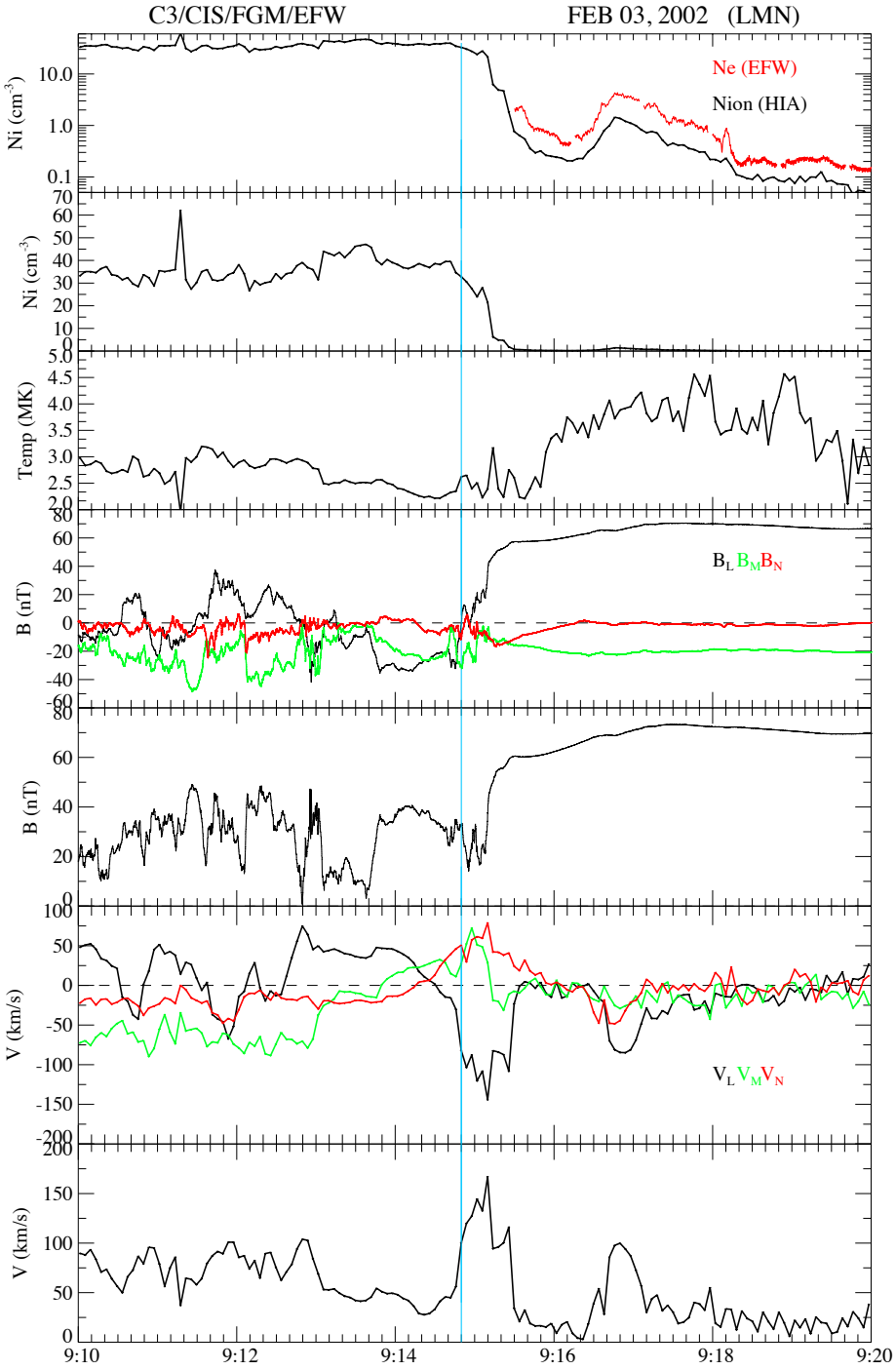

Figure 2-3: Magnetic field and plasma data from FGM and CIS instruments in LMN coordinates on February 03, 2002.

Plot of the same parameters in LMN corrdinates are presented in Figure 2-3. The

B_L reversal, marked by the blue vertical line, represents the CS crossing. This feature is also taken to represent the X−line in most asymmetric observational studies up to date [*Eastwood et al.*, 2013]. Note also the density gradient between the high density MSH side versus the low density MSP side. The midpoint of this gradient is used to represent the S−line, where the inflow velocity, v_N goes to zero. The separation between the two is an expected feature of IDR bounded by asymmetric reconnecting regions. The separation of the rotational discontinuity (B_L reversal) at the MP and the slow expansion (density gradient) was first explained as an effect of the asymmetric boundaries in a macroscopic scale by *Levy et al.*,[1964].

Tables 2.2 and 2.2 present the measured average values of the density and magnetic field in the ambient regions before and after the CS crossing. We calculate the density asymmetry as, $N_{asym} =< N_{MSH} > / < N_{MSP} >$ and magnetic field asymmetry as $B_{asym} =< B_{L,MSH} > / < B_{L,MSP} >$. Note that the average density measured by the CIS instrument was 0.82; since it's not below the condition we set we use $N_{MSP,CIS}$ to calculate the density asymmetry. This is not the case in most events studied in the thesis; we used $< N_{MSP,EFW} >$ for measurements in the MSP.

Parameter	$N_{MSH,CIS}$ (cm^{-3})	$N_{MSP,CIS}$ (cm^{-3})	$N_{MSP,EFW}$ (cm^{-3})	N_{Asym}
Value	$< 38.15 > \pm 1.20$	$< 0.82 > \pm 0.35$	$< 2.50 > \pm 1.11$	$< 46.56 > \pm 19.82$

Table 2.2: Measured density values of the ambient regions before and after the CS crossing and calculated density asymmetry.

The guide field was calculated as the average of the out-of-plane component B_M on the ambient MSH and MSP regions, $< -21.34 > \pm 4.02$ and $< -21.343 > \pm 0.94$ repectively. Hence, $B_G = < -21.34 > \pm 2.06$. This is 71% of the MSH reconnecting field, ($B_G / <$

$B_{L,MSH}$ >=71%). The percentage was calculated as conventionally done in simulation studies of asymmetric reconnection [e.g., *Pritchett and Mozer,* 2009]. The same method has been used to calculate the asymmetry for all events in this thesis.

Parameter	$B_{L,MSH}$ (nT)	$B_{L,MSP}$ (nT)	B_{Asym}
Value	$< -29.84 > \pm 3.08$	$< -66.50 > \pm 2.25$	$< 0.45 > \pm 0.05$

Table 2.3: Measured magnetic field values of the ambient regions before and after the CS crossing and calculated magnetic field asymmetry.

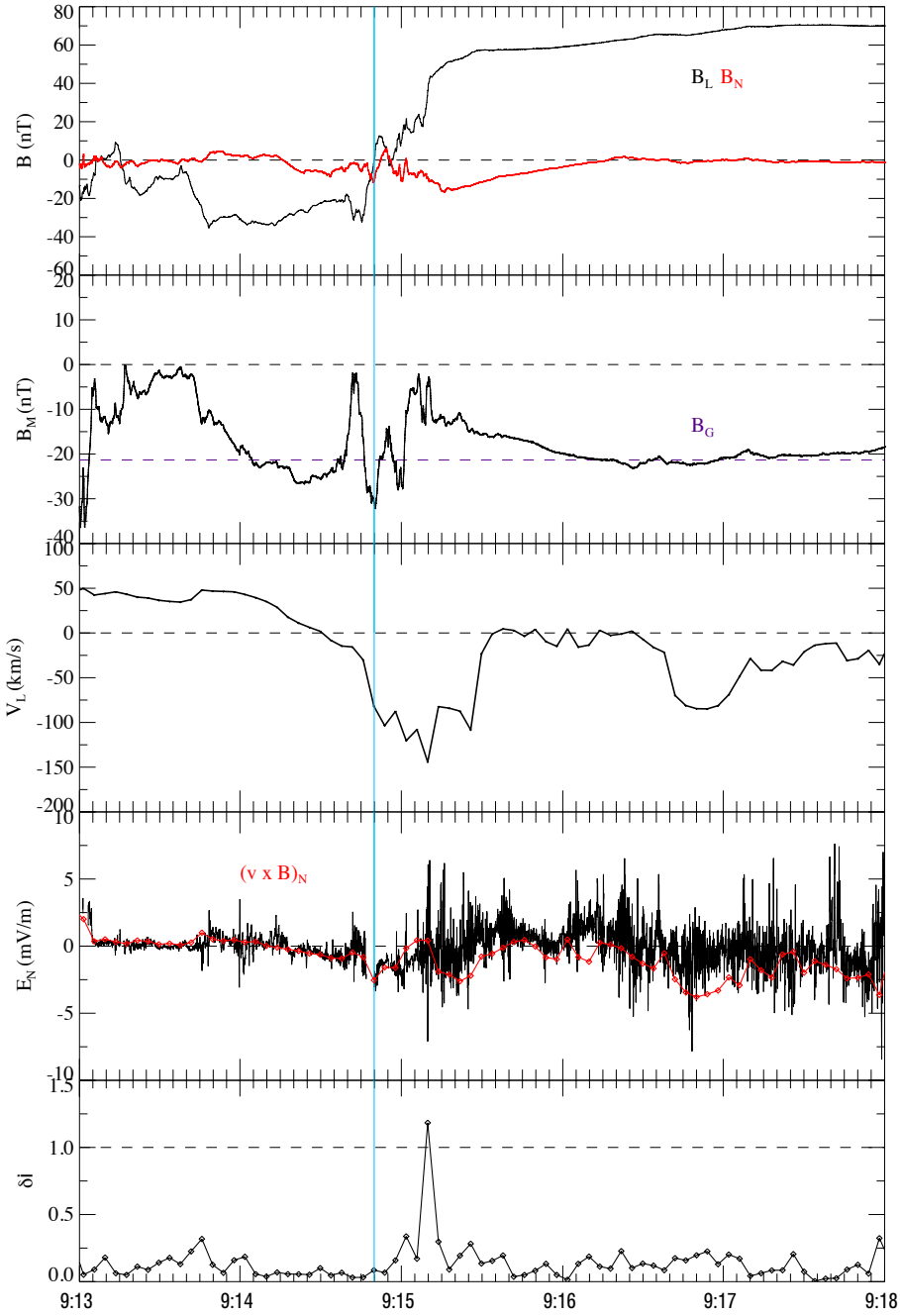

Figure 2-4: Magnetic field and plasma data from FGM and CIS instruments in LMN coordinates. The adiabatic parameter δ_i, as introduced in Section 2.7, is plotted in the last panel.

2.6 Determining spatial scales in the IDR

To study the structure of the IDR as it depends on asymmetric boundary conditions, it is essential to not just determine its normal direction but also to convert the measured time series into spatial profiles. This will aid in determining distances between specific features and the reconnection rate. In order to determine the speed of the MP, we use 2 different methods. Details of a multispacecraft (CVA) method and a single spacecraft (MFR) method is explained; a comparison of the two speeds that were obtained through the two methods are included at the end. The goal is to compare measurements of the features in the IDR, specifically, the separation between the X−line and the S−line and the reconnection rate, with the values obtained by scaling laws derived by *Cassak and Shay* [2007]. The way in which these parameters are calculated is explained using the same event.

2.6.1 Multi-Spacecraft Method

As Haaland et al., [2004] describes, multispacecraft timing methods require that a single common feature of a disconituity can be identified at four different locations and at different times when crossing the discontinuity. Identifying a common feature and time tagging this at each of the four spacecraft is therefore an essential element of timing methods.

Assuming that the orientation of the discontinuity is the same at all 4 spacecraft, a generic approach to find the velocity of the structure is as follows.

The instantaneous velocity $V(t)$, of the MP as a function of time is expressed by the following polynomial,

$$V(t) = A_0 + A_1 t + A_2 t^2 + A_3 t^3, \tag{2.1}$$

where A_i, i= 0,1,2,3 are constants to be determined from the polynomial data.Thus the

MP thickness is now, d_i,(i=0,1,2,3) is,

$$d_i = \int_{t_i-\tau_i}^{t_i+\tau_i} V(t)dt = 2\tau_i \left[V(t_i) + (A_2\tau_i^2)/3 + (A_3 t_i \tau_i^2)\right] \tag{2.2}$$

The square bracket on the right represents the average MP speed, $V_{ave,i}$, during crossing time CR_i, which has center time t_i and duration $2\tau_i$. i.e,

$$V_{ave,i} = \left[V(t_i) + (A_2\tau_i^2)/3 + (A_3 t_i \tau_i^2)\right]. \tag{2.3}$$

Distance travelled by the MP, between crossing CR_i and crossing CR0 along a fixed normal, $\boldsymbol{n}$, is then

$$\boldsymbol{R_i} \cdot \boldsymbol{n} = \int_{t=0}^{t=t_i} V(t)dt = A_0 t_i + \frac{A_1 t_i^2}{2} + \frac{A_2 t_i^3}{3} + \frac{A_3 t_i^4}{4}, \tag{2.4}$$

where $\boldsymbol{R}_i$ (i=0,1,2,3) is the position vector of the SC that experiences crossing CR$_i$ relative to the SC that encounters the first MP crossing (CR0) in the event. For simplicity, we assume $\boldsymbol{R}_i$ to be independent of time during the event.

2.6.2 Constant Velocity Approach

A method, based on timing alone, for determination of the orientation, speed and thickness of a discontinuity moving past four observing spacecraft was first presented by *Russell et al.* [1983], who applied it to interplanetary shocks. Here we review the method where we assume the velocity of the discontinuity (MP crossig) is the same at all 4 spacecraft also known as the triangulation method. So we set A_1= A_2= A_3=0 so that the MP velocity is constant during the event. Then $V(t)$= A_0. Equation (2.4) becomes

$$\boldsymbol{R_i} \cdot \boldsymbol{m} = t_i (i = 1, 2, 3) \tag{2.5}$$

where $\boldsymbol{m}$ is defined by

$$m = \frac{n}{A_0} \tag{2.6}$$

Equation 2.6 is solved for the 3 components of $\boldsymbol{m}$ and, since $|\boldsymbol{n}^2| = 1$, we get the velocity $V(t)$=A_0 =1/$|\boldsymbol{m}|$ and $\boldsymbol{n}$=$\boldsymbol{m}A_0$.

From equation 2.2, individual MP thickness is simply d_i=$2\tau_i A_0$.

2.6.3 Applying CVA Method to Case Study

We apply the CVA method to the event on February 03, 2002. Figure 2-5 shows magnetic field data for all four spacecrafts in GSE from 09:10− 09:20 UT. Note that the reversal in B_X and B_Z occur very closely in time for all 4 spacecraft. Therefore, this is an ideal event to assume constant velocity across each discontinuity and hence use the CVA method.

The MP crosses the C1, C4, C2, C3 respectively. We set the starting time t_0 to be 09:14:46.615 UT. Table 2.6.3 lists the times at which the MP crossed each spacecraft which were only a couple seconds apart. Applying the CVA method we obtained a MP velocity of v_{MP} of 45.48±3 km/s.

Spacecraft	X (GSE)	Y (GSE)	Z (GSE)	Time B_L=0(hr)
C1	32116.9	-6628.1	-52155.6	9.246282
C2	32214.7	-6614.5	-52153.4	9.247138
C3	32171.5	-6625.3	-52254.9	9.247188
C4	32208.2	-6572	-52172.6	9.247123

Table 2.4: Position (km) and time of MP crossing for each spacecraft

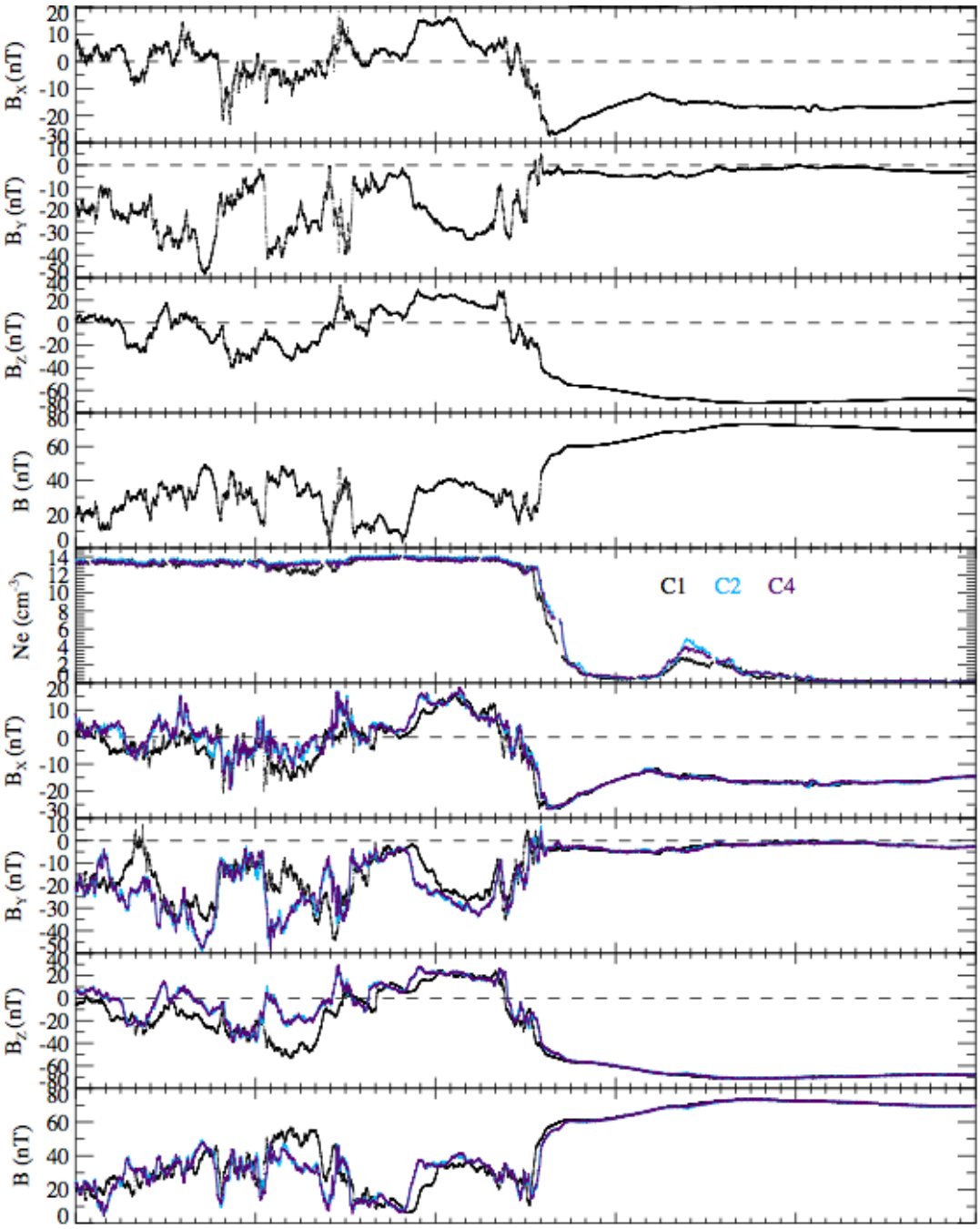

Figure 2-5: Magnetic field measurements from FGM for all 4 Cluster spacecrafts.

Recall that we took the time at which C3 crossed the MP to be 09:14:50 UT (marked by the blue vertical line) which we take to be the X−line. Time at which the density has the largest gradient 9:15:10 UT (marked by the orange vertical line) is taken to be the

stagnation point (S-point). Time between the two points is 20 seconds.

Using the average MSP value, we obtained an inertial length $d_{i,MSP}$ of 504 km. The distance between the two points are,

$$distance = t(s) \times v_{MP}(km/s) \tag{2.7}$$

We obtained a distance of 1.8 $d_{i,MSP}$ between the X−line and the S-point. The local reconnection rate R_m can be measured as $R_m = E_M = v_{in}B_{in}$. As discussed in Chapter 1, the dayside MP 'breathes' in and out, moving in the normal direction due to changing SW conditions at amplitudes larger than the inflow velocity, v_{in}. Thus, the measured v_N is a combination of the MP motion v_{MP} and the inflow velocity v_{in} as described in *Wang et al.,* [2014]. Since the plasma and magnetic field varies considerably in the MSP, we take the average of the reconnecting field in the ambient MSH, $B_{L,MSH}$ as B_{in} and substracting v_{MP} from average v_N for v_{in}. Thus,

$$\mathbf{R_m} = \mathbf{v_{in}} \times \mathbf{B_{in}} \tag{2.8}$$

yields a calculated reconnection rate of 0.61 mV/m. The predicted reconnection rate, E_{asym} from Eq. 1.5 was 0.74±0.08 mV/m.

2.7 Single Spacecraft Method: MFR

We now consider a single spacecraft method to estimate the v_{MP}; Minimization of the Faraday Residue method [*Khrabrov and Sonnerup*, 1998] as done *Wang et al.*, [2014]. This method requires that E_M is constant in the MP frame [e.g., *Mozer and Retino*, 2007]. We calculated the v_{MP} by selecting an interval across the B_L reversal region so that,

$$\sum_{\mathbf{i}}^{\mathbf{N}} \mathbf{E}'_{\mathrm{Mi}} = \sum_{\mathbf{i}}^{\mathbf{N}} (-(\tilde{\mathbf{v}}_{\mathrm{i}} - \mathbf{v}_{\mathrm{MP}}\mathbf{n}) \times \tilde{\mathbf{B}}_{\mathrm{i}})^2_{\mathrm{M}} \tag{2.9}$$

was minimized. Here, N is the number of data points in the interval selected and M is the out-of-plane direction. We need, $\frac{\partial \sum E'^2_{Mi}}{\partial v_{MP}} = 0$.

Thus, $\mathbf{v}_{\mathrm{MP}}$ becomes,

$$\mathbf{v}_{\mathrm{MP}} = -\frac{\sum_{\mathbf{i}}^{\mathbf{N}} (\mathbf{E}_{\mathrm{Mi}}\mathbf{B}_{\mathrm{Li}}) - \frac{1}{\mathrm{N}} \sum_{\mathbf{i}}^{\mathbf{N}} \mathbf{E}_{\mathrm{Mi}} \sum_{\mathbf{i}}^{\mathbf{N}} \mathbf{B}_{\mathrm{Li}}}{\sum_{\mathbf{i}}^{\mathbf{N}} \mathbf{B}^{\mathbf{2}}_{\mathrm{Li}} - \frac{1}{\mathrm{N}} (\sum_{\mathbf{i}}^{\mathbf{N}} \mathbf{B}_{\mathrm{Li}})^2} \tag{2.10}$$

This equation is similiar to MFR method except that the normal direction is predetermined as described above. The negative value for the MP velocity for crossings from MSP to MSH (outbound crossings) and positive for crossings from crossings from MSH to MSP. *Wang et al.*, [2014] obtained the electric field E_M component from $-\vec{v} \times \vec{B}$ using H^+ velocity from CODIF instrument while for this event we used the ion velocity from HIA measurements.

We obtained the velocity of the MP, V_{MP} of 32.12 km/s from the single spacecraft, MFR method. This gave a reconnection rate of 0.33 mV/m.

2.8 Table of Events

Unlike simulations, it becomes challenging to find an event when only one boundary condition is different from the symmetric case to isolate it's effect on the structure of the DR. Each individual event must be studied in detail to understand the structural changes due to the various boundary conditions. Here, we present a table 18 IDR crossings made by Cluster, with the associated density asymmetry, N_{asym}, B_{asym}, and the guide field as a percentage of the reconnecting MSH field, B_G, as calculated in the case study above. If the event satisfies the adiabatic expansion parameter δ_i at the CS crossing, and the magnitude of the total electric field is also included to showcase the different criteria that was fulfilled.

Event #	Date	N_{asym}	B_{asym}	B_G (%)	δ criteria satisfied at MP	E_{tot} (mV/m)
1	Apr 21, 2001	$< 185.74 > \pm 46.53$	$< 0.43 > \pm 0.14$	$< 15.76 > \pm 3.71$ (30%)	Yes	23 mV/m
2	Dec 3, 2001	$< 18.09 > \pm 13.27$	$< 0..61 > \pm 0.13$	$< 22.95 > \pm 3.27$ (74%)	Yes	25 mV/m
3	Dec 3, 2001	$< 32.70 > \pm 17.90$	$< 0.73 > \pm 0.08$	$< 8.26 > \pm 5.8$ (21%)	Yes	18 mV/m
4	Feb 3, 2002	$< 46.56 > \pm 19.82$	$< 0.45 > \pm 0.05$	$< 21.34 > \pm 2.06$ (72%)	Yes	8 mV/m
5	Mar 18, 2002	$< 754.30 > \pm 100.94$	$< 0.56 > \pm 0.10$	$< -5.91 > \pm 2.74$ (6%)	No	60 mV/m
6	Apr 10, 2002	$< 99.53 > \pm 12.13$	$< 0.78 > \pm 0.03$	$< -14..35 > 1.20$ (30%)	Yes	22 mV/m
7	Mar 5, 2004	$< 12.9 > \pm 2.48$	$< 0.28 > \pm 0.15$	$< -19.08 > \pm 1.55$ (19%)	No	16 mV/m
8	Mar 8, 2004	$< 759.45 > \pm 280.05$	$< 0.75 > \pm 0.07$	$< 15.69 > \pm 2.08$ (46%)	Yes	13 mV/m
9	Mar 10, 2004	$< 19.81 > \pm 4.0$	$< 0.54 > \pm 0.08$	$< -11.21 > \pm 1.54$ (28%)	No	33 mV/m
10	Nov 9, 2004	$< 201.10 > \pm 14.37$	$< 0.82 > \pm 0.17$	$< -13.69 > \pm$ (12%)	No	66 mV/m
11	Jan 17, 2005	$< 40.89 > \pm 19.64$	$< 0.55 > \pm 0.15$	$< 43.63 > \pm 8.45$ (58%)	Yes	72 mV/m
12	Mar 23, 2005	$< 5.37 > \pm 0.89$	$< 0.97 > \pm 0.07$	$< 8.13 > \pm 2.04$ (17%)	Yes	20 mV/m
13	Nov 19, 2005	$< 63.48 > \pm 14.08$	$< 0.96 > \pm .12$	$< -23.16 > \pm 8.42$ (33%)	No	24 mV/m
14	Dec 22, 2005	$< 81.08 > \pm 12.2$	$< 0.81 > \pm .13$	$< 10.12 > \pm 3.67$ (17%)	Yes	26 mV/m
15	Feb 05, 2006	$< 1234.59 > \pm 320$	$< 0.61 > \pm 0.21$	$< -12.35 > \pm$ (26%)	No	N/A
16	Apr 12, 2007	$< 8.59 > \pm 3.7$	$< 0.48 > \pm 0.15$	$< -12.85 > \pm 2.77$ (62%)	Yes	31 mV/m
17	May 4, 2008	$< 56.65 > \pm 21.18$	$< 0.67 > \pm 0.12$	$< 4.11 > \pm 1.40$ (14%)	Yes	13 mV/m
18	Apr 3, 2008	$< 25.47 > \pm 3.23$	$< 0.58 > \pm 0.04$	$< 0.82 > \pm 1.46$ (4%)	Yes	18 mV/m

Table 2.5: Poleward of the cusp crossings with associated density asymmetries N_{asym}, magnetic field asymmetries, B_{asym}, guide field and percentage with respect to $B_{L,MSH}$, if the adiabatic parameter, δ_i criteria is satisfied, and the total electric field E_{tot} at the crossing.

2.8.1 Summary

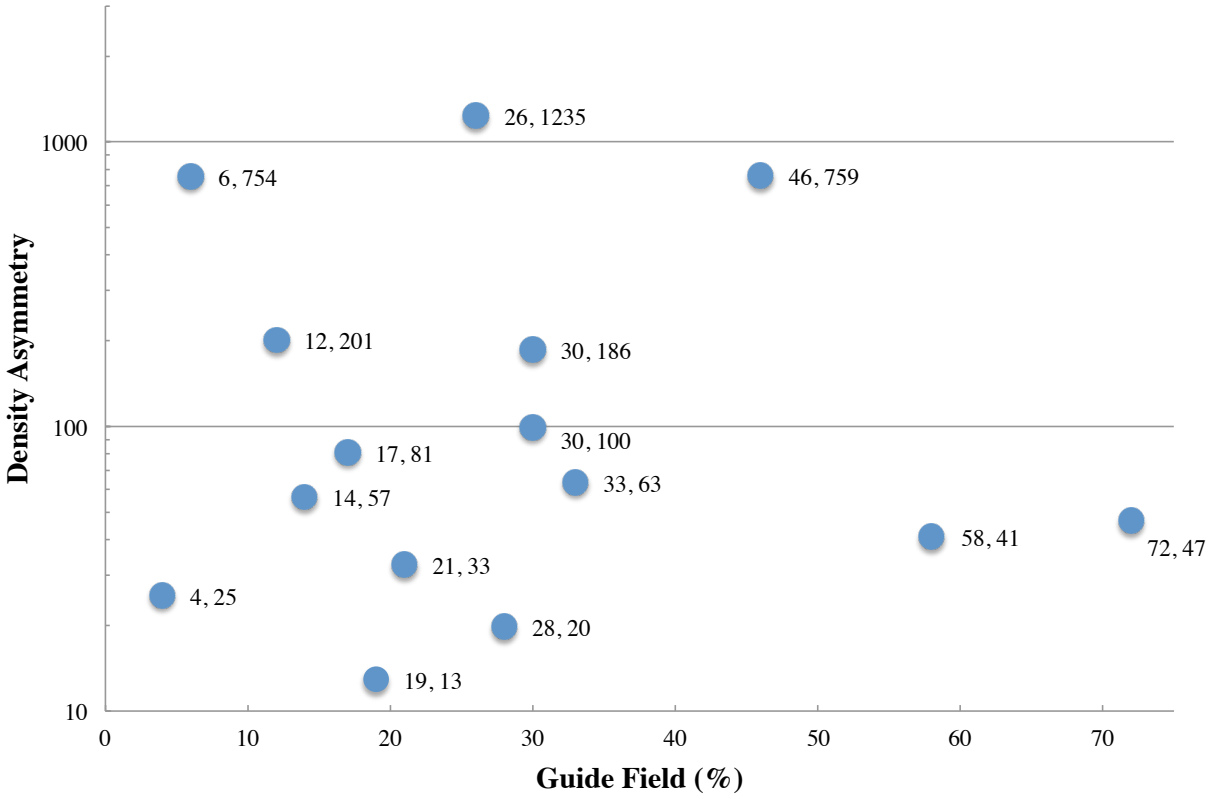

Figure 2-6: Guide Field vs. N_{asym} for 18 Cluster events

The plot of guide fields vs. density asymmetries (Figure 2-6) show that the event list spans a wide range of values; density asymmetries range from values of 1 order of magnitude to over 3 orders of magnitude, while the guide field ranges from 6−74%. With this list, we are able to pick out example events to study the effect of (i) N_{asym} for events with low guide fields, (ii) N_{asym} for events with large guide fields and (iii) effect of a guide field on events with similar N_{asym}.

We now compare observations which depend on asymmetry in plasma density and reconnecting magnetc fields with theoretical predictions. Specifically, we shall compare the measured outflow speed and outflow density to the predictions of *Cassak and Shay*, [2007,

2009] who derived scaling laws by performing Sweet-Parker type analysis for antiparallel reconnecting fields as discussed in Section 1.4. By considering the upstream magnetic field strengths B_{MSH} and B_{MSP} and the upstream mass densities ρ_{MSH} and ρ_{MSP}, the scaling relation for asymmetric outflow density $\rho_{out,asym}$ and velocity $v_{out,asym}$ was,

$$\rho_{out} \sim (\rho_{MSH}B_{MSH} + \rho_{MSP}B_{MSP})/(B_{MSH} + B_{MSP}) \tag{2.11}$$

and

$$v_{out,asym} = \sqrt{\frac{B_{MSH}B_{MSP}}{\mu_0}}\sqrt{\frac{B_{MSH} + B_{MSP}}{\rho_{MSH}B_{MSP} + \rho_{MSP}B_{MSH}}} \tag{2.12}$$

Cassak and Shay, [2007, 2009]'s scaling relations were derived with anti-parallel reconnecting magnetic fields, i.e., magnetic shear was 180^o. Hence, from Table 2.5 we chose IDR crossings with shear angle between the inflow magnetic field on two sides greater than 150^o degrees for this comparison. Predicted values were calculated using average values of the ambient reconnecting regions (Table 2.5).

Table 2.6 presents measured parameters of ten events with the magnetic shear angle, predicted outflow density $n_{out,asym}$, peak density measured during the outflow jet $n_{obs,peak}$, average of the density measured during the outflow jet $n_{obs,avg}$ with standard deviations, predicted outflow speed $v_{out,asym}$, peak speed of the measured outflow jet $n_{obs,peak}$, average speed of the measured outflow jet $n_{obs,avg}$ with standard deviations.

Predicted outflow density values are plotted against measured in the following Figure 2-7. Data points in blue represent the peak values while data points in red represent the measured average values. The error bars on the red data points represent the standard deviations.

Date		Magnetic Shear Angle	$n_{out,asym}$ cm^{-3}	$n_{obs,peak}$ cm^{-3}	$n_{obs,avg}$ cm^{-3}	$v_{out,asym}$ km/s	$\|v_{obs,peak}\|$ km/s	$\|v_{obs,avg}\|$ km/s
Apr 21, 2001		155.66^o	18.19	11.6	$< 9.0 > \pm 2.39$	195.48	281.29	$< 232.61 > \pm 28.31$
Dec 03, 2001	Jet #1	159.61^o	10.78	2.27	$< .99 > \pm .92$	308.92	266.8	$< 181.54 > \pm 41.68$
	Jet #2			10.55	$< 9 > \pm 1.5$		528.02	$< 442.7 > \pm 80.07$
Mar 18, 2002		174.34^o	71.03	48.02	$< 38.22 > \pm 13.73$	322.92	327.7	$< 287 > \pm 44.54$
Mar 10, 2004		156.01^o	9.2	10.55	$< 8.29 > \pm 2.62$	417.3	364.06	$< 210 > \pm 74.77$
Nov 9, 2004		155.55^o	4.31	3.21	$< 2.13 > \pm .75$	311.83	297.31	$< 258.64 > \pm 29.61$
Mar 23, 2005		160.75^o	9.48	15.08	$< 12.29 > \pm 2.62$	281.29	360.86	$< 297.84 > \pm 42.71$
Dec 22, 2005		162.35^o	8.85	7.85	$< 6.31 > \pm 2.38$	302.43	265.045	$< 201.041 > \pm 63.92$
Feb 5, 2006		156.23^o	29.06	37.33	$< 25.37 > \pm 4.61$	244.47	257.126	$< 190.841 > \pm 48.41$
May 4, 2008	Jet #1	166.75^o	4.42	5.85	$< 4.67 > \pm .98$	374.96	190.94	$< 165.19 > \pm 28$
	Jet #2			6.19	$< 3.95 > \pm 1.84$		377.14	$< 227.6 > \pm 86.49$
Apr 3, 2008	Jet #1	159.22^o	9.48	13.78	$< 7.99 > \pm 5.21$	204.71	205.12	$< 158.28 > \pm 33.48$
	Jet #2			9.81	$< 4.72 > \pm 2.63$		170.67	$< 145.53 > \pm 14.09$

Table 2.6: Ten events with magnetic shear greater than 150^o with associated $n_{out,asym}$, $n_{obs,peak}$, $n_{obs,avg}$, $v_{out,asym}$, $v_{obs,peak}$, $v_{obs,avg}$

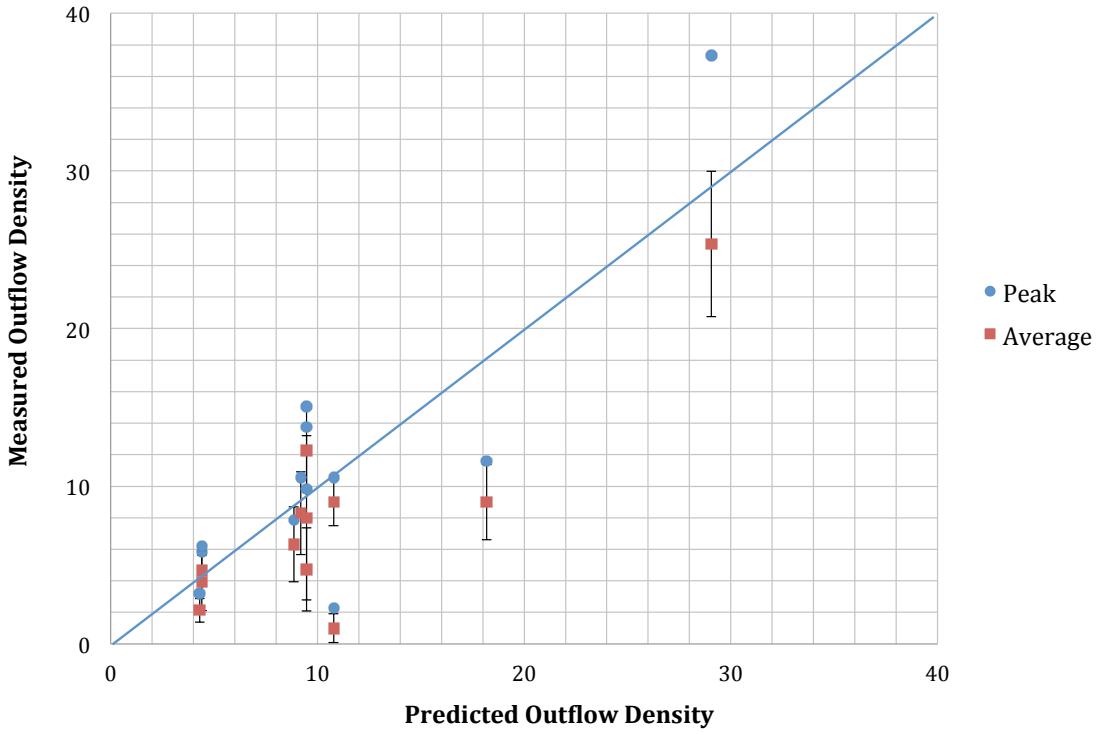

Figure 2-7: Predicted outflow density against measured values. Blue data points represents peak values while the red data points represents the average values.

Measured peak values of the outflow density $n_{obs,peak}$ matched well with predicted values. Average values of the density fell below predicted values. Similarly, we plotted predictions against measured values of the outflow velocity in Figure 2-8. For events with jet reversals, the jet with the lower speed is marked in yellow.

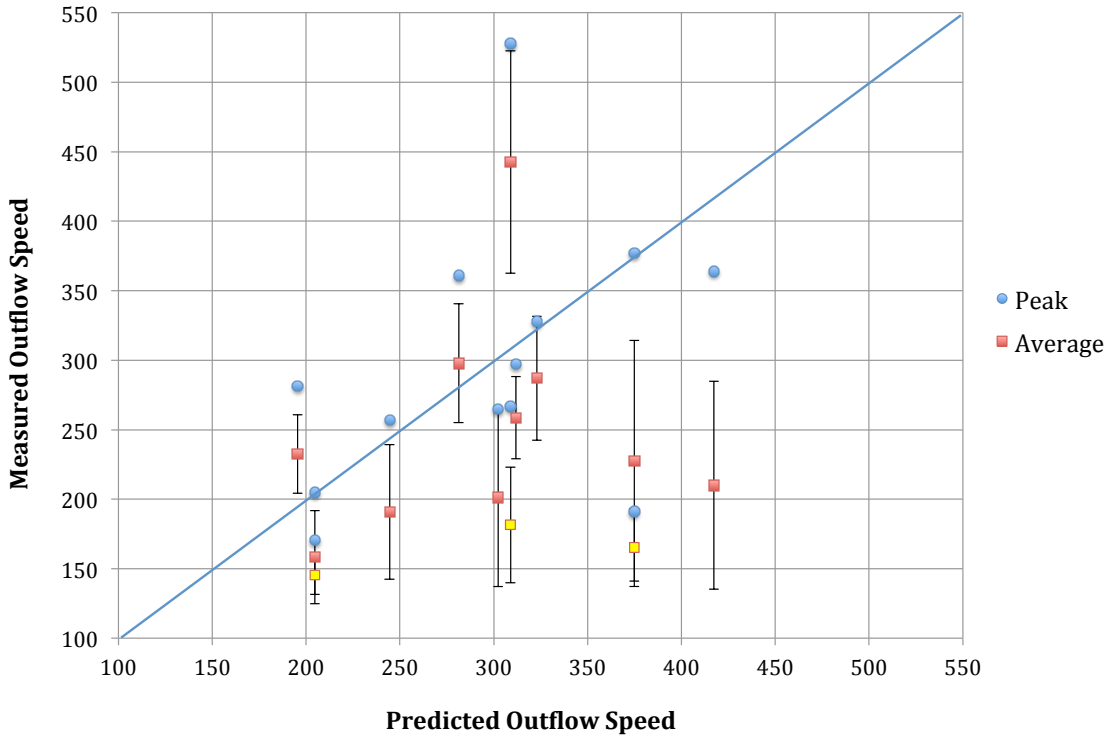

Figure 2-8: Predicted outflow velocity against measured values. Blue data points represents peak values while the red data points represents the average values. For events with jet reversals, jets with lower speeds are marked in yellow.

We note that *Cassak and Shay*, [2007, 2009]'s predicted the outflow of a jet with the implicit assumption that both outflow jets were the same. However, as we see in above Figure 2-8, in cases with jet reversals, the predictions agree better with the higher speed jet.

We continue to investigate individual events from Table 2.5 in detail throughout the thesis.

Chapter 3

Case Study: Large Density Asymmetry

3.1 Introduction

In this chapter we document several crossings of a reconnection layer poleward of the cusp made by the Polar spacecraft on 11 April 1997. These are meant to complement and extend other *in situ* high latitude observations under asymmetric conditions for a new domain of parameters. The event we study has various noteworthy features that have not been reported before. Namely, (1) the IMF was strong (20 nT) and pointed steadily and strongly northward (B_z ∼20 nT) without interruption for 13 hours (average clock angle was $\sim 20^0$). An event with such extreme interplanetary parameters has not been studied before in this context. (2) There was a huge asymmetry in the density ($N_{MSH}/N_{MSP} \approx 140$). (3) When the *in situ* observations started, the IMF had been northward-pointing for 6 hours. Thus we are in the middle of a continuous lobe reconnection process. This is further verified, albeit in snapshot fashion, by the DMSP F13 satellite dusk-dawn passes over the northern polar cap. Reverse convection was observed on all passes. Polar is thus seeing a "mature" reconnection layer. Besides the huge density asymmetry, the traversal of the reconnection layer occured under an asymmetry in temperature ($T_{MSH}/T_{MSP} = 0.38$) and small asymmetry in the

magnetic field ($B_{MSH}/B_{MSP} = 0.85$). The shear between the ambient fields was $\sim 155^0$, comparable in magnitude to the event reported by *Retinò et al.,* [2005]. In view of the large density asymmetry we compare our observations with the simulations of *Tanaka et al.*, [2008].

Then we also consider the effects of the guide field on the structure of the reconnection layer by comparing our observations with PIC simulations of asymmetric reconnection in the presence of a guide field [*Pritchett and Mozer*, 2009]. As noted, the guide field is expected to alter the Hall magnetic and electric field configurations and cause additional asymmetries north and south of the X−line.

The layout of this chapter is as follows. Section (3.2) gives an overview of the interplanetary conditions using data acquired by the Wind spacecraft. In section (3.3), we present typical DMSP F13 observations over the northern polar cap. Section (3.4) gives an overview of the *in situ* data of multiple entries into the reconnection layer. This is followed by a detailed study of one event, a complete inbound crossing. The effects of the guide field on the Hall magnetic and electric field structures as well as the electron behavior are considered in section (3.5). We end with a summary and a discussion in section (3.6).

3.2 Interplanetary Observations: WIND

Figure 3-1 shows interplanetary plasma and magnetic field data from the Solar Wind Experiment (SWE) [*Ogilvie et al.,* 1995] and Magnetic Field Investigation (MFI) [*Lepping et al.,* 1995] on spacecraft Wind for the interval 4−20 UT, 11 April 1997. The plasma data are at ∼90 s and magnetic field data are at 3 s temporal resolution. From top to bottom, the panels display the proton density (α particle-to-proton number density ratio in percent in red with the scale on the right), bulk speed, temperature (the proton temperature in black, electron temperature in blue, and the expected proton temperature from the statisti-

cal analysis of *Lopez,* [1987] in red), pressure (proton pressure in black, electron pressure in blue and the magnetic pressure in green), dynamic pressure (including the α particle contribution), the components of the magnetic field in Geocentric Solar Magnetospheric System (GSM) coordinates, total magnetic field strength, proton β, and the IMF clock angle, i.e., the polar angle in the GSM YZ plane.

Wind was at an ideal location to monitor the effects on the terrestrial MSP, because it was upstream of Earth and close to the Sun-Earth line. At 12 UT, it was located at (230, 8, 22) R_E in GSE coordinates. With an average speed of 450 km/s, the convection delay time to the subsolar MP can be estimated as $\sim$ 53 minutes.

Wind was observing an interplanetary coronal mass ejection (ICME). The blue vertical lines show the estimates of the ICME boundaries, 6−19 UT as identified by *Richardson and Cane* [2010]. This transient was identified among other features by a strong magnetic field, low proton β, and high values of density ratio (α/p). The interval between the red lines is our identification of a magnetic cloud (MC) embedded in the ICME. The leading edge of the MC is located at the time when the proton temperature falls below the expected temperature while the trailing edge is drawn at the time when the proton temperature recovers and the magnetic field direction becomes variable. Defining characteristics of a MC are a strong magnetic field (average $\sim$18 nT), a large and smooth rotation in the field vector and a low proton temperature with respect to expected values [*Lopez*, 1987], and low proton β.

There are three major features that are of interest to us: the dynamic pressure profile (panel 5), the magnetic field behavior, and the clock angle. The dynamic pressure was high, well above typical values at 1 AU (of the order of $\sim$2.2 nPa). It was also very variable, ranging from 2.5 nPa to 15 nPa. Note the sharp dynamic pressure drop from 14 nPa to $\sim$4 nPa at 14 UT. Adding the 53 or so minutes convection delay to this, we would expect

the MP to experience a sudden inflation at around 14:53 UT. Correspondingly, any *in situ* measurements being made at the MP would be expected to cease abruptly at this time. We have a strong magnetic field, with values reaching over 20 nT. IMF B_z was the dominant component and it stayed strongly positive for 13 hours. IMF B_y was more variable: it is mainly negative until 14 UT and mainly positive afterwards. With an average clock angle of $\sim 20^0$ throughout this interval, this is a case of a strong field pointing strongly northward for 13 hours.

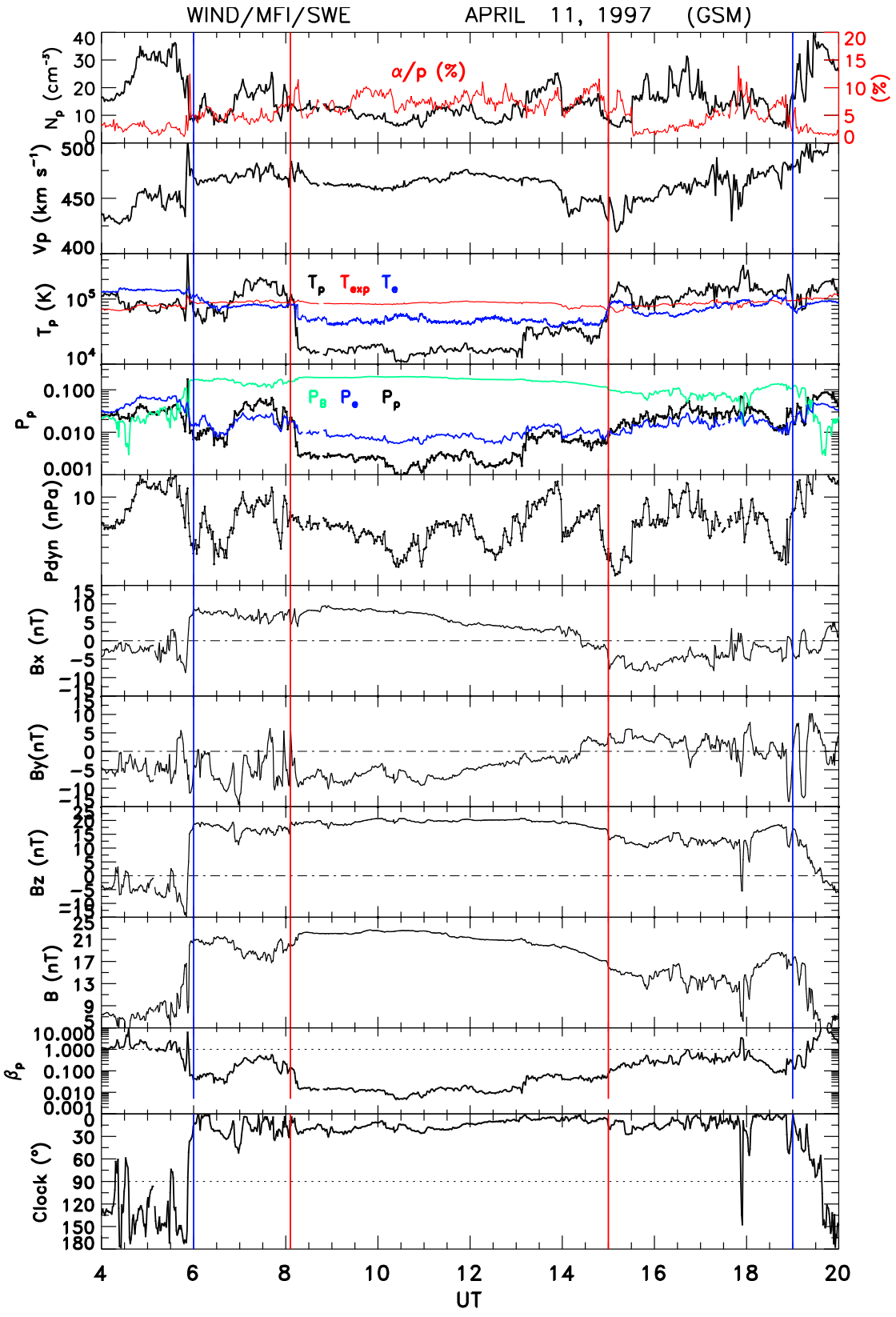

Figure 3-1: Interplanetary plasma and magnetic field data from SWE and MFI on spacecraft Wind for the interval 4−20 UT, 11 April 1997. See text for description of each panel.

3.3 Direct Evidence of Continued Reconnection: DMSP F13

We now present measurements made by the Defense Meteorological Satellite Program (DMSP) F13 satellite to study the convection in the northern polar cap region. The F13 satellite followed a sun-synchronous, approximately dusk-dawn orbit at low altitudes. Figures 3-2−3-4 show plots of data acquired by three sensors on the F13 satellite. Figure 3-2 shows a pass which occurred about three hours before the MP *in situ* data which we present below were acquired (11:15−11:42 UT); the measurements in Figure 3-3 are during the event (14:38−15:05 UT); and those in Figure 3-4 are two hours later (16:19−16:46 UT) on 11 April 1997.

The panels show, from top to bottom, the ion (dotted) and electron differential number fluxes (cm^{-2} s^{-1} sr^{-1}), the average energy of the ions (dotted) and electrons (eV), color-coded electron and ion spectrograms in the 30 eV to 30 keV energy range, and the horizontal (cross−track, in black) and vertical (in green) ion flow speeds (ms^{-1}).

When F13 passed the northern hemisphere and reached the very high latitude polar cap at 14:51 UT (Figure 3-3), we note that the cross-track component showed a clear sunward flow which reached up to 1 km/s. At lower latitudes the flow was antisunward. Similarly, a very clear sunward flow of approximately 2 km/s was seen in Figure 3-2 when F13 approached $\sim 82^0$ MLAT at 11:28 UT, and a sunward flow, greater than 1 km/s was seen in Figure 3-4 when F13 approached $\sim 86^0$ MLAT at 16:32 UT. These flow patterns are all cases of reverse convection [*Maezawa*, 1976; *Crooker*, 1992]. This ionospheric signature of reconnection poleward of the cusp persisted throughout the whole interval of northward IMF. During its observation of the reconnection layer between 14:30−15:00 UT, Polar was seeing a reconnection process which had been ongoing for hours.

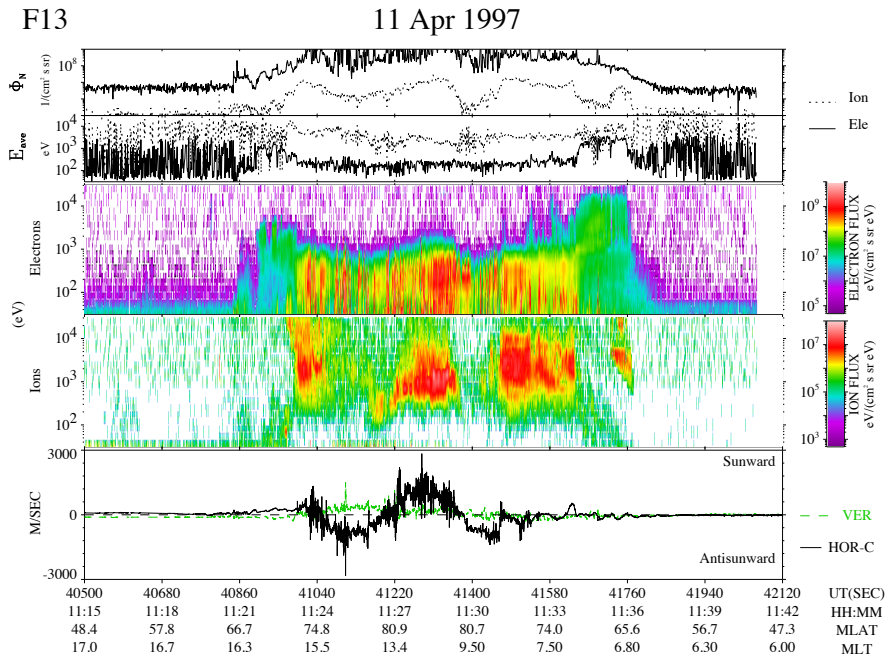

Figure 3-2: DMSP F13 precipitation and ion drift for the time interval 11:15−11:42 UT (three hours before the event) on an approximately dusk-dawn orbit. From top to bottom the ion (dotted) and electron number differential fluxes (cm^{-2} s^{-1} sr^{-1}), the average energy of the ions (dotted) and electrons (eV), color-coded electron and ion spectra in the 30 eV to 30 keV energy range, and the horizontal (cross-track, in black) and vertical (in green) ion flow speeds (ms^{-1}).

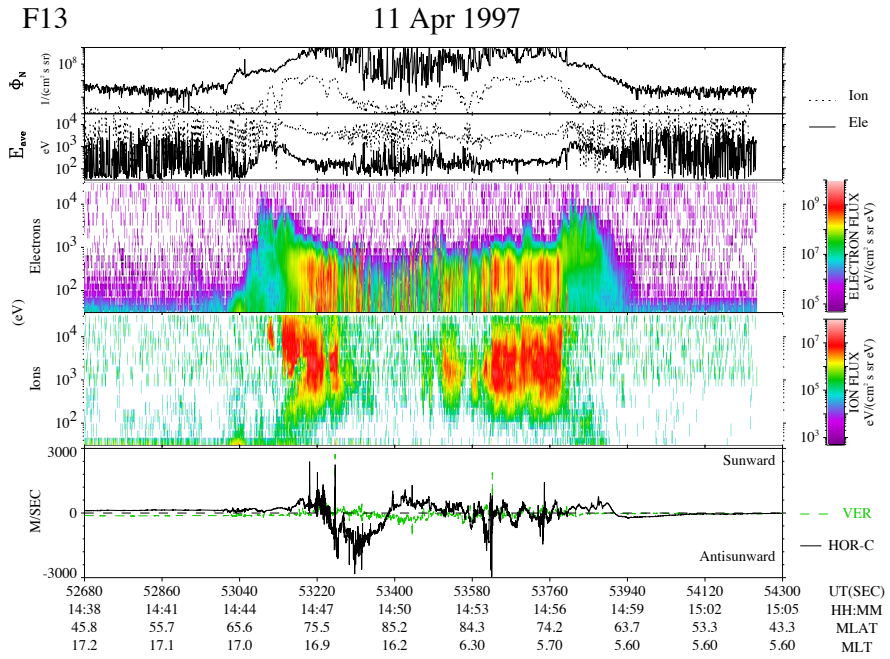

Figure 3-3: DMSP F13 precipitation and ion drift for the time interval 14:38−15:05 UT (during the event). Panels same as Figure 3-2.

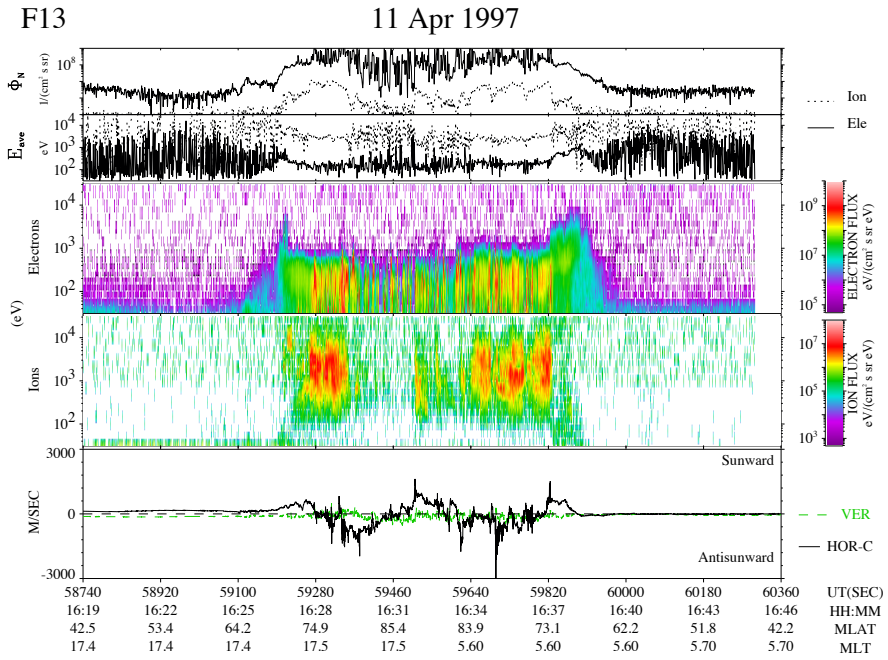

Figure 3-4: DMSP F13 precipitation and ion drift for the time interval 16:19−16:46 UT (two hours after the event). Panels same as Figure 3-2.

From panels 3 in Figure 3-2−3-4 we note that in the polar cap the electron precipitation was sporadically very intense. It rose to very high energies up to 1 keV, and was also inhomogeneous. Note also the presence of energetic ion bursts at 14:52 UT. This type of precipitation is often referred to as a "polar shower" [*Shinohara and Kokubun*, 1996]. It is very different from the homogeneous electron precipitation arising from dayside reconnection at low latitudes and called the "polar rain" [*Fairfield and Scudder*, 1985], which is typically devoid of ion precipitation.

3.4 In Situ Observations: Polar

3.4.1 Overview of Multiple Crossings

At 14:00 UT Polar was located at (3.12, 1.58, 7.61) R_E (GSM). During the time when *in situ* MP observations were obtained, Polar was at 79.8^0 MLAT at 14:30 UT, and had reached 81.1^0 MLAT by 15:00 UT. The MLT range was 17-18 hours, i.e., Polar was at duskside high latitudes at the poleward side of the northern cusp.

We used data from the Magnetic Field Experiment (MFE) [*Russell et al.,* 1995], proton and electron data from the HYDRA instrument [*Scudder et al.,* 1995], and the densities derived from the spacecraft potential [*Harvey et al.,* 1995]. Figure 3-5 gives an overview of observations Polar made in the interval 14:30−15:00 UT. The panels show, from top to bottom, the electron density from the spacecraft potential (6 s resolution), proton temperature (13.8 s resolution), the components of the velocity vector (13.8 s resolution), the total bulk speed, the components of the magnetic field (13.8 s resolution) in GSM coordinates, and total field strength.

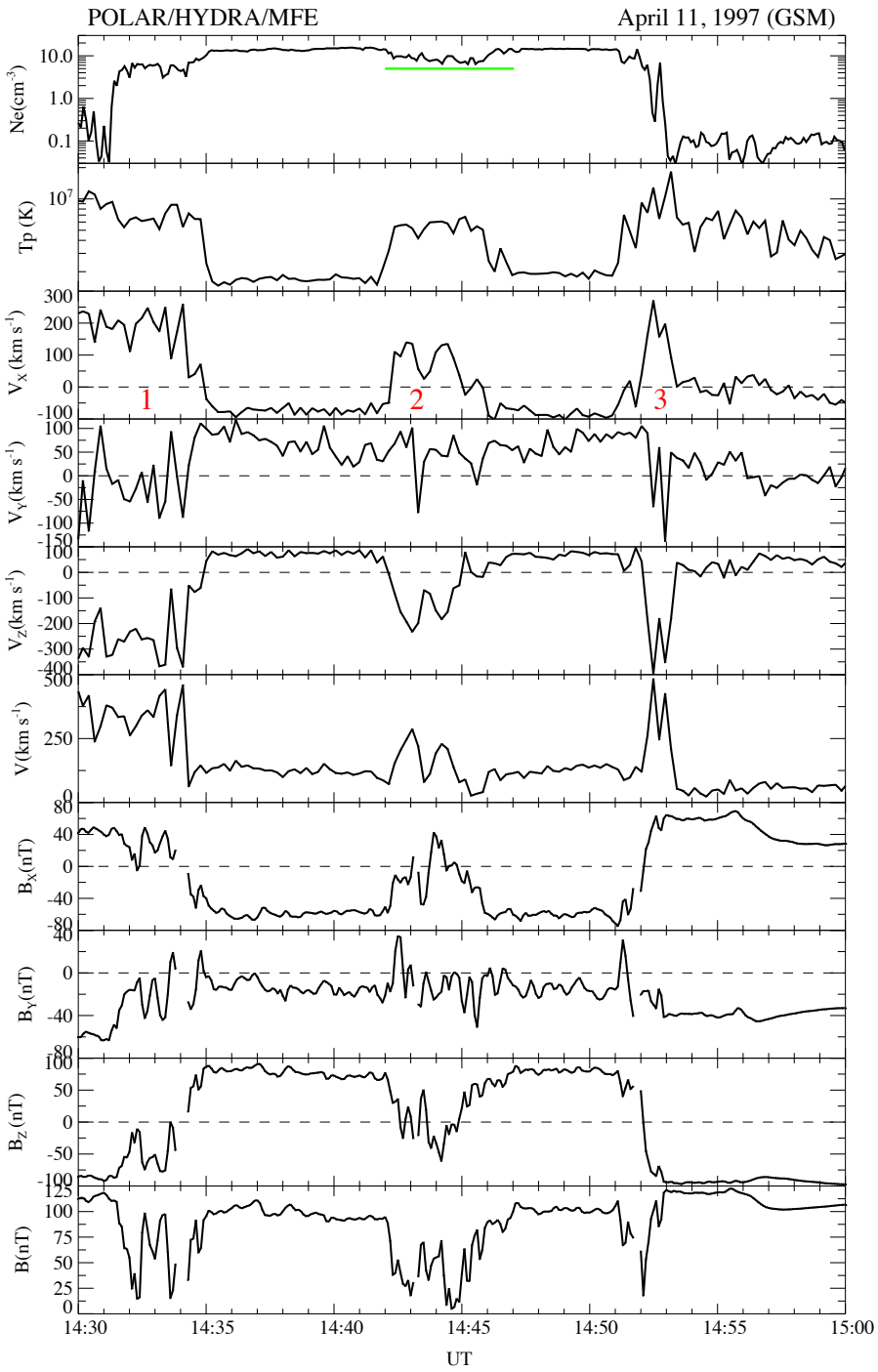

Figure 3-5: Plasma and magnetic field data from the HYDRA and MFE instruments, and density from spacecraft potential, on Polar for the period 14:30−15:00 UT. From top to bottom the panels show the electron density, proton temperature, GSM components of bulk speed, total bulk speed, GSM components of magnetic field and total field strength. Reconnection jets are indicated by the red labels 1-3 while the partial crossings are shown by the horizontal green bars.

The plot shows that Polar made two complete MP crossings: an outbound crossing from 14:30−14:36 UT, and an inbound crossing from 14:52−14:55 UT. During the outbound crossing, the spacecraft started in a regime on the poleward edge of the cusp characterized by $B_x > 0$, $B_z < 0$ with low density and high temperature and went to a dense and cold regime where $B_x < 0$, $B_z > 0$. These regimes correspond to the MSP and MSH, respectively. During the inbound crossing at ∼14:52 UT, Polar moved from a regime with $B_x < 0$, $B_z > 0$ (MSH) to a regime with $B_x > 0$, $B_z < 0$ (MSP). After the inbound crossing, observations of reconnection signatures stopped. Subsequently, no further reconnection signatures were seen and the spacecraft stayed in the MSP. As noted before, the convection delay time was estimated to be ∼53 min. We noticed a sharp dynamic pressure drop at 14:00 UT at Wind (Figure 3-1, panel 5). This would then arrive at Polar's location at roughly 14:53 UT, which coincides closely with the time of the inbound crossing noted here. This is in very good agreement with Polar's exit from the MP environment. Note the magnetic field rise coincident with the density minimum at ∼14:31 UT on the outbound pass. This feature was also seen on the inbound pass. The main focus of this work is to examine this inbound crossing in detail.

In between the two complete crossings, Polar evidently made several partial entries from the MSH to the MP boundary layer, i.e., not entering to the MSP proper, during the interval 14:42−14:48 UT (green bar). This is suggested by the density dips (not as low as the MSP) as well as fluctuations in the magnetic field, including strong field depressions. Note that the temperature increased during these partial crossings but did not reach MSP values. Note also the two-humped total velocity profile (panel 6) and total magnetic field profile (panel 10), suggesting that the spacecraft had crossed into the reconnection jet from the MSH side but had not progressed as far as the MSP proper. Accordingly, for most of the interval in Figure 3-5, the spacecraft was in the MSH with its high density of ∼14 cm^{-3}.

The Alfvén Mach number when Polar observed the MSH flow was 0.2−0.3 (not shown), i.e., the MSH flow was sub-Alfvénic. After ∼14:54 UT the spacecraft was in the MSP, as demonstrated by the plasma density of ∼0.1 cm^{-3}, the magnetic field orientation, and the low velocity.

During the intervals 14:30−14:35 UT, 14:42−14:46 UT and 14:52−14:54 UT, Polar observed accelerated sunward and southward flows ($V_x > 0$, $V_z < 0$) that reached up to ∼500 km/s and are marked by the red labels, 1−3. These are the reconnection jets. The strong sunward flows are preceded by weaker anti-sunward flows in the MSH, (for example 14:47−14:50 UT) with $V_x < 0$, $V_z > 0$ of roughly equal strength (∼100 km/s). They are in the direction of the MSH flow. If they were counter streaming flows due to reconnection they would be stronger; they are too weak to be jet reversals. We therefore interpret these flow data as Polar traversing the reconnection layer earthward of the X−line.

We now advance plausible evidence of entries into the IDR during these crossings. Lets start with the adibatic expansion parameter δ_i introduced in Chapter 1. Figure 3-6 shows in GSM coordinates the components of the convection electric field $-\mathbf{V_p} \times \mathbf{B}$ in black and the spin averaged, measured electric field in red. Underneath each component panel is plotted the difference between the two. The last panel then shows the δ_i parameter. It reaches and even exceeds values of $\gtrsim$1 at the crossings. Thus at these times the IDR is crossed. Everywhere else in the interval δ_i is small and we can reasonably assume the ions are magnetized.

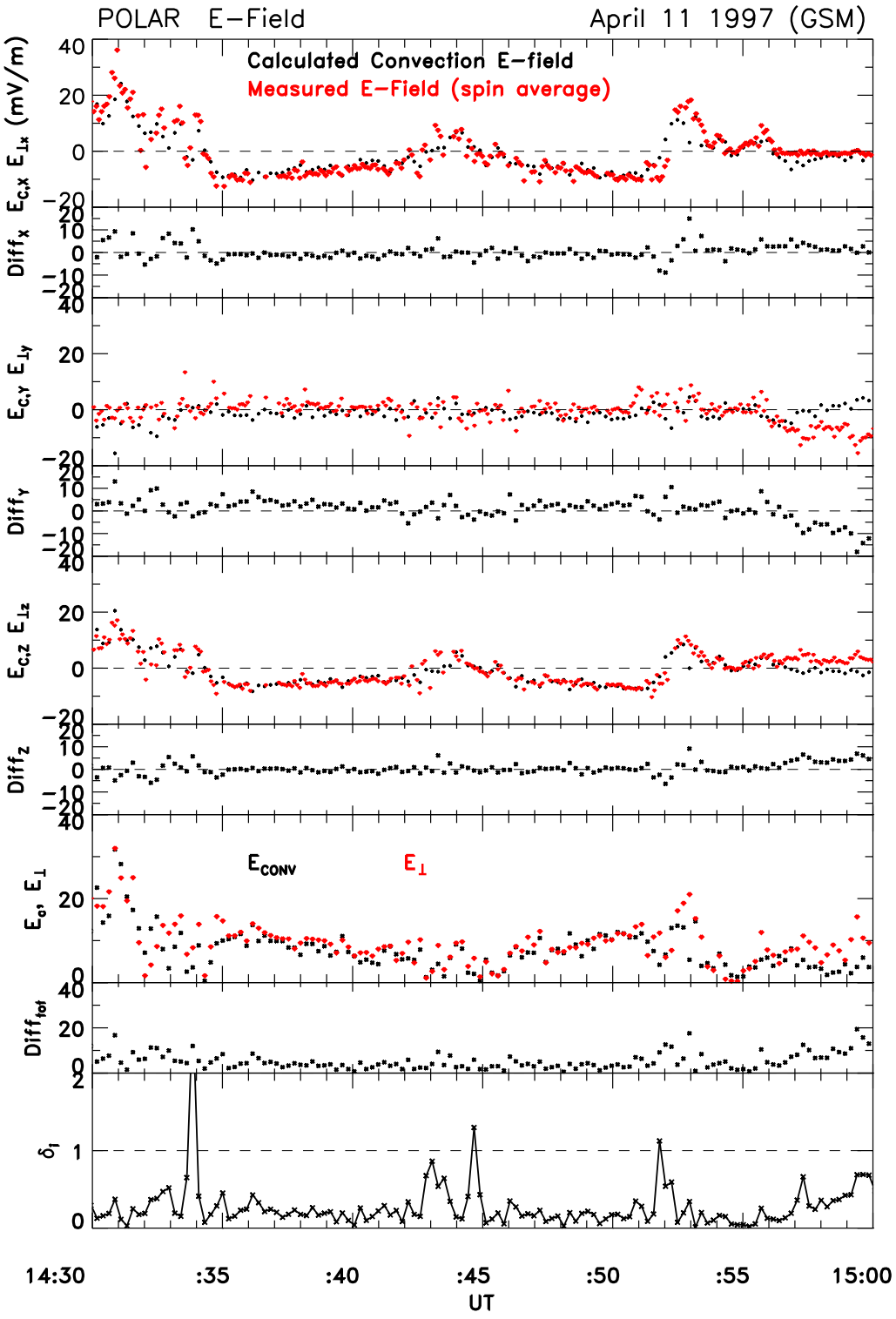

Figure 3-6: The components of the convection electric field $-\mathbf{V_i} \times \mathbf{B}$ in black and the spin averaged, measured electric field in red (GSM) for the period 14:30−15:00 UT. Underneath each component panel is plotted the difference between the two. The last panel shows the δ_i parameter.

In Figure 3-7, we draw a cartoon to qualitatively visualize Polar's orbit relative to the reconnection layer. The MSH and MSP regimes are labeled in red. The MSH field lines are shown in purple while the MSP field lines are in black. The trajectory during the time interval 14:30−15:00 UT is marked by green arrows, starting at the label S and ending at the label E. The thick blue arrows show the reconnection jets. The trajectory relative to the reconnection layer was determined by the density, magnetic field orientation and bulk velocity. The figure contains further information which will be described later.

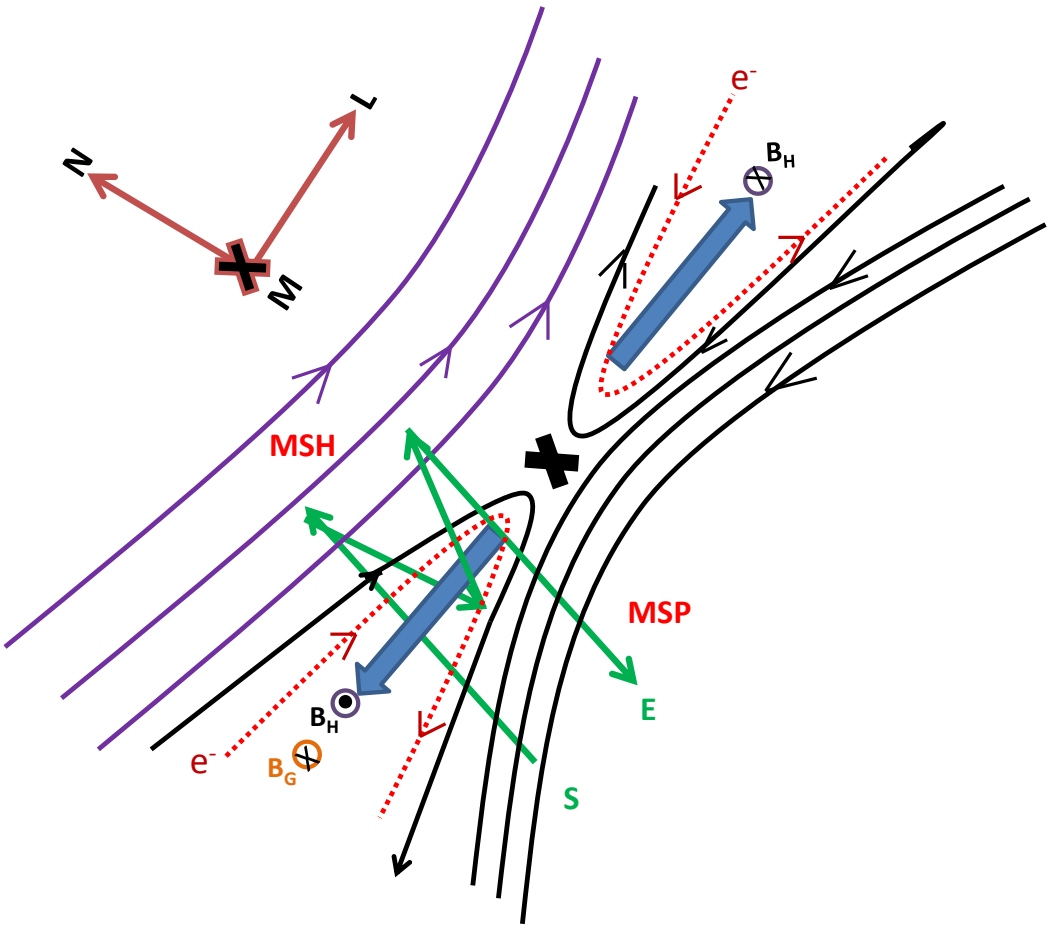

Figure 3-7: Cartoon interpreting the trajectory of Polar making several entries to the reconnection layer on one side of the X−line. The start and end of the trajectory during the time interval 14:30−15:00 UT are marked by S and E, respectively.The MSH and MSP are labeled in red. The MSH field lines are in purple and the MSP field lines are in black. The thick blue arrow shows the reconnection jets. The electron flow is shown by the dotted red line.

3.4.2 An Event with Extreme Density Asymmetry

Our focus is now on the complete inbound crossing. We present Polar observations for the four-min interval 14:50:30−14:54:30 UT. We use high resolution data from MFE (∼8 Hz) and Electric Field Investigation (EFI) [*Harvey et al.,* 1995] (∼41 Hz) instruments. We obtained the MP normal **N** by forming a cross product between the ambient MSH and MSP fields, taking averages over 14:50:00−14:50:30 UT for the former and 14:53:45−14:54:15 UT for the latter as described in Chapter 2. We obtained **N**= (0.840, -0.021, 0.541), i.e., **N** points mainly sunward and northward, **L**= (-0.541, 0.013, 0.841), i.e., mainly northward and anti-sunward, and **M**= (-0.025, -0.999, 0) i.e., pointing westward.

The EFI instrument measures three components of the electric field through three sensors arranged orthogonal to each other; two sensors on the spin plane and the one on the spin axis. The on-axis booms are closer to the spacecraft and thus are more sensitive to the spacecraft potential and the plasma environment around the spacecraft. To get rid of an offset, we discarded the on-axis measurements and obtained the third component using an assumption: we reconstructed the third component by assuming that there are no field-aligned potential drops, i.e., the parallel electric field is zero, $\mathbf{E} \cdot \mathbf{B} = 0$, which is a valid assumption for the time scales considered; the same way the third component was calculated for measurements from the Cluster EFW instrument. However, the results from this assumption become less trustworthy when the magnetic field is too weak [see *Eastwood et al.,* 2007].

Figure 3-8 shows the Polar observations from 14:50:30−14:54:30 UT. From top to bottom, the panels show the electron density on a log scale, electron density on a linear scale, the LMN components of the magnetic field, the total magnetic field strength, ion outflow bulk velocity in the L-direction V_{iL}, the LMN components of the electric field and the total electric field. The red traces in panels 8-10 represent the components of the convection

electric field.

The ambient MSH and MSP are labeled in red. We took the averages of the ambient density in the MSH from 14:50:00−14:50:30 UT, and in the MSP, from 14:53:45−14:54:15 UT and obtained a ratio of $N_{MSH}/N_{MSP} \approx 140$. This is thus a case of a very pronounced density asymmetry. By contrast, the ambient magnetic field strength ratio is $B_{MSH}/B_{MSP} = 0.85$ and there is a magnetic shear of 155^0 between the MSP and MSH fields.

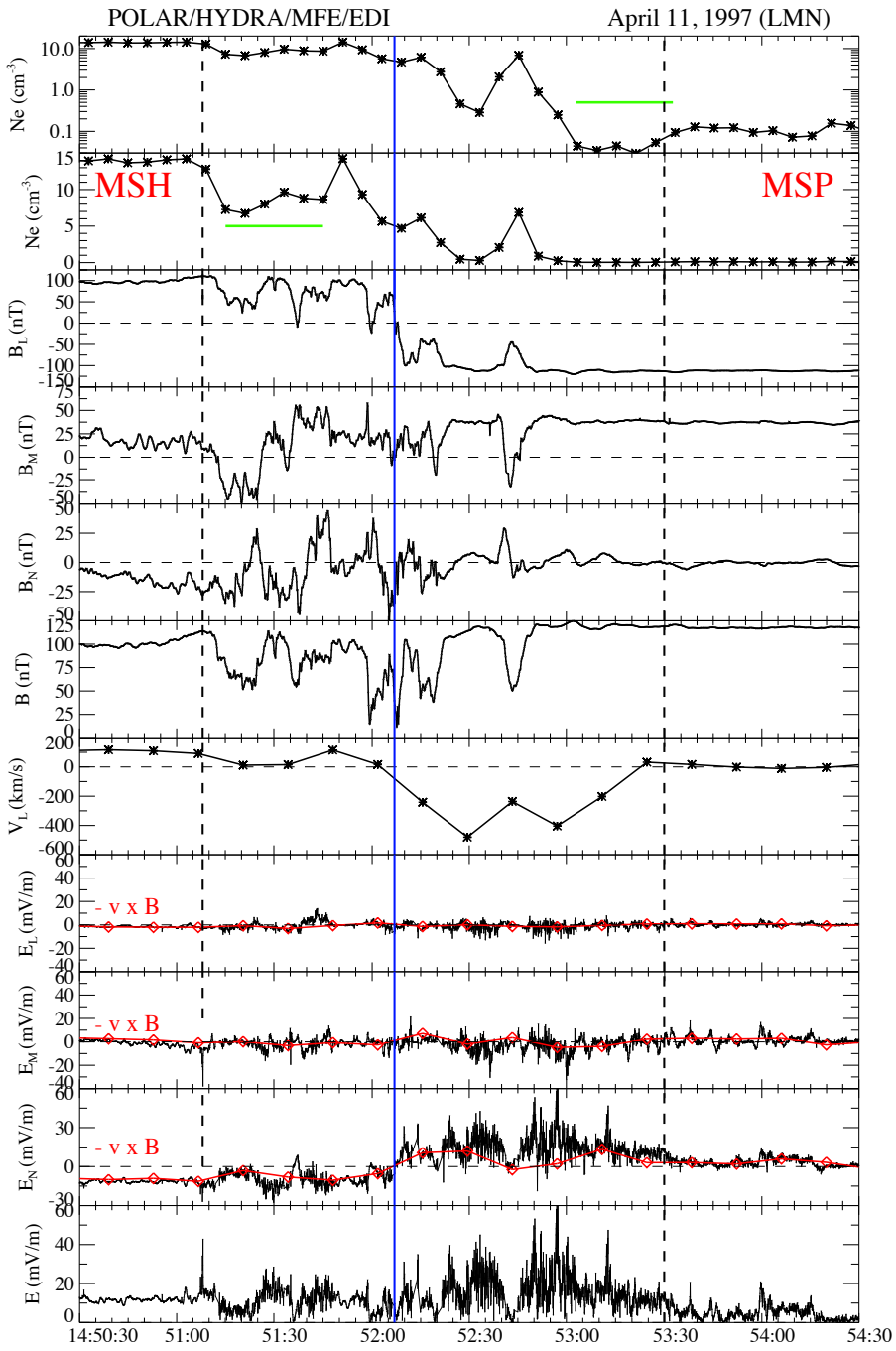

Figure 3-8: Plasma, electric field and magnetic field data from HYDRA, EFI, and MFE instruments on Polar for the period 14:50:30−14:54:30 UT. From top to bottom panels show electron density in log scale, electron density in linear scale (derived from the spacecraft potential), LMN components of magnetic field, total magnetic field, V_L, LMN components of electric field and total electric field. The black dotted vertical lines indicate the separatrices while the blue vertical line marks the complete inbound crossing. The density dip regions at the SR on the MSH and the MSP side of the MP marked by the green horizontal bars.

The first and third vertical guidelines bracket the region where the reconnection signatures are seen. The blue guide line at 14:52:07 UT marks the definitive CS crossing where B_L reverses polarity. This reversal took 4 s. In the interval shown, the spacecraft started at the high density MSH (average $\sim$14 cm^{-3}), encountered a density dip region at 14:51:15−14:51:45 UT (first green bar, panel 2), a strong negative gradient and another density dip region at 14:53:03−14:53:33 UT (second green bar, panel 1) before it recovered to the low density MSP value (average $\sim$0.1 cm^{-3}). The two density dips help define the two separatrices. This identification is further confirmed by the fact that the vertical guidelines form boundaries between quiet and turbulent electric fields [*Mozer et al.*, 2002; *Andrè et al.,* 2004; *Khotyaintsev et al.,* 2006]. Note that the declining density profile occurred after the B_L polarity reversal (blue vertical line) without any overlap, as did also the flow jet. Importantly, this decreasing density profile was interrupted for 30 s from 14:52:30−14:53:00 UT by a clear field and flow feature that we discuss further below.

There are apparent temporal variations, in particular, on the MSH side of the CS. For example, B_L made two brief excursions to negative values at 14:51:37 UT and 14:52:00 UT before the definitive B_L polarity change. Note that $|\mathbf{E}| = 0$ at these times. Recall also that the solar wind dynamic pressure was variable. It is likely that Polar was observing temporal fluctuations produced in the interplanetary medium.

The figure furnishes compelling observational evidence of a huge contrast between the MSH side and the MSP side of the CS. Soon after the spacecraft crossed over to the MSP side of the CS, a sunward and southward-pointing ion jet that reached up to 500 km/s was seen. This occurred at the sharp density gradient on the MSP side (panel 1) of the CS.

In the electric field data (panels 8−11) the two black vertical dotted lines delimit the region of strong electric field activity, as noted. We identified these as the separatrices. All components of the electric field fluctuations were clearly larger on the MSP side of the CS

than on the MSH side. The electric field strength reached values of 60 mV/m. Most of the activity was in the normal component of the electric field, E_N. The E_N component has a clear polarity change from smaller (negative) to larger (positive) where we identified the CS crossing (blue vertical line), i.e., E_N is pointing towards the CS on both sides. These are the Hall electric fields. The largest fluctuations occurred when the spacecraft traversed the jet, where E_N peaked at 60 mV/m during the strong density gradient. Note that E_L was the least perturbed component and was essentially 0 throughout the interval.

There was an isolated peak in electric field activity associated with the start of the density dip region on the MSH side, where E_N reached up to 30 mV/m in the negative direction. On the MSP side, in middle of the extended density dip region, there was an isolated peak with positive E_N reaching 45 mV/m.

The out-of-plane B_M is mainly positive on both sides of the CS but fluctuated more on the MSH side. In the density dip region on the MSH side of the MP (first green bar), there was an excursion of B_M to large negative values, lasting for ∼13 s. This is coincident with the total magnetic field depression and $|\mathbf{E}| \approx 0$.

A pronounced feature of the data was observed during the negative density gradient from 14:52:38−14:52:52 UT. Here the flow was attenuated to ∼200 km/s (in the spacecraft frame) and the density rose to 7 cm^{-3}. Interestingly, the magnetic field executed clear deflections with a bipolar signature in B_N whose peak-to-peak amplitude was 25 nT. Simultaneously there were unipolar deflections in B_L and B_M. In addition, the electric field has a clear depression, essentially vanishing at the center of the interval. We return to this feature in the discussion section.

3.5 Effect of the Guide Field

Figure 3-9 shows measurements made by the HYDRA instrument [*Scudder et al.*, 1995]. From top to bottom the figure shows a spectrogram of the differential energy fluxes (as a function of time with the energy color-coded) for electrons and ions, the electron skew and the electron anisotropy for the period 14:00−15:00 UT. The data have been corrected for spacecraft potential effects. The electron skew and anisotropy are moments of the distribution functions defined as $\frac{\mathbf{J}_{||}}{\mathbf{J}_{-||}}$ and $\frac{\mathbf{J}_{||}+\mathbf{J}_{-||}}{\mathbf{2J}_{\perp}}$ respectively, where $\mathbf{J}_{||}$ is the current density aligned with the field, $\mathbf{J}_{-||}$ is the current density opposite to the field, and $\mathbf{J}_{\perp}$ is the current density perpendicular to the field. Accordingly, the electron skew indicates whether the particles moving parallel to the field are aligned or opposed to it. The anisotropy indicates whether the electrons are moving mostly perpendicular or parallel to magnetic field. We notice very detailed ongoing electron dynamics at the same time as the crossings.

The outbound crossing at 14:30−14:36 UT, the shorter inbound crossing 14:52−14:55 UT and the partial crossings 14:42−14:48 UT are clearly observed in the electron and ion spectra as enhancements in the intensity of higher energy particles (above ∼200 eV for electrons, above 4×10^3 eV for ions).

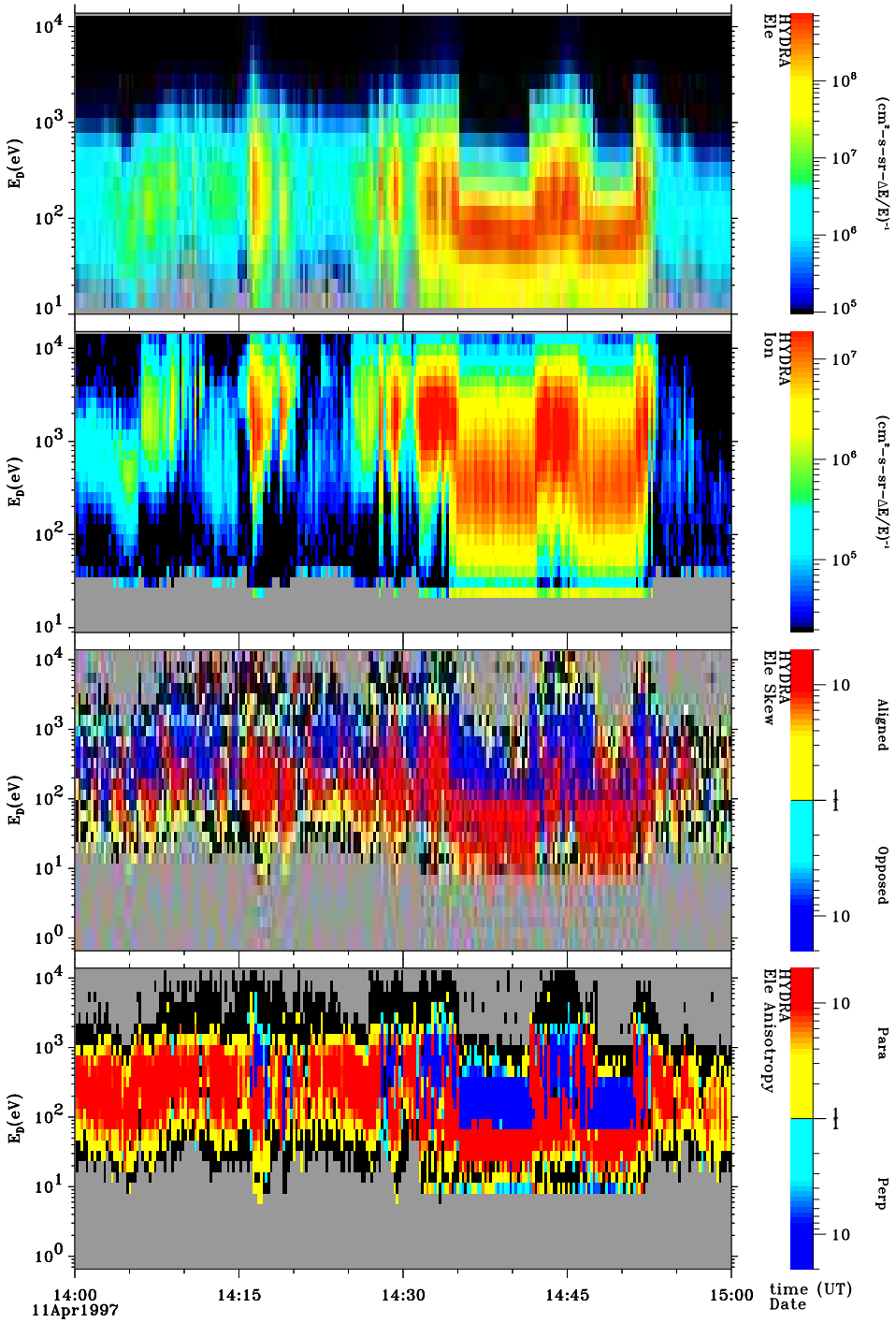

Figure 3-9: Differential energy fluxes (as a function of time and energy) for electrons and ions, electron skew (indicates whether particles are aligned or opposed to the magnetic field), anisotropy (indicates whether particles are perpendicular or parallel to the magnetic field), from the HYDRA instrument for the period of 14:00−15:00 UT.

The skew at the MSH separatrix at 14:51:10 UT of high energy electrons (100 eV−1 keV) is blue and at lower energy red (< 100 eV) while the anisotropy is red. This indicates that the high energy electrons are flowing opposed and parallel to the field while the low energy electrons are flowing aligned and parallel to the field and towards the X−line. The skew at the MSP separatrix at 14:53:30 UT of the high energy electrons (> 1 keV) is red and the low energy electrons (< 100 eV) are yellow while the anisotropy is red, i.e., the electrons are flowing aligned and parallel to the magnetic field and away from the X−line. The flow of the electrons are shown by red traces in Figure 3-7. On the side of the X−line where Polar is crossing, this electron flow creates the out-of-plane Hall magnetic field B_H which points in the negative M- direction (The electron flow shown by the red traces on the tailward side of the X−line are drawn from expectations of bipolar Hall fields and not from observations.)

Taking the average of the ambient fields of the MSH and MSP in the out-of-plane M-direction, we have an average guide field of ∼30 nT (see panel 4, 3-8), which is ∼ 25% of the total field. We recall that Polar's position is on the sunward side of the X−line (Figure 3-7). The guide field, B_G, points opposite to the Hall magnetic field, B_H.

The measured B_M is the sum of the two, $B_M = B_G + B_H$. Figure 3-8 showed that the measured B_M is unipolar and mostly positive on both sides of the CS. The guide field B_G acts to weaken the Hall field, making the out-of-plane B_M change sign at one point. This is clear evidence that the guide field has distorted the expected Hall magnetic field structure. Also note that near the MSH separatix, there is an interval where B_M has opposite polarity (negative) and exceeds the guide field B_G.

3.6 Summary and Discussion

3.6.1 Summary

In this paper we have presented Polar observations of processes at a high latitude magnetic reconnection site on the poleward edge of the cusp, on 11 April 1997. We have provided interplanetary observations through the Wind spacecraft, which was at an ideal location to monitor the solar wind. We have an exceptional case of a strong IMF pointing strongly northward for 13 hours. Through DMSP data we also provided direct evidence of continued reconnection through ionospheric flows at high latitudes. The spacecraft recorded continuous reverse convection in the northern polar cap for 12 hours during the time period when Wind observed strong northward IMF ($B_Z \approx$20 nT).

Through an overview of the ion and magnetic field behavior we showed that Polar made several encounters with the reconnection layer. It made two complete MP crossings; one outbound and one inbound, and encountered sunward/southward flowing jets. Since the anti-sunward flows were too weak to be a jet reversals, i.e., their speeds were not higher than the MSH flow, we concluded that Polar traversed the reconnection layer earthward of the X−line.

We then focused on the last, inbound crossing. This was an event with a density asymmetry of over two orders of magnitude $N_{MSH}/N_{MSP} \approx 140$. To the best of our knowledge, an event with such a high density asymmetry has not been analyzed before either in observations or in simulations.

We also analyzed the electron behavior during our interval of interest through the differential energy fluxes, electron skew and anisotropy obtained from HYDRA. We provided evidence of low-energy electrons moving from the MSH separatrix to the MSP separatrix. The associated current densities are the source of the Hall magnetic field structure, which pointed opposite to the guide field.

There was a clear contrast in fields and particle behavior before and after the B_L reversal. Most activity was located between the CS and the MSP separatrix: (i) very strong electric fields (up to 60 mV/m), (ii) the sunward flow was located on the MSP side, (iii) the electric field component (E_N) had larger values, and (iv) E_N had a clear bipolar structure, changing sign at the B_L reversal.

We also found two density dip regions at the start and the end of the reconnection layer encounter, one on the MSH separatrix and one on the MSP separatrix. At these density depressions we noted isolated peaks in E_N pointing towards the CS. The two density dips bracketed the interval where there were electric field fluctuations. They thus served as good indicators of the separatrices.

During this crossing, a strong V_y component is seen (Figure 3-5, panel 4). We therefore examined how much of the E_N component may be due to the convective electric field by plotting $-\mathbf{V_p} \times \mathbf{B}$ in Figure 3-8 in LMN coordinates (red traces). We overlaid this result on the measured electric field to compare the two. The values of the N component of the $-\mathbf{V_p} \times \mathbf{B}$ are a small fraction of the high values of the electric fields seen, especially on the MSP side. Further, it does not reproduce the localized peaks in E_N seen at the density depletions. From this we believe that most of the electric field is Hall-related and not due to the convective electric field.

We advanced a plausibility argument that Polar crossed the IDR because the magnetization condition, $\delta_i \approx 0$, is not satisfied. Other considerations are consistent with this conclusion. Firstly, according to *Eastwood et al.*, [2010], "one of the most significant signatures [of the IDR] is in fact the total DC electric field (which is in large part dominated by the Hall electric field), which can attain peak values of several tens of millivolts per meter". Such strong fields were observed by Polar. Secondly, there was evidence of Hall electric fields pointing towards the CS. This direction is consistent with expectations for

the IDR [e.g., *Tanaka et. al.*, 2008]. Finally, despite having data from a single spacecraft crossing on one side of the X−line, a qualitative argument that the spacecraft is not too far from the X−line is based on the flow speed. The observed flows are sub-alfvénic. Using the equation for outflow speed derived by *Cassak and Shay* [2007] (their equation 14), for symmetric magnetic fields and asymmetric densities, the maximum ion flow in our event was 500 km/s or 0.58 V_{Alfven}. Nevertheless, we point out that these are in the nature of plausibility arguments. This is because there is no absolute criterion for identifying the IDR.

3.6.2 Structure of the Ion Diffusion Region

We now discuss how the structure of the IDR depends on the size of the density asymmetry.

(i) *Mozer et al.* [2008a], examined the effect that a density asymmetry has on the Hall fields. The authors gave quantitative theoretical estimates of how N_{asym} affects Hall fields. Considering the generalized Ohm's law (Equation 1.1), the Hall fields were found to depend on the relative size of the ratio $\frac{B_Z}{n}$, where B_Z is the anti-parallel component of the reconnecting fields and n is the number density. The higher the value of $\frac{B_Z}{n}$, the stronger the observed Hall fields. Thus, for example, if quantity $\frac{B_Z}{n}$ is larger on the MSP side, as is normally the case in subsolar MP and lobe reconnection, the Hall electric field on the MSP side is stronger than on the MSH side. As a data example, they studied an inbound crossing of the dayside MP made by three THEMIS spacecraft. The density asymmetry between the two regions was 25; i.e., modest compared to the asymmetry reported in this paper. The guide field was 20 nT (40 % of the total magnetic field). The ratio $\frac{B_Z}{n}$ was 50 on the MSP side and only 0.4 on the MSH side. Correspondingly, the Hall electric field observed was 8 mV/m on the MSP side and was insignificant on the MSH side. The $\frac{B_Z}{n}$ ratio in our case is higher than this on both sides of the CS, and thus the Hall electric fields should be

stronger than those reported in *Mozer et al.* [2008a]. And this is indeed observed.

(ii) A very important effect of density asymmetry is its influence on the reconnection rate. Using 2D compressible MHD simulations with anomalous resistivity, *Borovsky and Hesse* [2007] found that for symmetric magnetic fields on both sides of the CS, the rate of magnetic reconnection decreases with increasing density asymmetry. They plotted the reconnection rate as a function of the density ratio, for ratios up to ∼300 (see their Figure 5). For equal densities, the normalized reconnection rate had a value of ∼0.16. For a density ratio of 10 and 100, the reconnection rate had dropped by a factor of ∼2 and ∼8, respectively. Similarly, in their 2D PIC simulations with no guide field, *Tanaka et al.* [2008] studied the reconnected magnetic flux as a function of time for cases with density ratios of 1 and 10 (see their Figure 11). For the symmetric case, the growth rate was faster and the saturation level was higher than the asymmetric case.

We now consider theoretical calculations (*Cassak and Shay* [2007]) for 4 different density ratios, spanning a wide range: (i) ratio = 1, i.e. no asymmetry (ii) ratio = 10 (iii) ratio = 30 and finally our case, i.e., (iv) ratio = 140. We use the theoretical scaling relation for the reconnection rate as derived by *Cassak and Shay*, Equation 1.5. We keep ρ_1 fixed and vary ρ_2. We take the aspect ratio $\frac{\delta}{L} = 0.1$. Applying this to the four cases, we obtain, E = 0.1, 0.03, 0.02, 0.01, i.e. E decreases with increasing density asymmetry.

(iii) In our data, we noted that the density gradient occurs after the B_L reversal. This separation has a theoretical background. A general feature of asymmetric reconnection is that the stagnation point (S−point) and the X−line are not colocated as discussed in Chapter 1, section 1.4 [*Cassak and Shay*, 2007, 2009; *Birn et al,*, 2008]. This separation is not only a property of the IDR, i.e., it can be observed even outside it (see figure 3 in Levy et al. [1964]). Indeed, in simulations of *Nakamura and Scholer* [2000], they observed this separation in the exhaust region far away from the DR.

Let us now compare our observations on this with theoretical expectations. To fix ideas, let us take a geometry of the DR similar to that of Figure 1 of *Cassak and Shay*, [2007]. We calculate the values for the relative distances of the interior structure as given by their equations (26) and (27). We obtain $\frac{\delta_{X2}}{\delta_{X1}} \sim \frac{B_2}{B_1} = 1.13$ and $\frac{\delta_{\rho 2}}{\delta_{\rho 1}} \sim \frac{\rho_2 B_1}{\rho_1 B_2} = 0.006$. Parameters δ_{X1} and δ_{X2} are the distances from the corresponding upstream edges of the DR to the X−line and, similarly, δ_{S1} and δ_{S2} are the distances from the edges to the S−point (Refer to Figure 1-6). Thus, according to these calculations, the X−line has shifted very slightly to the MSH side, and is located almost at the center of the DR. This is because the MSH and MSP have almost equal magnetic field strength. The S−point, however, is displaced to the MSP side, and by a considerable amount.

(iv) We next turn to the width of the DR. *Cassak and Shay* [2009] derived the half-thickness of the DR in their equation (17), i.e., $\delta \sim \frac{1}{2}\left(\sqrt{\frac{B_1}{B_2}} + \sqrt{\frac{B_2}{B_1}}\right) d_{out}$ where the ion inertial length $d_{out} = \left(\frac{m_p^2}{4\pi e^2 \rho_{out}}\right)^{1/2}$ and outflow mass density, $\rho_{out} \sim \frac{\rho_1 B_2 + \rho_2 B_1}{B_1 + B_2}$. We have $\rho_1 = 14.2 \times 10^6 \times m_p \ kgm^{-3}$, $B_1 = 98.5 \times 10^{-9}$ T, $\rho_2 = 0.1 \times 10^6 \times m_p \ kgm^{-3}$ and $B_2 = 111.7 \times 10^{-9}$ T. We then obtain a DR width of about 166 km. This is about 2 ion inertial lengths and $\sim$ 6 proton Larmor radii. In this context we mention that in their comparisons of THEMIS data with PIC simulations with density ratios varying from 10 to 30, with a guide field, *Mozer et al.* [2008b] found the thickness of the current sheet to be of order a few d_i.

3.6.3 Comparison with Observations and Numerical Simulations

We now compare our observations to the event reported by *Retinò et al.* [2005, 2006]. In their example of an outbound crossing of a reconnection layer poleward of the cusp under northward IMF, on the 3 December 2001. The $N_{MSH}/N_{MSP} = 10$. They ignored the small B_{asym} and considered a zero guide field (Refer to Figure 1 in *Retinò et al.*, [2006], also seen

in more detail in Figure 1 of *Tanaka et al.,* [2008]). The 3 December 2001 event was an outbound pass.

Proceeding from the MSP to the MSH side of the CS, *Retinò et al.*, [2006] subdivided the separatrix region (SR) on the MSP side of the MP into three distinct adjacent regions indicated in the paper by the yellow, magenta and blue layers. The first regime (yellow layer) was then separated into three subregions based on density, electric field and magnetic field activity and a "bulge" region. The first subregion was a sharp density cavity adjacent to the MSP separatrix that coincided exactly with the E_N peak of ∼40 mV/m. In the second subregion, the density increased gradually over the MSP level while E_N decreased. A sharp density gradient that brought the density up to MSH values and electric field fluctuations that showed strong emissions around the lower-hybrid frequency range formed the third subregion.

The next regime (magenta layer) lasting ∼14 s highlighted the main part of the tailward jet which reached a maximum speed of ∼500 km/s. The last regime (blue layer) showed the CS as a rotational discontinuity where B_L changed sign from positive to negative with non−zero B_N which lasted for 5 seconds. The CS crossing overlapped the trailing edge of the jet.

We see all these regimes in our event but not necessarily in the same order. For comparison, proceeding from the MSP side in Figure 3-8 (right to left), we first saw an extended density dip region (second green bar) lasting for 22 s, with a peak in E_N that reached 45 mV/m. While *Retinò et al.,* [2005]'s E_N peak is localized exactly at the density dip in the SR, we did not see direct correspondence due to the longer extended cavity in our event. Afterwards we saw a sharp density gradient which lasted ∼ 70 s with very high fluctuations (wavy behavior) in the electric field strength. This is much stronger wave activity than in the 3 December 2001 event.

We do not see a gradual increase in density, the region that was labeled as subregion 2 in *Retinò et al.,*'s 3 December 2001 event, but rather a sudden peak in the density gradient. This is due to the special feature that was noted in end of section 3.4.2. We noted that the entire ion reconnection jet coincides in time with this sharp density gradient. The rotational discontinuity (B_L reversal) followed. The reconnecting magnetic field B_L reversed at 14:52:07 UT, meanwhile the peak of the ion jet interval was at 14:52:15−14:52:40 UT. There was no overlap between the jet and the CS crossing. The greater bias that the data show may be attributed to the higher density ratio that our event has (140 vs. 10). If we were to color code our event as *Retinò et al.*, [2006] did, the region classified as subregion 3 (the sharp density gradient), and "bulge" region in the first regime would overlap with the second regime where the tailward jet was observed.

In our case the duration of the density gradient is ∼70 s, much longer than on the 3 December 2001 event. This may be an indication that the boundary layer is wider. This may, in turn, be due to the long duration (∼13 hours) of ongoing reconnection.

We compare the results obtained for a density asymmetry = 10 with our results. Assuming equal magnetic field strengths in the upstream regions, the ratios for the event Retinò et al. reported are $\frac{\delta_{X2}}{\delta_{X1}} \sim \frac{B_2}{B_1} = 1$ and $\frac{\delta_{\rho 2}}{\delta_{\rho 1}} \sim \frac{\rho_2 B_1}{\rho_1 B_2} = 0.1$. Thus the X−line would be exactly at the center, but the S−line would be shifted towards the MSP but not by the same amount as for the higher density asymmetry. In our example the ∼140 density asymmetry causes the S−line to be displaced 10 times more towards the MSP side that in the case of the moderate density asymmetry.

Next we compare our observations to the simulations of *Tanaka et al.,* [2008], who provided a comparison between virtual observations in 2D PIC simulation results and the Cluster MP crossing on 3 December 2001 reported by *Retinò et al.*, [2005]. The emphasis was on the density asymmetry. The key features in the observations that were used to set the

initial conditions were (1) the reconnecting magnetic fields were approximately anti-parallel and the magnitudes on both sides were the same. (2) The density profile was asymmetric, with $N_{MSH}/N_{MSP} = 10$. (3) The ion outflow in the MP results from the reconnection jet. The simulation reproduced the observed features in the 3 December 2001 event, namely, (1) the prominent density dip region detected at the SR on the MSP side of the MP, (2) the intense E_N pointing to the center of the MP at the location where the density dip is located, (3) the ion bulk outflow was biased towards the MSP side, and (4) the out-of-plane B_M had a bipolar structure.

Our results are in good agreement with these predictions in so far as they refer to the density asymmetry. We are able to see both density cavities, on the MSP as well as the MSH separatrix (see the green bars on panels 1 and 2 in Figure 3-8). The MSH separatrix was not seen in *Retino et al.,* [2005] example. The ion jet is biased strongly towards the MSP side of the CS.

We now consider the effects of the guide field. *Pritchett and Mozer* [2009] used 2D PIC simulations to examine the reconnection layer at the subsolar MP in the presence of a guide field on top of a density asymmetry. The coordinate system used in the simulations had X directed from the MSH side toward the MSP side of the current layer, Y is directed dawnward, and Z is directed northward. The density asymmetry across the current layer was 10 ($N_{MSH}/N_{MSP} = 10$) while the reversing magnetic field ratio was 3 ($B_{MSH}/B_{MSP} = 0.33$). The initial guide field was equal to the MSH B_z field, giving a magnetic shear 117^0.

The most significant effect of the guide field was to introduce a distinct north-south asymmetry about the X−line. The electron flows from the high density (MSH) to the low density (MSP) side of the CS dominated the in-plane Hall currents which, in turn, strongly enhanced the out-of-plane B_y field on one side of the X−line (northward for a dawnward directed guide field) and decreased it on the other side. On the weakened field side (in the

case considered in that paper, this is southward of the X−line), there was a weakening of the Hall out-of-plane fields, and the presence of bipolar electric field with a sharp increase at the separatrix (see their Figure 5). On the enhanced magnetic field side (the northward side of the X−line) there was a bipolar pair of electric fields and an electron velocity shear flow layer, structures not present on the other side (the southern side of the X−line). For comparison to our event in this chapter, April 11, 1997, we are interested in the weakened side of the X−line.

Referring to our event, as expected in asymmetric reconnection, as B_L changes sign, the out-of-plane magnetic field, B_M, is mostly positive on both sides of the crossing indicating a unipolar structure, apart from one excursion to negative values. This is consistent with the trajectory of Polar traversing one side of the X−line. We do not see any pronounced differences in strengths when comparing the magnetic field B_M on either side of the CS. In addition, as argued above, the guide field pointed opposite to the Hall magnetic field which weakened the out-of-plane B_M component. This is exactly what was seen in the simulations.

Interestingly, at the MSH SR (first green bar in Figure 3-8) of the event we report, B_M was $\sim$ 50 nT in the negative direction and lasted for $\sim$13 s. This was coincident with the total magnetic field depression and electric field going towards 0. A similar B_M reversal is also reproduced in the simulations. As *Pritchett and Mozer* [2009] state, "the B_y magnitude is substantially reduced, and the field even changes sign in a small region inside the MSH separatrix".

The simulations predict that the electric field should be dominated by the strong MSH-directed normal component, E_N. The other components should be much weaker, as we also observe. In our case, the electric field reaches up to 60 mV/m on the MSP side and isolated peaks at the MSH and MSP separatrices with values of 30 mV/m and 45 mV/m

respectively.

As noted at the end of section 3.4.2, we noticed an unusual feature in the exhaust region which occurred during the negative density gradient. i.e., when the spacecraft was traversing to the MSP side. Here the flow was attenuated and the density increased. The magnetic field had a clear bipolar signature in B_N with peak-to-peak amplitude $\sim$ 25 nT and simultaneous deflections in B_L and B_M which lasted for 40 s. The magnetic component signature and its duration are similar to that of an FTE [*Russell and Elphic*, 1978] and bear resemblance to the propagating bulge in the exhaust region that *Retinò et al.,* [2006] named a micro-FTE. The amplitude of this micro-FTE in the event on 3 December 2001 was $\sim$40 nT and lasted for 5 s. However, in our case other features argue against this being a micro-FTE. The electric field oscillations weakened considerably and vanished at the center of the interval. Simultaneously, the total magnetic field decreased to 50 nT. The field depression was not typical of FTEs. So we think that this feature is likely to be a magnetic island in the exhaust region. It might have been produced by the process of magnetic reconnection (see *Eastwood et al.*, [2007]).

One might ask whether Polar crossed not only the IDR but also the much smaller electron diffusion region (EDR). A way of finding out is to calculate the electron thermal Mach number, $M_{e,\perp} = \frac{|\mathbf{u}_e|}{\langle w_{e,\perp} \rangle}$, where $\mathbf{u}_e$ is the electron bulk velocity and $\langle w_{e,\perp} \rangle$ is the electron thermal speed derived from the perpendicular temperature. In the EDR this quantity exceeds unity [*Scudder et al.*, 2012]. Consulting electron data (not shown) for the interval from one separatrix to the other, we find that the maximum $M_{e,\perp} \approx 0.17$. It thus appears that Polar did not cross the EDR.

In summary, we have presented a case of reconnection at the poleward edge of the cusp hallmarked by a large density asymmetry and a guide field. Comparing with relevant simulations we found good agreement. There were, however, some discrepancies. In our view,

it would be worthwhile to conduct numerical simulations with a higher density asymmetry than usually done. From an observational point of view, it would be nice to examine data from crossings on both sides of the X−line under the same external conditions to permit observational comparisons. The Magentospheric Multi-scale mission (MMS) will be able to achieve these goals.

Chapter 4

Effect of a guide field at high-latitudes poleward of the cusp

4.1 Introduction

In this chapter we study the effect of a guide field on the Hall field structure of the IDR. Ideally, to isolate effects of a guide field we would require an event with negligible density asymmetry. As discussed in Chapter 2, unlike simulations, it becomes challenging to find an event when only one boundary condition is different from the symmetric case to isolate the effect of that boundary condition on the structure of the IDR. Here, we picked events with low values of N_{asym} and high guide fields from our table 2.5 in Chapter 2 and compare these events to predictions of asymmetric simulations with a guide field.

When considering the effect of the guide field on the Hall magnetic and electric field structure of the DR, as discussed in previous chapters, the presence of a density asymmetry changes the out-of-plane quadrupolar Hall field configuration to a bipolar configuration as seen when a spacecraft crosses from one side of the X-line to the other. One key effect that is brought about by the guide field on top of the bipolar feature, is a 'North-South' asymmetry

in the out-of-plane Hall field, B_Y component. In events poleward of the northern/southern cusp, this will become an asymmetry between the sunward side and tailward side of the X-line giving a 'sunward-tailward' asymmetry. We shall focus on this feature in our study. Other major effects caused by the guide field is the motion of the X-line due to the electron diamagnetic drift [*Swisdak et al.*, 2003; *Pritchett*, 2008] and the changes in reconnection rate.

The layout of this chapter is as follows. Section 4.2 gives a summary of the key findings of *Pritchett and Mozer*, [2009] 2D PIC simulation study with emphasis on the Hall magnetic and electric field features in the presence of an uniform guide field. In Section 4.3, we present two events with similar and moderate guide fields (26% of the reconnecting $B_{L,MSH}$) with clear jet reversals. Events with jet reversals allow us to compare *both sides*, the sunward and tailward side of the X-line, to showcase the effect of the guide field on the Hall field structure. The density asymmetries differed in the two case studies. This is followed by an analysis of three other crossings on *one side* of the X-line, with high guide field percentages (>60%) in Section 4.4. We analyze the enhancement in the out-of-plane component with respect to the guide field and the average of the two reconnecting fields (as done in the simulation). A summary and a discussion is provided in Section 4.5.

4.2 Predictions from 2D PIC Simulation

Pritchett and Mozer, [2009] studied asymmetric reconnection in the presence of a guide field using 2D PIC simulations. The scenario they considered represented the configuration of reconnection between the MSH and MSP regions at the subsolar point. Reconnection was initiated by applying a spatially and temporally steady convection electric field at the high density/low magnetic field MSH side of the current layer to imitate driven asymmetric reconnection, which was an extension of *Pritchett*, [2008]'s work.

We present figures from *Pritchett and Mozer* [2009] when reconnection was well established, to illustrate the key findings of their study that is related to our data analysis. Coordinate system for the simulation was as follows: X was directed from the MSH side towards the MSP side of the current layer, Y was directed dawnward and Z was directed northward. In space-fixed GSE coordinate system, X would be reversed and pointing sunward (MSP to MSH) and Y would be reversed and pointing duskward.

Initial conditions of the reconnecting regions of the simulation had a density asymmetry of 10 ($N_{asym} = N_{MSH}/N_{MSP} = 10$) and a jump factor of three in the reversing magnetic field, giving a magnetic asymmetry of $B_{asym} = B_{MSH}/B_{MSP} = 0.33$. The magnetic shear angle across the current sheet was 117^o. A uniform guide field of equal strength to the reconnecting magnetic field $B_{L,MSH}$ was applied and was directed dawn-ward, i.e., along Y. Following the convention used in this thesis, this implies a guide field of $B_G/B_{L,MSH} = 100\%$. The ion beta in the MSH, $\beta_{i,MSH}$ was 3.0.

Figure 4-1 presents the normal (X) and out-of-plane (Y) components of the magnetic field. The reconnecting magnetic field B_X was not constant as a function of X (horizontal axis) and was enhanced in magnitude at the MSH separatrix (on the left). Although we cannot showcase this feature in the events chosen for this chapter, we note that the X-line was shifted southward due to the diamagnetic drift, by about $2d_i$ relative to the maximum at Z = 0 of the driving electric field on the boundary.

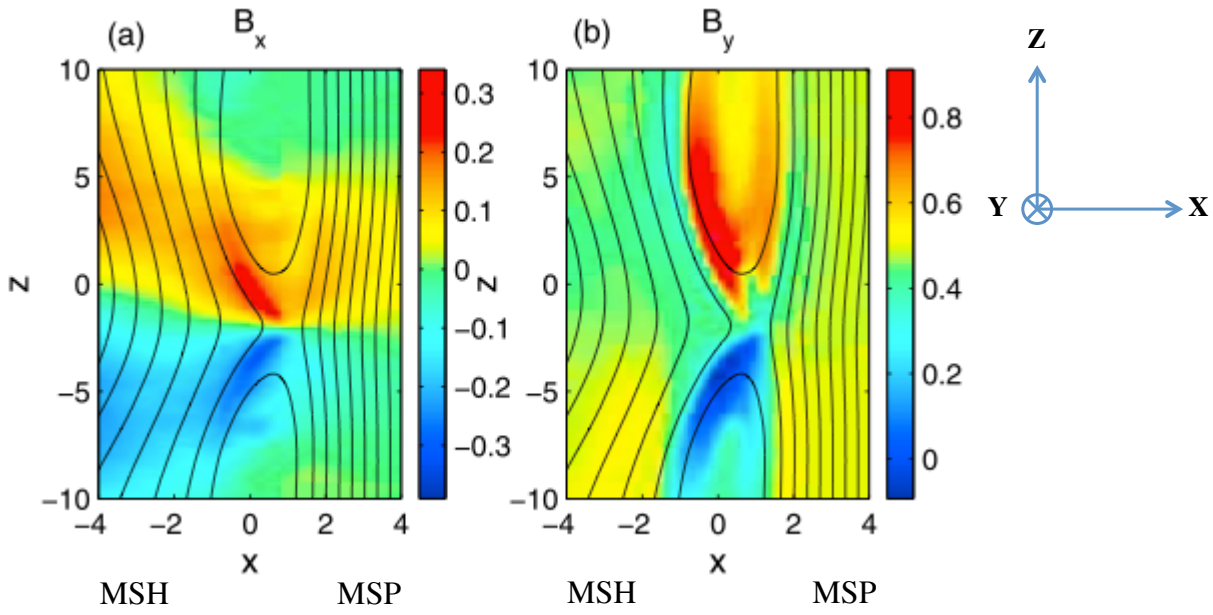

Figure 4-1: The normal (X) and out-of-plane (Y) components of the magnetic field. Left side represents the MSH while the right side represents the MSP. Reproduced from *Pritchett and Mozer*, [2009]

For a dawn-ward directed guide field, there was a significant enhancement in the B_Y field on the northern outflow region (NOR) of the X-line with a maximum of $\sim 0.9B_0$ just inside the MSH separatrix. Here, B_0 is the average of the asymptotic values of the reversing magnetic field magnitudes on the MSH and the MSP sides of the current layer (i.e., $B_0 = (|B_{MSH}|+|B_{MSP}|)/2$). Note that the in Figure 4-1(b) color bar is mostly in the positive range.

They observed a significant reduction in B_Y field in the southern outflow region (SOR) of the X-line; the field even changed sign in the small region inside the MSH separatrix (dark blue in the MSH side indicating opposite polarity). The weakening and enhancement of the Hall magnetic fields in NOR and SOR was what was phrased as the North-South asymmetry about the X-line.

Figure 4-2 shows the Z component of the bulk ion and electron flow velocities and the resulting current density J_Z. They noted that the ion outflow in the NOR peaked along the MSP separatrix (to the right) and extended on either side of the right half of the outflow region and into the MSP (i.e., outflow jet is biased towards the MSP side of the current layer. See also *Tanaka et. al.,* [2008]). In the SOR, the ion outflow was weaker, and filled the entire island. Furthermore, the electron flow was strongly concentrated on the separatrices. This represented the electron flow from the high density side (MSH) to the low density (MSP) side of the layer. Electron flow was much larger than the ion flow and this, in turn, determined the current density.

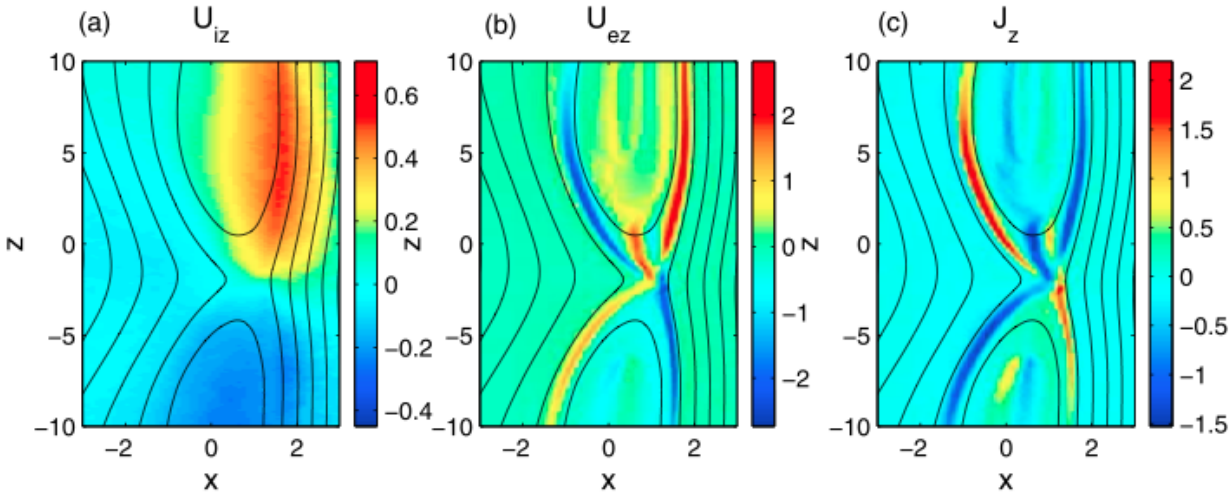

Figure 4-2: Z component of the bulk ion (a) and electron (b) flow velocities and the resulting current density J_Z (c). Left side represents the MSH while the right side represents the MSP. Reproduced from *Pritchett and Mozer*, [2009].

This in-plane Hall current strengthens the B_Y field just inside the northern MSH separatrix (left side) and is the cause for the B_Y structure seen in Figure 4-1(b). J_Z reinforces B_Y to a lesser degree just inside the MSP separatrix (right side). In the southern hemisphere, the B_Y field is reduced in magnitude (and even reversed). Apart from the electron

flow along the separatrices, an important feature they noticed was a distinct outflow in the center of the northern island, starting at the X-line, that extended several d_i away from the X-line as seen in Figure 4-2(b), and a weaker return flow next to the outflow in the MSP side. This created a velocity shear layer in the immediate vicinity of the X-line, and the resulting current density, continued to weaken the B_Y field in this region. Data examples presented in the Section below shows this feature. Note that this feature was not present in the SOR, since there was no electron shear layer in the southern side.

Figure 4-3 shows the X and Z components of the electric field. There was a strong MSH directed E_X component. This E_X component plays a role of opposing the ion inflow from the MSH side and maintaining charge neutrality with much less dense population of MSP electrons. E_Y and E_Z are much weaker; the reconnection E_Y field being the weakest and uniform over the whole island region (not shown) and E_Z mainly along the separatrices with large values at the MSP separatrix.

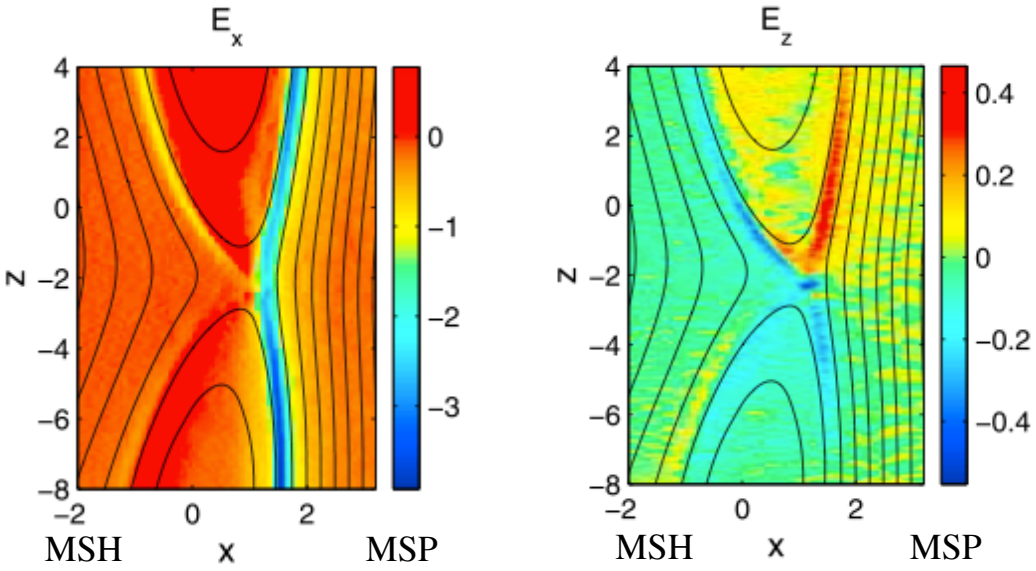

Figure 4-3: The X and Z components of the electric field. Reproduced from *Pritchett and Mozer*, [2009].

We now turn to data examples with a guide field.

4.3 Observations: Hall field structure on both sides of the X-line

4.3.1 Case Study 1: April 03, 2008

First, we present an event at high latitudes poleward of the southern cusp on April 03, 2008 during the interval 3:40−4:10 UT measured by C3. The spacecraft observed a clear jet reversal, therefore we use this particular event to examine the contrast between the sunward side and tailward side of the X-line. The IMF conditions during this event were extremely stable. From 3:00–7:00 UT the average clock angle was $\sim 9^0$ for the entire 4 hour duration.

At 03:30:30 UT, C3 was located at (2.59, -7.71, -9.80) R_E (GSE) and -75.96 MLAT, and at 04:00:30 UT, travelled to (2.12, -7.41, -9.53) R_E (GSE) and -76.12 MLAT. The MLT range was 08:15:32−07:37:13 h. Additionally, C3 travelled from a high density MSH region with $B_{X,Y,Z} > 0$ (GSE) to a low density MSP region with $B_{X,Y,Z} < 0$ (GSE) confirming an inbound MP crossing at high latitudes poleward of the cusp. As explained in Chapter 2, the coordinate system of the data was rotated from GSE to current sheet centered coordinates. The current sheet normal in GSE coordinates was $\mathbf{N}$ = (0.72, -0.36, -0.59) pointing from the MSP to the MSH side of the current sheet. $\mathbf{L}$ = (-0.66, -0.62, -0.43), pointed anti-sunward and contains the reconnecting fields, while $\mathbf{M}$ = (-0.21, 0.70, -0.68) is the out-of-plane component containing the guide field.

Figure 4-4 presents plasma, magnetic field and electric field measurements during the interval 3:40−4:10 UT. From top to bottom, the panels show, ion density (with electron density derived from SC potential overlaid in red), ion density in linear scale, ion temperature, B_L, total magnetic field strength, V_L, total bulk velocity, E_N, total electric field and

δ_i. The dashed blue vertical line marks the jet reversal while the two purple dashed lines bracket the interval of the two oppositely directed outflow jets. The average values of the ambient regions before and after the current sheet crossing are presented in Table 4.1.

N_{MSH}	N_{MSH}	$B_{L,MSH}$	$B_{L,MSP}$	B_G
$< 21.34 > \pm 1.04$	$< 0.21 > \pm 0.05$	$< -15.97 > \pm 2.33$	$< 39.53 > \pm 0.46$	$< 4.20 > \pm 0.56$

Table 4.1: Average density and magnetic field values of the ambient MSH and MSP, before and after the MP crossing and the guide field

The N_{asym} and B_{asym} for this event was $< 99.32 > \pm 22.6$ and $< 0.40 > \pm 0.06$ respectively. The resulting guide field was 26.28% of the reconnecting MSH magnetic field. The magnetic shear between the reconnecting fields was 159.2^o. Using average values in the ambient MSH region before the MP crossing, the beta in the MSH, β_{MSH}, was 1.86.

The B_L component showed that C3 made several attempts to cross over from the MSH to the MSP side, starting at 03:53:30 UT. These partial crossings were verified by the dips in density (not as low as MSP values) and peaks in the total temperature (not as high as MSP values). The complete crossing occurred at ∼03:57:52 UT.

C3 observed a clear jet reversal; first a tailward directed jet (jet #1) and then a sunward directed jet (jet #2). Jet #1 had a peak value of, $v_{obs,peak}$= 205.12 km/s and average $v_{obs,avg} = < 158.28 > \pm 33.48$ km/s while jet #2 had a peak value in the opposite direction, $v_{obs,peak}$= -170.67 km/s and average, $v_{obs,avg} = < -145.43 > \pm 14.09$ km/s.

C3 observed jet #2 for a longer period which may indicate that the outflow jet filled the entire sunward outflow region. The tailward directed jet #1 was stronger and its peak was more localized towards the MSP side of the CS. This is in agreement to the ion outflow pattern observed in the simulation (see Figure 4-2(a)).

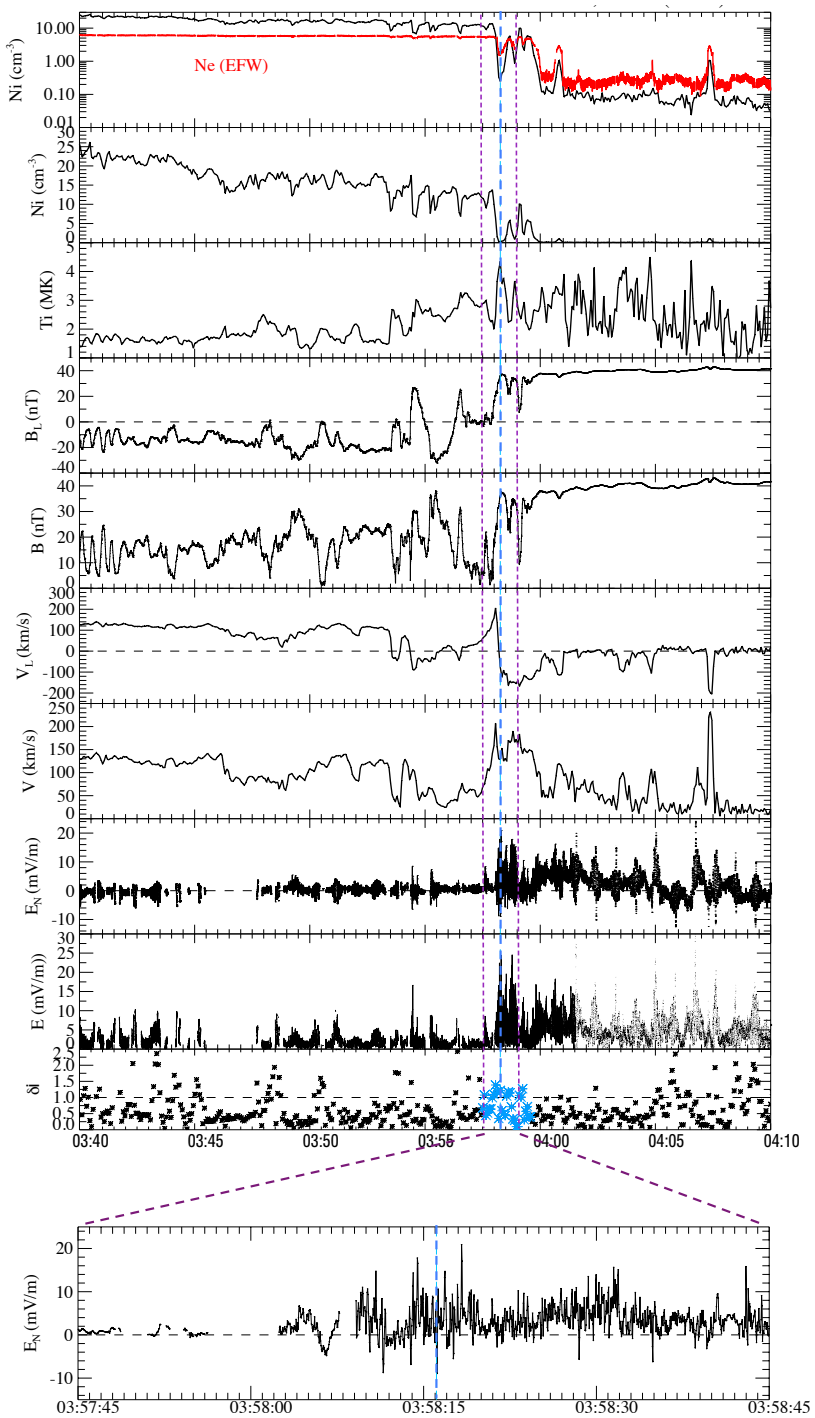

Figure 4-4: Plasma, magnetic field and electric field data from the CIS, FGM and EFW instruments, on C3 for the period 03:40−04:10 UT on April 03, 2008. From top to bottom the panels show the ion density (with electron density derived from SC potential overlaid in red), ion density in linear scale, ion temperature, B_L, total magnetic field strength, V_L, total bulk velocity, E_N, total electric field and δ_i. Bottom insert shows a 1 minute interval of the E_N component centered on the jet reversal.

Figure 4-5 is a cartoon to help visualize Cluster's orbit relative to the reconnection layer and the expected Hall field structure. Similar to Figure 3-7 in Chapter 3, the MSH field lines are shown in purple, and the MSP fields lines are in black. The trajectory during the time interval considered is marked by the green arrows, starting at the label S and ending at the label E. The thick blue arrows show the reconnection jets. The expected Hall field polarity is marked in orange while the positive guide field is marked in purple.

We turn to the Hall electric field features. As expected for asymmetric reconnection events, the normal component of the electric field, E_N showed increased activity in the MSP side [*Mozer et al.,* 2008 and Chapter 3]. To the left of the blue vertical line in Figure 4-4, in the tailward outflow jet (jet #1), E_N was more positive than negative, showing that the Hall electric fields E_N directed towards the MSH on the MSP side was stronger. See expanded view of E_N near the V_L reversal at the bottom of Figure 4-4. To the right of the blue vertical line, in the sunward outflow jet (jet #2), the measured E_N was mostly positive yet again showcasing strong MP current sheet directed Hall electric field. The total electric field peaked at $\sim$25 mV/m.

In the time interval considered, we note that the quality flag was low after 04:01:32.017 UT, i.e., data was untrustworthy after this time. However, this does not affect our electric field measurements and the δ_i calculations near the curent sheet crossing since the data set centered at the V_L reversal from 03:57:30−03:59:30 UT had a high quality flag. The last panel of Figure 4-4 shows the adiabatic parameter, δ_i rose above 1 (highlighted in blue), during the tailward and sunward outflow regions. This coupled with the strong total electric field [*Eastwood et al.*, 2008] provides confirmation of an IDR crossing during the jet reversal.

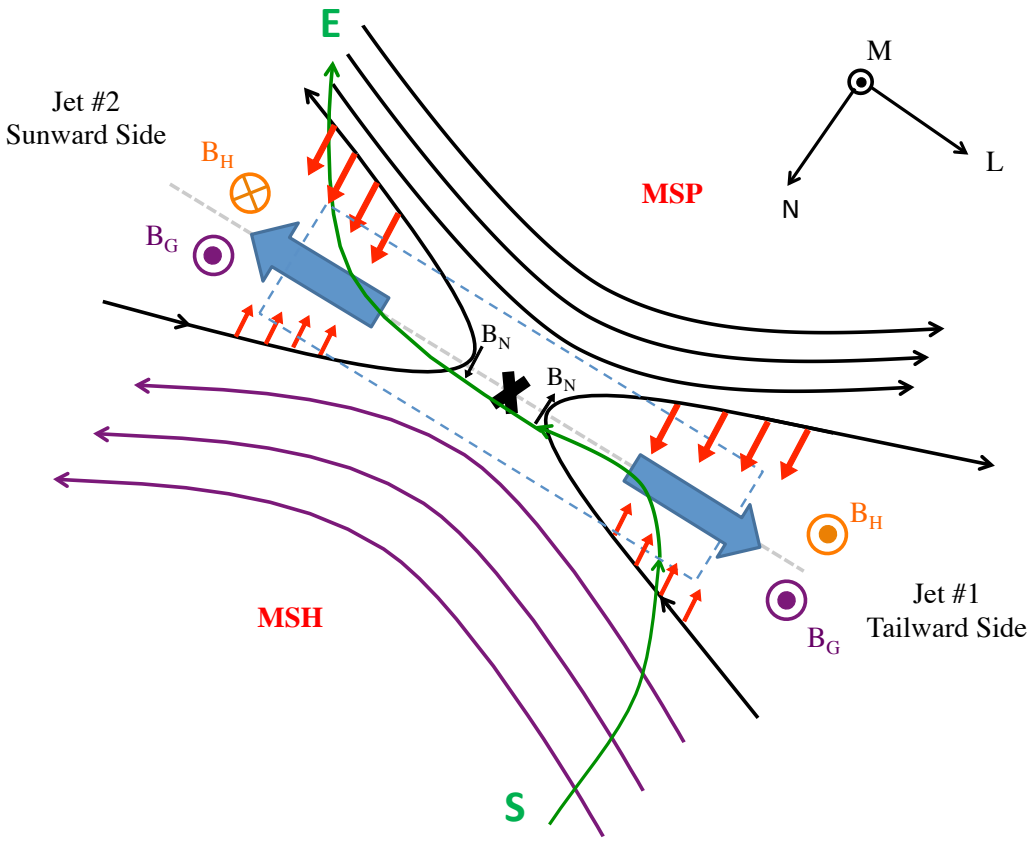

Figure 4-5: Schamatic of C3 trajectory during the interval 03:57−04:02 UT. See text above for details.

Expectations for the polarity of the out-of-plane B_M field is as follows. During jet #1, the positive (although moderate) guide field superimposes on the expected positive Hall field that arises from the Hall current. Since $B_M = B_H + B_G$, the B_M field is enhanced by B_G and expected polarity on the tailward outflow region should be overall positive and rise above the background guide field (refer to Figure 4-1(b) and schematic 4-5).

Meanwhile, during jet #2, in the sunward side of the X-line, the guide field acts to weaken the Hall field. The measured B_M should be either negative or overall below the background guide field.

In order to examine the Hall magnetic field signatures near the X-line, we zoom in to

a 1 minute interval centered on the jet reversal. Taking the time of reversal in the V_L component to be C3 passing very near to the X-line, Figure 4-6 shows measured B_M in red and B_N in black. The background guide field, B_G, taken to be uniform is represented by the horizontal purple dashed line. The left side represents the tailward outflow region ('enhanced side') while the right side represents the sunward outflow region ('weakened side'). Close to the dashed blue vertical line, B_N changes from negative to positive values as expected (Refer to Figure 4-5).

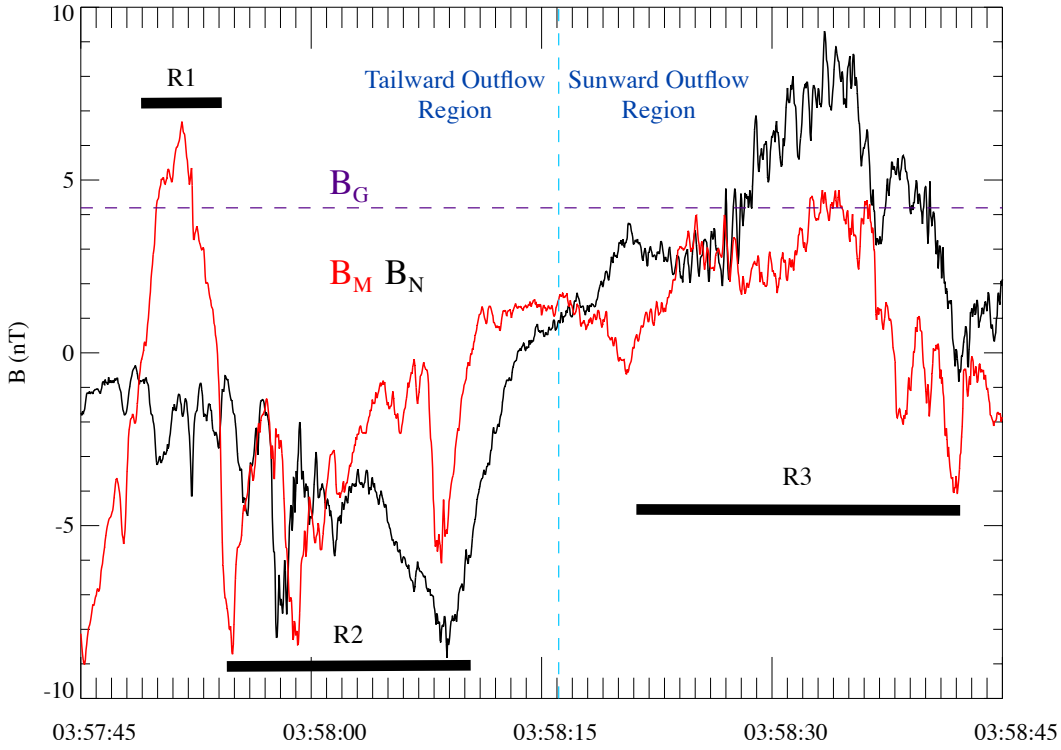

Figure 4-6: 1 minute interval of measured out-of-plane magnetic field component B_M and normal component B_N centered at the jet reversal on April 03, 2008. The background guide field is represented by the purple dashed horizontal line. The blue dashed vertical line represents the time of the jet reversal at 03:58:16.116 UT as previous figure. Left of the blue line represents the tailward outflow region and the right of the blue line represents the sunward outflow region.

Right of the dashed blue vertical line, measured B_M was mostly below the background guide field (labelled R3), and on average took a negative value matching the expected polarity during the sunward jet.

To the left of the dashed blue vertical line, at the beginning of the interval, the measured B_M changed polarity from an average of ~ -9nT to positive values, although momentarily, peaking at 6.69 nT (labelled R1). This is a 59% enhancement from the background guide field. In asymmetric reconnection, the measured B_M is expected to have a positive polarity (above purple background guide field line) during the tailward outflow region. Note that the polarity of B_M just before jet reversal (right at the X-line) was however negative. Recall that the simluations showed a distinct electron outflow in the center of the northern island, and a weaker return flow adjacent to the outflow in the MSP side (see Figure 4-2(b)). This feature implies that there is an electron velocity shear layer that extends northward from the X-line, i.e., on the enhanced side of the X-line. This in turn generates a current density (Figure 4-2(c)) that tends to weaken the B_M field magnitude by $30-40\%$ in the immediate vicinity of the X-line. The guide field of this event is not as high as the guide field in the simulation study. However, we note in Figure 4-6 that the B_M field magnitude has been weakened. Thus we ascribe the discrepancy in the polarity of B_M from the expected positive polarity to the electron velocity shear layer. This feature is seen more clearly in the next case study as well. Thus, this event provides an observational example to the Hall field structure near the X-line seen in *Pritchett and Mozer*, [2009].

4.3.2 Case Study 2: February 05, 2006

For comparison, we present another event where C1 observed a jet reversal during an inbound crossing on February 05, 2006. The interval 17:44−17:50 UT is shown in Figure 4-7(a) which presents the same panels as Figure 4-4 without the last 3 panels, due to the

lack of electric field data during this time interval. The blue dashed vertical line marks the reversal in V_L while the dashed purple lines bracket the interval where V_L changes from positive values to negative values (17:46:15-17:47:15 UT).

The guide field was $< 12.35 > \pm 2.60$ nT which was 26% of the ambient $B_{L,MSH}$.; same as Case Study 1 above. However, the density in the reconnecting regions was $< 49.40 > \pm 4.0$ in the MSH to $< 0.03 > \pm 0.007$ in the MSP giving a large asymmetry of $\sim$1725.

The jet reversal which took $\sim$10s indicates that C1 traversed very close to the X-line. The tailward directed jet (positive V_L) had a peak value of 257.12 km/s (<190.84>$\pm$ 48.11 km/s). Note that this positive V_L jet has an attenuation before the reversal. The sunward directed jet (negative V_L) peaked at -131.16 km/s (<-117.56>$\pm$ 13.39 km/s. Recall that polarity of the guide field was positive. The polarity of the V_L components then indicate that C1 measured the 'enhanced side' of the X-line first, and then crossed over the 'weakened' side. Also note that both jets are biased towards the MSP side of the current sheet. This is an expected feature due to the large density asymmetry [*Tanaka et al.*, 2008].

As before we zoom in on the interval near the V_L reversal to study the Hall field structure (Figure 4-7(b)). The blue dashed line indicates the time of V_L reversal. B_M measurements are mainly positive and above the background guide field value to the left of the blue line (labelled R1); the positive guide field has enhanced the tailward side of the X-line, as expected through simulations (see schematic in Figure 4-5). The Hall field to the right of the blue line is also positive, although much less than the left side (R3). The guide field has weakened the measured B_M field ($B_M = B_H + B_G$). Now, note the momentary drop in B_M below the background guide field (R2) very close to the X-line (V_L reversal) similar to the previous event. This again provides observational evidence of the effect of the electron velocity shear layer right next X-line effecting the measured out-of-plane field (Figure 4-1(b)).

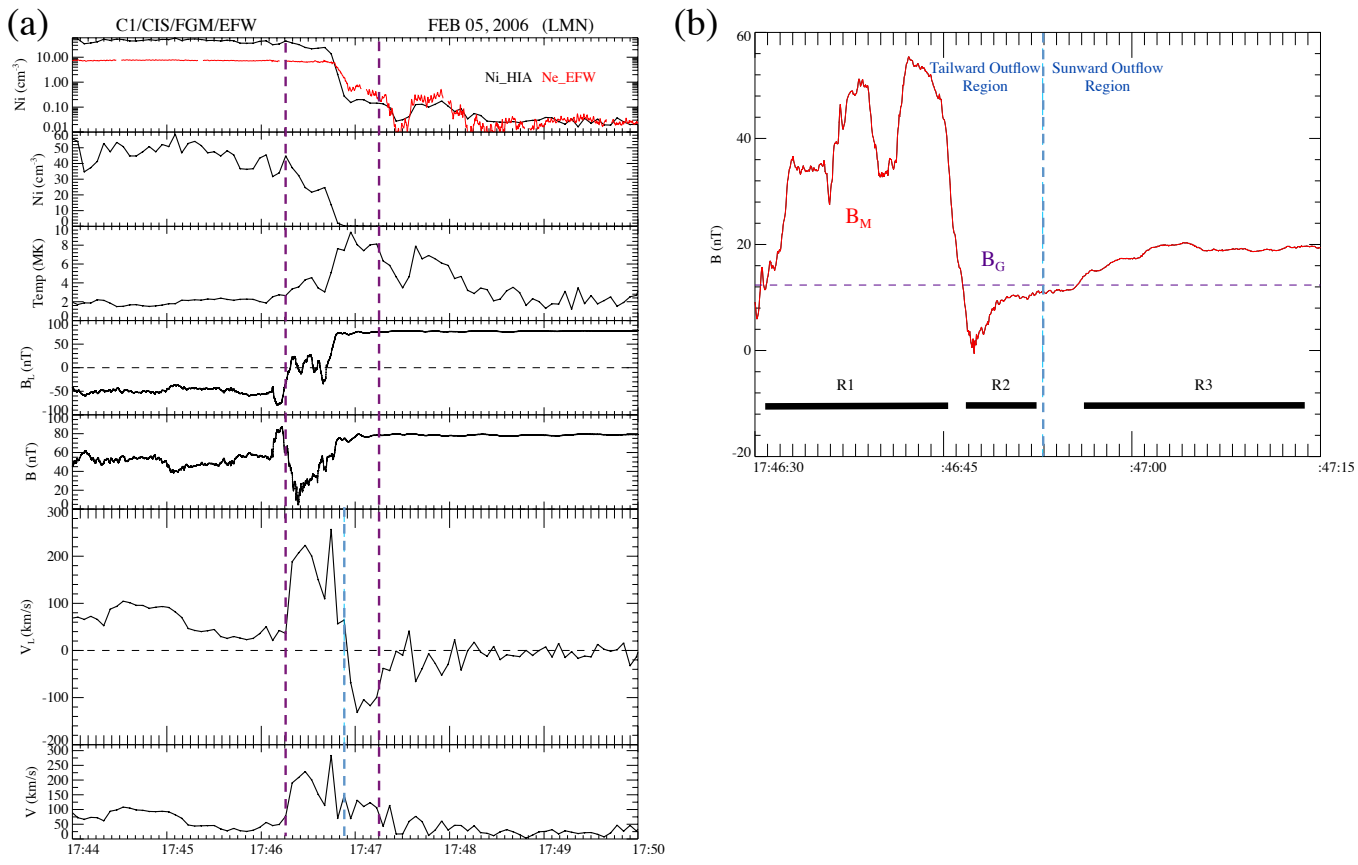

Figure 4-7: (a) shows panels same as Figure 4-4 for event on February 05, 2006 during interval 17:44-17:50 UT, without the last 3 panels due to lack of electric field data during this time. (b) shows same parameters as Figure 4-6.

4.4 Comparison of 3 events with large B_G (>60%)

We now consider 3 Cluster crossings on one side of the X-line with similar B_G% and small (<50 cm^{-3}) N_{asym} (small compared to the asymmetries that are above 3 orders of magnitude). The spacecraft crossed the 'enhanced side' of X-line in the chosen events, therefore allowing us to determine and compare the enhancement caused by the large guide field.

4.4.1 Case Study 3: April 03, 2008

We present 1 case study (Figure 4-8) in detail (Event A) out of 3, to illustrate how the enhancement with respect to the background guide field was determined.

C3 started in the dense and cold MSH region and crossed a current sheet at ∼06:41:07 UT. The LMN components in GSE along with the N_{asym} and B_G percentage are presented in Table 4.2. This sharp reversal in B_L is marked by a dashed blue veritical line. The spacecraft then encountered a sunward directed outflow jet, a large density dip of about 0.5 cm^{-3}, the peak of the sunward outflow jet V_{iL} -297.31 km/s at 06:41:47 UT (average was $< -258.64 > \pm 29.61$ km/s). The final transit to the tenuous and hot MSP region occured just after the S-line. The S-line is marked by the negative gradient in density from 06:42:01 to 06:42:07 UT and zero inflow velocity (V_N=0). Note that E_N changes from low negative values to large positive values at the current sheet crossing. This is the Hall electric field directed towards the current sheet with a higher magnitude on the MSP side reaching a magnitude of ∼25 mV/m.

We picked the interval in which the outflow jet was observed and obtained the average of the out-of-plane magnetic field component,$B_{M,avg}$, as well as the peak value $B_{M,peak}$. Enhancement of B_M with respect to the guide field was calculated as $((|B_{M,peak}| - |B_G|)/|B_G|) \times 100\%$. Similarly, in order to compare against B_0, as done in Pritchett and Mozer [2009] simulation study, the enhancement was calculated also with respect to B_0.

Results of the 3 case studies are summarized in Table 4.2. Events on April 12, 2007 [03:40-04:10 UT], February 03, 2002 [09:10 - 09:20 UT] and December 03, 2001 [10:47-10:53 UT] are presented in the table as Event A, B, C respectively. From the left to right, the columns present the event name, the current sheet normal coordinate in GSE, the magnetic local time at the MP crossing, the average density asymmetry, the guide field (percentage with respect to $B_{L,MSH}$), peak value in B_M, the average of B_M in the outflow region, and

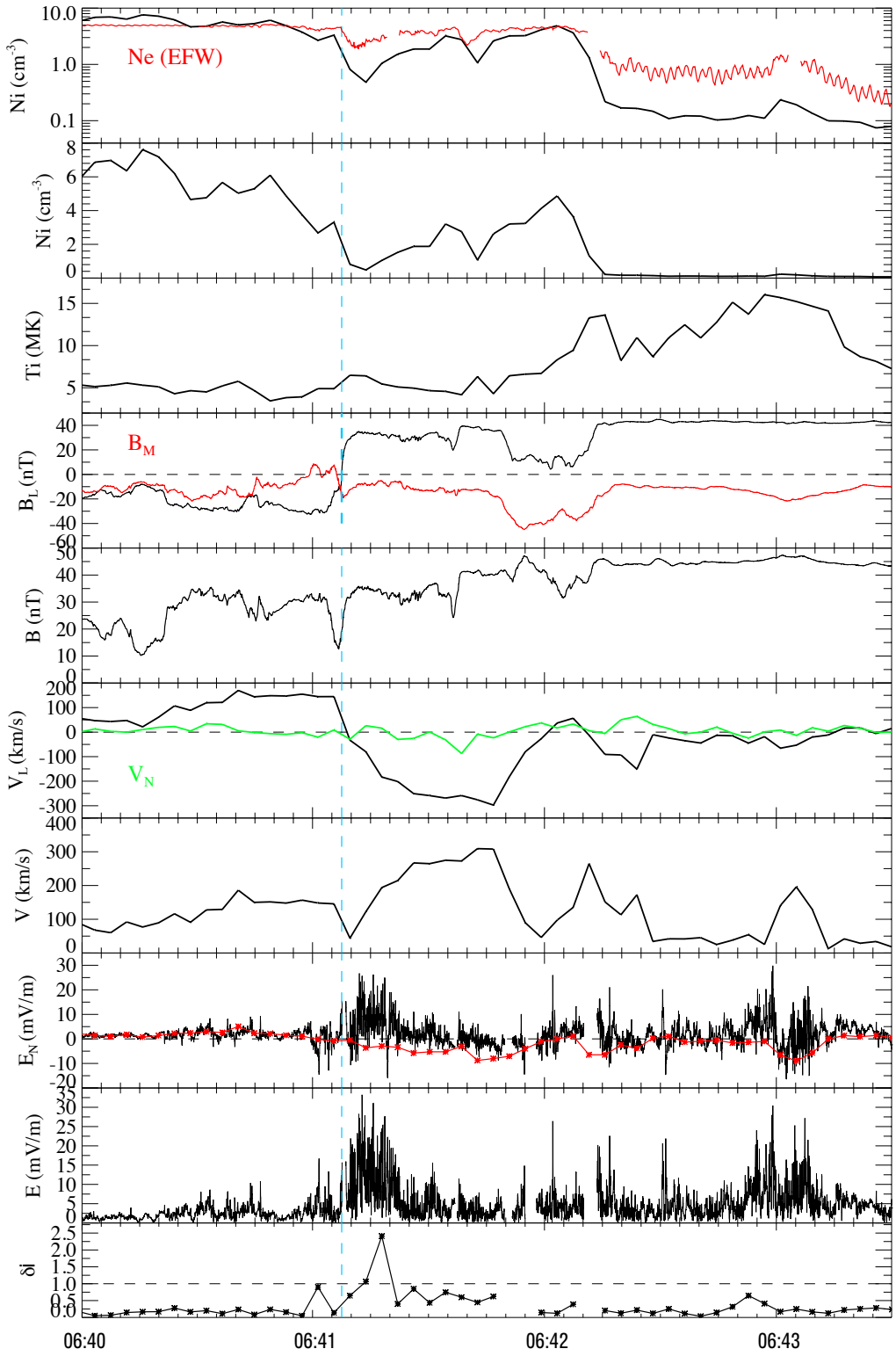

Figure 4-8: Plasma, magnetic field and electric field data from the CIS, FGM and EFW instruments, on C3 for the period 03:40−04:10 UT. From top to bottom the panels show the ion density (with electron density derived from SC potential overlaid in red), ion density in linear scale, ion temperature, B_L (B_M overlaid in red), total magnetic field strength, V_L, total bulk velocity, E_N, total electric field and δ_i.

the enhancement of the Hall field with respect to the background guide field and B_0.

4.5 Summary and Discussion

In this chapter we considered the effect of a guide field on the Hall field structure. We found good agreement with features in the observations and the features of a 2D PIC simulation in the presence of a density asymmetry of 10 and a guide field of 100% [*Pritchett and Mozer*, 2009]. From our table of events that had a wide range of asymmetries and guide fields, we picked out 5 case studies for this analysis. We first picked two events [April 03, 2008 and February 05, 2006] that have clear flow reversals and a guide field of 26% of the reconnecting $B_{L,MSH}$. We showed that the measured out-of-plane component B_M, which is a superposition of the Hall field B_H and the guide field B_G, matched the expected polarity produced in the simulations. The positive guide field weakened the Hall magnetic field in the sunward outflow region of the X-line, while it enhanced the Hall field in the tailward outflow region showing a sunward-tailward asymmetry about the X-line. Additionally, the data showed that at the vicinity of the X-line on the 'enhanced side' of the X-line, due to an electron velocity shear layer, the Hall field was weakened, and changed polarity. This feature was also predicted in the simulations.

The measured normal component of the electric field, E_N was stronger on the MSP side and was directed towards the MSH side. This matched the expected Hall electric field configuration predicted by asymmetric simulations.

In the 'enhanced side' of the X-line, the outflow speed was much higher than the other side. The peak in outflow speed was localized towards the MSP separatrix. The outflow jet on the 'weakened side' was weaker and was measured for a longer duration, indicating that it filled the entire outflow region. This too is in agreement with the 2D PIC simulations.

In addition to the two flow reversal events, we also compared three cases of crossings

Event	CS normal coordinates	MLT at MP crossing	N_{asym}	B_G (%)	$B_{M,peak}$	$B_{M,avg}$ in outflow region	$B_M\uparrow$ w.r.t B_G	$B_M\uparrow$ w.r.t B_0
A	L = (-0.73, -0.24, -0.64)	06:47:57	$< 8.59 > \pm 3.7$	$< -12.85 > \pm 2.77$ (62%)	-19.31	$< -16.40 > \pm 2.05$	50%	39%
	M = (0.16, 0.85, -0.05)							
	N = (0.66, -0.47, -0.59)							
B	L = (-0.27, 0.25, -0.93)	11:48:10	$< 46.56 > \pm 19.81$	$< -21.34 > \pm 2.06$ (72%)	-32.16	$< -23.16 > \pm 5.35$	51%	56%
	M = (-0.14, 0.94, 0.30)							
	N = (0.95, 0.21, -0.22)							
C	L = (-0.64, 0.58, -0.50)	18:36:00	$< 18.09 > \pm 13.27$	$< 22.95 > \pm 3.26$ (74%)	55.36	$< 37.20 > \pm 5.24$	141%	44%
	M = (0.22, 0.77, 0.60)							
	N = (0.74, 0.28, -0.62)							

Table 4.2: MP crossings with high guide field and low N_{asym}. $B_M \uparrow$ denotes the enhancement with respect to the background guide field and B_0.

by Cluster of just one (enhanced) side of the X-line. These events had a guide field range of 60-75% and small density asymmetries. We normalized the peaks in B_M with B_0 as done in the simulations and obtained an enhancement of ∼40-60% in outflow regions of these events. The enhancements with respect to the background guide field was between ∼50-140%. In the simulations, for a stronger guide field (100%), the peak enhancement in B_M was 90% of B_0. Thus these observations of Cluster crossings at poleward of the cusp are consistent with asymmetric simulation studies in the presence of a guide field.

Chapter 5

Episodic large (∼90 %) field depressions near the magnetic separatrix

5.1 Introduction

We present a detailed observational two-spacecraft study of three encounters of prominent magnetic depressions (MDs) by the Cluster spacecraft. On February 05, 2006, the spacecraft C1 encountered the MSH boundary layer (MSBL) adjacent to the MP, at high latitudes poleward of the southern cusp. The focus of this study is the distinctive characteristics of these deep MDs which have an average duration of ∼30 s and portray wave-like structures. These dropouts of magnetic field are not accompanied by rises in plasma density. Simultaneously, as C1 observed these dips, C3 which was ∼5000 km tailward and southward of C1 observed strong sunward plasma flows which also have some MDs.

The chapter is organized as follows. Section 5.2 gives an overview of the interplanetary conditions using data acquired by the ACE spacecraft. In section 5.3, we present an overview of plasma and magnetic field data on both C1 and C3 during a longer interval. This is followed by a detailed study in Section 5.4 of the MDs observed by C1 during a shorter

interval, highlighting their specific characteristics since MDs are encountered in various contexts. Section 5.5 presents an analysis of what was observed by C3 during the same time. The electron and ion properties are examined in Section 5.6 to determine the specific regions poleward of the southern cusp that the SC was traversing. We end with a summary of the characteristics of these MDs in Section 5.7, along with short discussion of possible causes of these depressions.

5.2 Interplanetary Observations

Figure $5-1$ shows interplanetary plasma and magnetic field data from the Solar Wind Experiment SWEPAM [*McComas et al.*, 1998] and MAG instrument [*Smith et al.*, 1998] on spacecraft ACE for the interval 16−19 UT, 05 February 2006. The plasma data are at ∼64 s and magnetic field data are at 0.35 s temporal resolution. From top to bottom, the panels display the proton density, proton temperature, dynamic pressure, plasma bulk speed, GSE components of the magnetic field, total magnetic field strength, and IMF clock angle.

At this time, ACE was located approximately ∼218 R_E upstream from earth and within ∼14 R_E of the Earth-Sun line. Note that the data has been shifted in time to account for the SW travel time from ACE to Earth. The IMF was northward for the entire period; B_Z was positive, with an average clock angle of 38^o from 17:00−18:00 UT.

The SW conditions during this 3 hour interval were quiet and steady. We note a few minor fluctuations in the magnetic field, in the beginning of the interval from 16:00−17:00 UT, mainly in the B_Y and B_Z components. The B_X component was constant at ∼2 nT during this time. The SW density varied from 10−20 cm^{-3} and the dynamic pressure varied between 2 and 4 nPa for almost the entire 3 hour interval (rose to 5.5 nPa after ∼ 18:45 UT). The SW speed was slow, remaining at around 350 km/s. The interval of interest in Cluster observations for this chapter was from ∼17:20−17:50 UT, so we conclude that the

SW was steady with very minor fluctuations in all parameters displayed in the plot during this time. The strongly NW orientation of the IMF was favorable for reconnection poleward of the cusp.

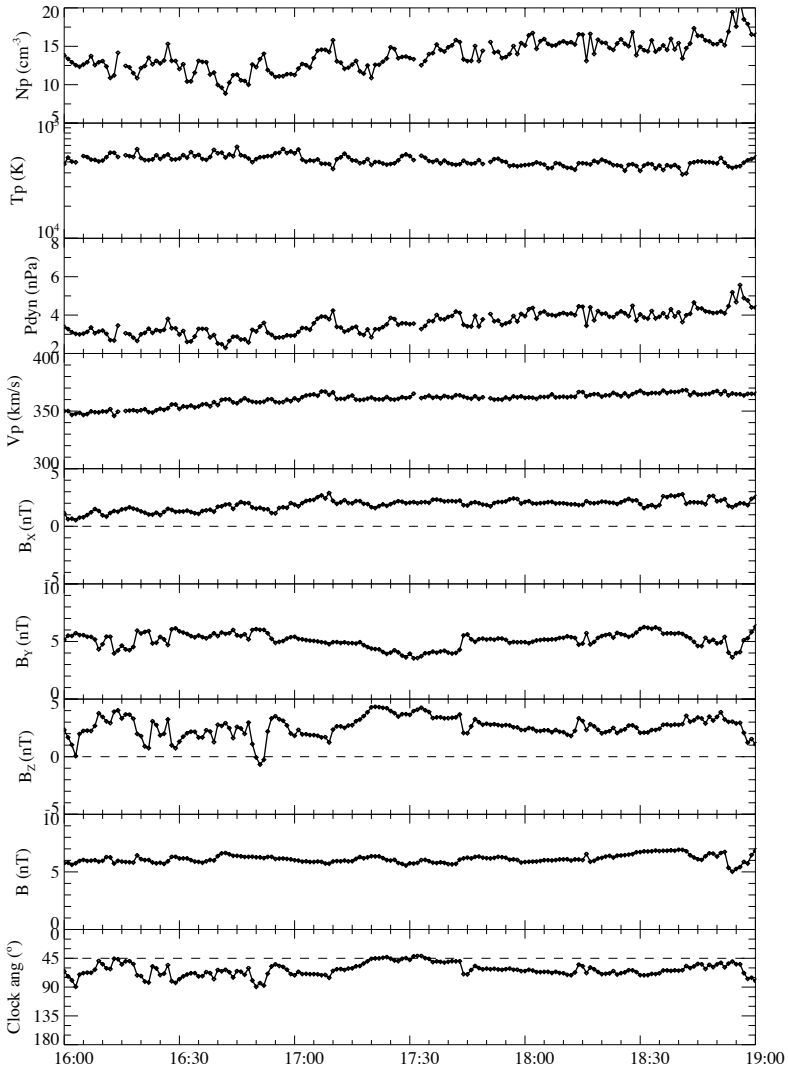

Figure 5-1: Interplanetary plasma and magnetic field data from SWEPAM and MAG on spacecraft ACE for the interval 16−19 UT, 5 February 2006. From top to bottom, the panels display the proton density, proton temperature, dynamic pressure, plasma bulk speed, GSE components of the magnetic field, total magnetic field strength, and IMF clock angle.

5.3 Overview of C1 and C3

Data from all four Cluster spacecraft during the time interval 17:20−17:50 UT on February 05, 2006 are analyzed. Figure $5-2$(a) shows the position of the spacecraft at 17:30 UT in R_E(GSE) on XZ, XY and YZ planes.

C2 was earthward and closest to C1 while C4 was sunward and southward, and was furthest away from C1. Meanwhile, C3 was tailward and southward from C1. During the interval 17:20−17:50 UT, C2 was in the MSP while C4 was in the MSH characterized by the constant low density and high density plasma respectively, and no reversal in the magnetic field components (not shown). Due to the lack of ion moment data from C2 and C4 we focus only on data from C1 and C3 for the analysis of this event.

Figure $5-2$(a) shows that the separation between C1 (black dot) and C3 (green dot) was mostly in the X and Z directions. At 17:30 UT C1 was located at (2.66, -3.50, -8.32) R_E (GSE) and C3 was located at (2.08, -3.61, -8.83) R_E (GSE). The separation distance was ∼4950 km. C3 was tailward and southward of C1.

Figure $5-2$(b) shows the trajectory of C1 and C3 in the XY and XZ (GSE) planes for the interval 17:00−18:00 UT, both moving earthward and northward with C3 leading and C1 trailing behind. At 17:30 UT, C1 was at -79^o MLAT and C3 was at -83^o and reached -81^o and -85^o by 18:00 UT. The MLT range was 08:30−10:30; i.e., C1 and C3 was at very high latitudes dawn side poleward of the southern cusp.

We then examined the magnetic and plasma parameters of C1 and C3 with measurements made by the FGM and CIS instruments for the interval 17:20−17:50 UT. Figure $5-3$ shows, from top to bottom, density in linear scale, temperature, the GSE components of the magnetic field, the total magnetic field strength, GSE components of velocity, and the total bulk speed. Measurements from C1 are in black while the measurements from C3 are overlaid in green.

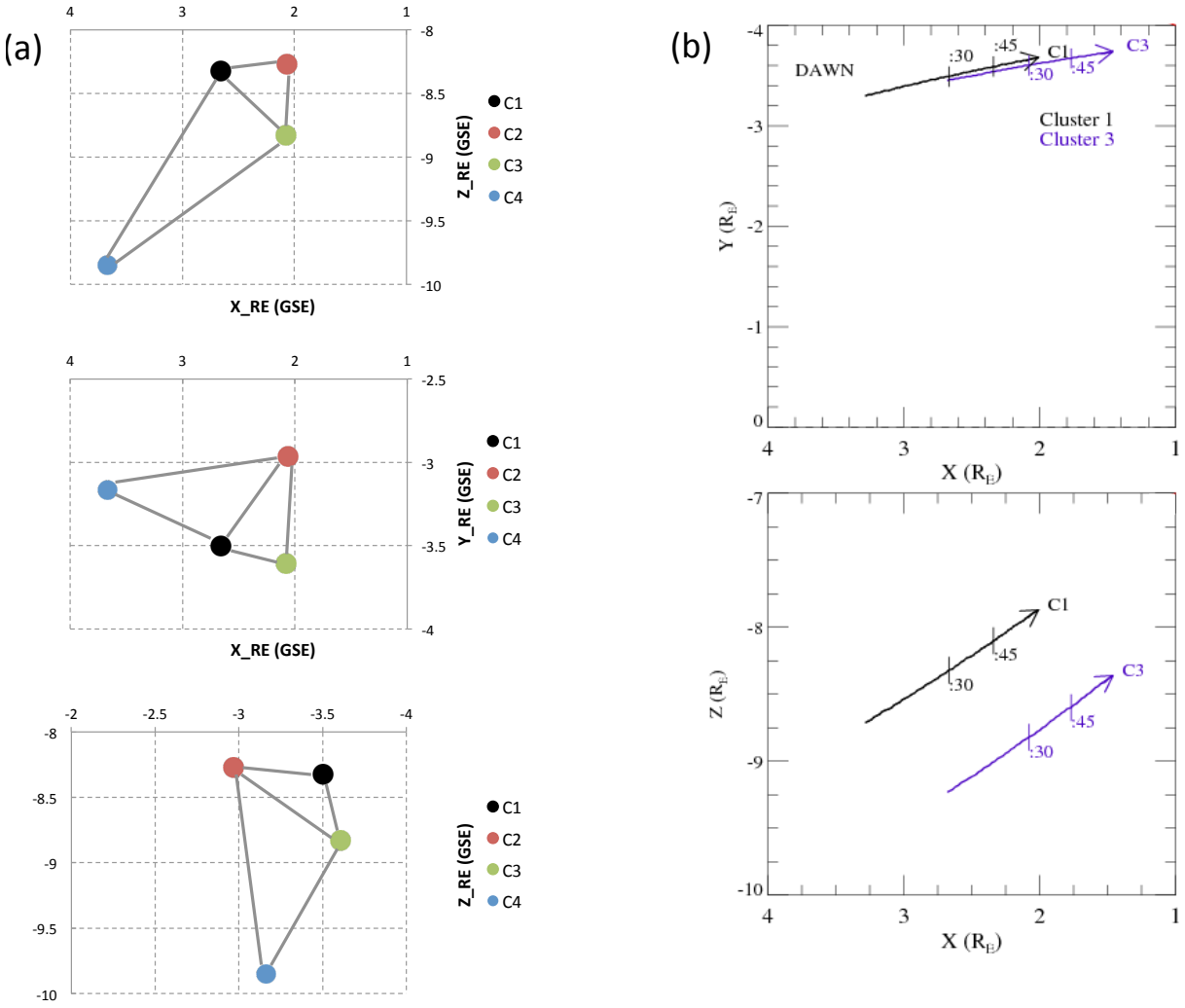

Figure 5-2: (a): Spacecraft separation of C1, C2, C3, C4 at 17:30 UT in R_E(GSE). (b): Trajectory of C1 (black) and C3 (purple) during the time interval 17-18 UT, in the XY and XZ plane.

During this 30 minute interval, there were two complete inbound crossings, first by C3 and then by C1. The black dashed vertical line at ~17:30:31 UT indicates the time at which C3 crossed the current sheet as indicated by the clear reversals in all three components of the magnetic field ($B_{XYZ} > 0$ to $B_{XYZ} < 0$). The negative density gradient, after the current sheet crossing, indicates that C3 crossed a boundary layer and finally entered the MSP region after ~17:35 UT. While C3 was in the boundary layer, the spacecraft observed a continuous high speed flow for about 5 minutes (thick blue bar). The start and end points

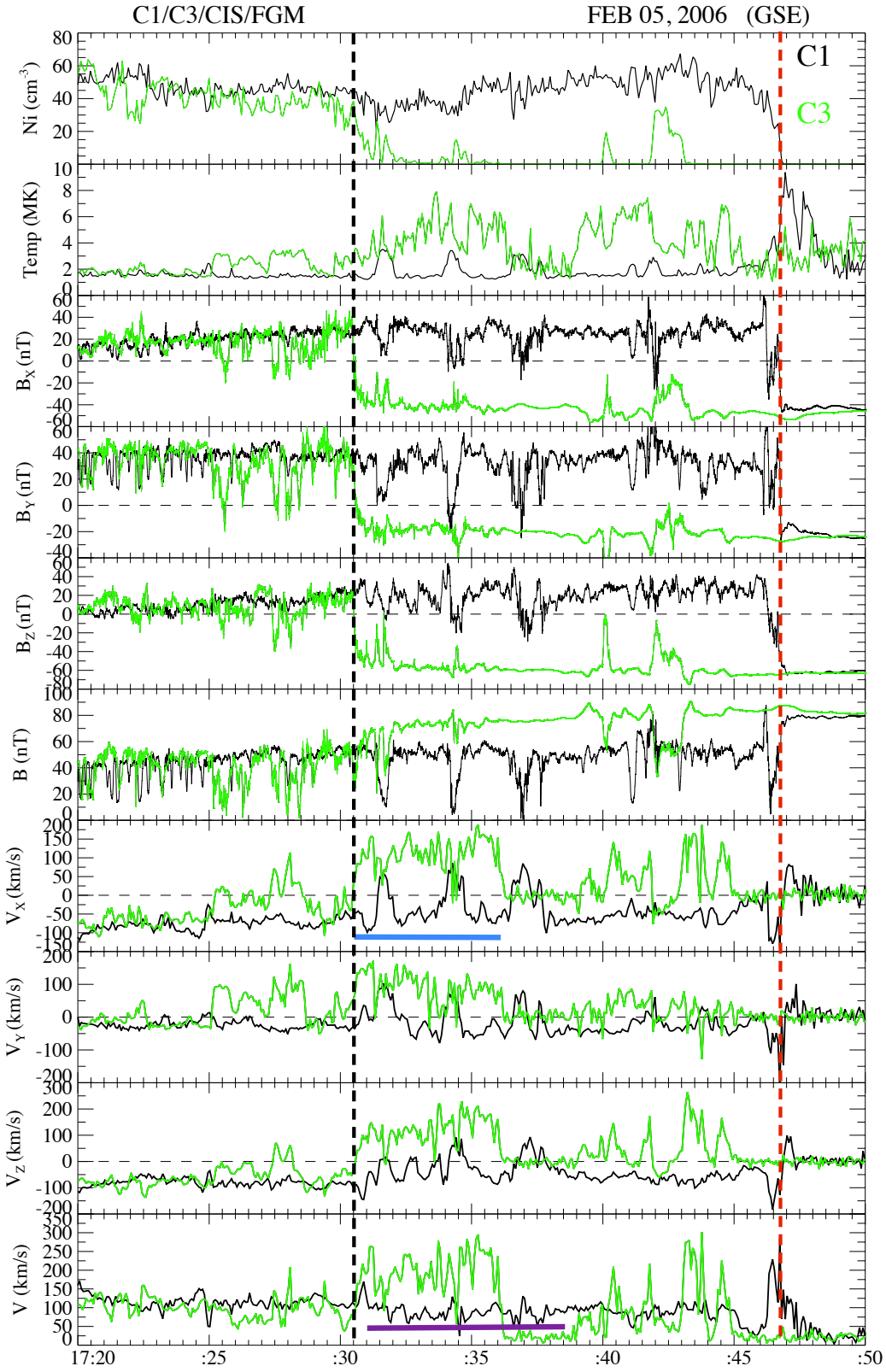

Figure 5-3: Magnetic field and plasma data from the FGM and CIS instruments on C1 and C3 for the period 17:20−17:50 UT. From top to bottom the panels show density linear scale, temperature, the GSE components of the magnetic field, the total magnetic field strength, GSE components of bulk speed, and the total bulk speed.

of this increased flow feature are well defined; there was a clear rise and fall of the velocity in all three components with an average total velocity of ∼250 km/s. The flow is sunward, northward and duskward as expected for a reconnection outflow in this region. Note the sporadic dips in the total magnetic field (panel 6) with a prominent one being at 17:31:30 UT. We shall discuss this feature further in Section 5.5. There was a density asymmetry of over 3 orders of magnitude (∼ 1270) during this crossing. The magnetic field asymmetry was 0.40. When C3 was crossing the current sheet, C1 was in the MSBL, as we shall show through a study of ion and electrons spectra to be presented later.

At the beginning of the interval, from ∼17:20−17:25, it is apparent that C1 observed mirror mode waves illustrated by the fluctuating behavior in the magnetic field and density. The oscillating dips in magnetic field strength correlated to increases in density as expected in mirror mode waves. Furthermore, the condition for the mirror instability [*Southwood and Kivelson,* 1993]

$$\frac{T_\perp/T_\parallel}{1+\beta_\perp^{-1}} > 1 \tag{5.1}$$

was fulfilled (not shown). C1 then observes 3 prominent and smooth (decreased fluctuations) dropouts of the total magnetic field during a 6 min interval, 17:31 − 17:38 UT. These prominent dips were observed by C1 while C3 was observing the strong sunward reconnection jet. We analyze this closely in the next section.

At around 17:46:25 UT (dashed red vertical line), with an abrupt decrease in density, C1 made an inbound crossing into the MSP during which the spacecraft observed a jet reversal indicated on all 3 components of the bulk velocity. C1 first observed an accelerated southward and tailward jet ($V_X < 0$ and $V_Z < 0$) that reached up to ∼275 km/s and then a northward and sunward jet ($V_X > 0$ and $V_Z > 0$) that reached up to ∼125 km/s in the opposite direction. Aspects of this flow reversal was examined in the previous chapter. After ∼17:48 UT, C1 and C3 were both in the MSP.

5.4 Analysis of Magnetic Depressions observed by C1

We now focus on the measurements of deep magnetic depressions (MDs) and the associated patterns in density, temperature, bulk flow and pressure observed by C1 during a 10 minute period, 17:20−17:40 UT. From top to bottom, the panels in Figure $5-4$(a) show the ion density, ion temperature, GSE components of the magnetic field, and total magnetic field strength. The last panel plots the mirror instability criteria, i.e., the value of $\frac{T_\perp}{T_\parallel} - 1 - \frac{1}{\beta_\perp}$. Figure $5-4$(b) presents the GSE components of the velocity, total bulk speed and the pressure. The total plasma pressure (P_{tot}) in black, with ion pressure (P_i), magnetic pressure (P_b), electron pressure (P_e) overlaid in blue, red and green respectively. We assumed that $T_i = 8T_e$ as *Stasiewicz et al.*, [2001] did for the P_e calculation. The shaded grey areas in both Figures $5-4$ (a) and (b) mark the intervals of deep MDs while the purple vertical lines mark the total magnetic field minimum inside the MDs.

The three MDs were observed in the interval 17:31−17:38 UT in the MSH side of the CS, and were roughly equally apart with an average duration of ∼30 s. The average ambient magnetic field strength just before this interval (17:29:00 −17:31:00 UT) was 52 nT. As the vertical purple lines guide us, the depression in magnetic field becomes deeper and deeper (closer to zero) as we progressed. We shall name the depressions MD1, MD2, MD3, respectively. The minimum value of the magnetic field strength during these depressions are, 10 nT, 4.3 nT, and 0.6 nT. Accordingly, the deep MDs were a significant 81%, 92%, 99% drop from the ambient magnetic field. Note that the ambient magnetic field components do not rotate across the MDs. This implies that the MDs were not entrained on a discontinuity unlike some magnetic holes in the solar wind. These types of decreases in magnetic field strength with less than 5^o directional change in the ambient field were termed as 'linear holes' by *Turner et al.*, [1977].

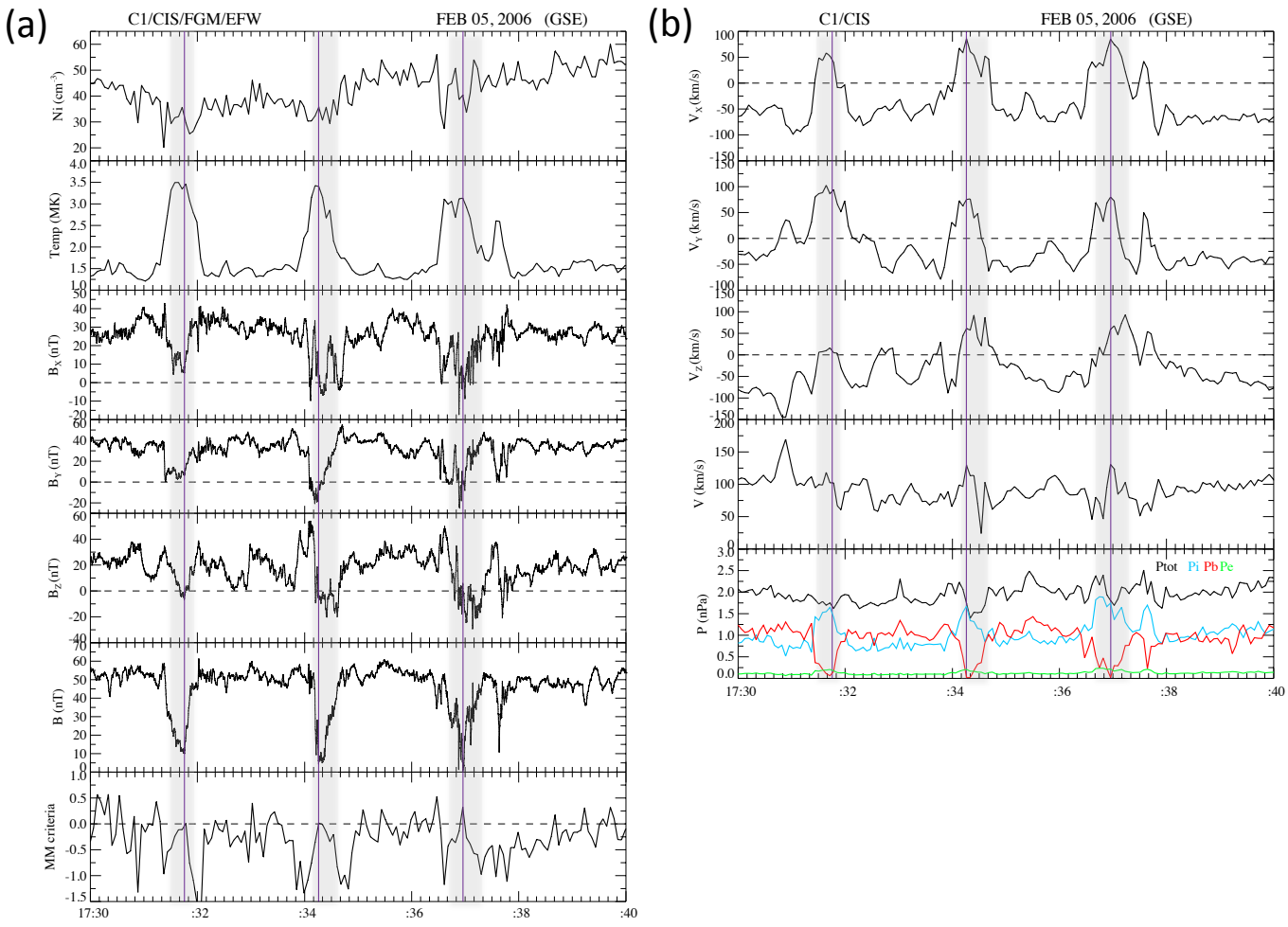

Figure 5-4: Plasma and magnetic field data from the CIS and FGM instruments on C1 for the period 17:30−17:40 UT. From top to bottom the panels on Figure (a) shows ion density in linear scale, ion temperature, the GSE components of the magnetic field, the total magnetic field strength and the mirror instability criteria. Figure (b) shows the GSE components of the ion bulk velocity, total bulk velocity and the total pressure (black) with plasma pressure, magnetic pressure, and electron pressure overlaid in blue, red and green respectively.

All 3 MDs are further hallmarked by a three-fold rise in temperature. The MDs were not associated with density rises at the center of the MDs. The average ambient density

before the magnetic depression interval (17:27 − 17:30 UT) was 46 cm^{-3} while the average ambient temperature during that same time interval was ∼1.5 MK. Using ambient plasma parameters in the MSH, the Alfvén speed $c_A = B/(\mu_0 n_i m_i)^{-1/2}$=167 km/s, the electron inertial length, $d_e = c/\omega_{pe}$ =2 km, the ion inertial length, $d_i = c/\omega_{pi}$ =34 km and the plasma beta, $\beta = 0.88$.

The criteria for mirror instability was generally fulfilled in the regions between the MDs, i.e., $\frac{T_\perp}{T_\parallel} - 1 - \frac{1}{\beta_\perp} > 1$. However, in the center of the MD, the value did not rise above 1.

In Figure 5-4(b), note how each MD is accompanied by significant flow deflections. These pulsed flows, almost equally spaced, showcased in all 3 components of the bulk flow velocity changing directions from negative values and peaking at a positive ∼100 km/s. I.e., they are sunward and duskward flow bursts as opposed to the ambient flow. We may infer from the the direction and strength that these flows are related to reconnection poleward of the cusp.

What's most remarkable is the fact that the total velocity during this ∼7 min interval of MDs remained relatively constant at ∼90 km/s, more visible in the last panel on Figure 5-3 (thick purple bar).

The last panel of Figure 5-4(b) gives insight to the pressure during this interval. The ion pressure, P_i rises at the center of the MDs while the magnetic pressure, P_b drops. The electron pressure was almost negligible but may vary since the values were derived under the assumption of $T_i = 8T_e$. However, the total pressure (black trace), $P_{tot} = P_i + P_b + P_e$ stayed roughly constant. We conclude that it was the rise in temperature, i.e., the heated plasma that was keeping the pressure balanced inside the MDs.

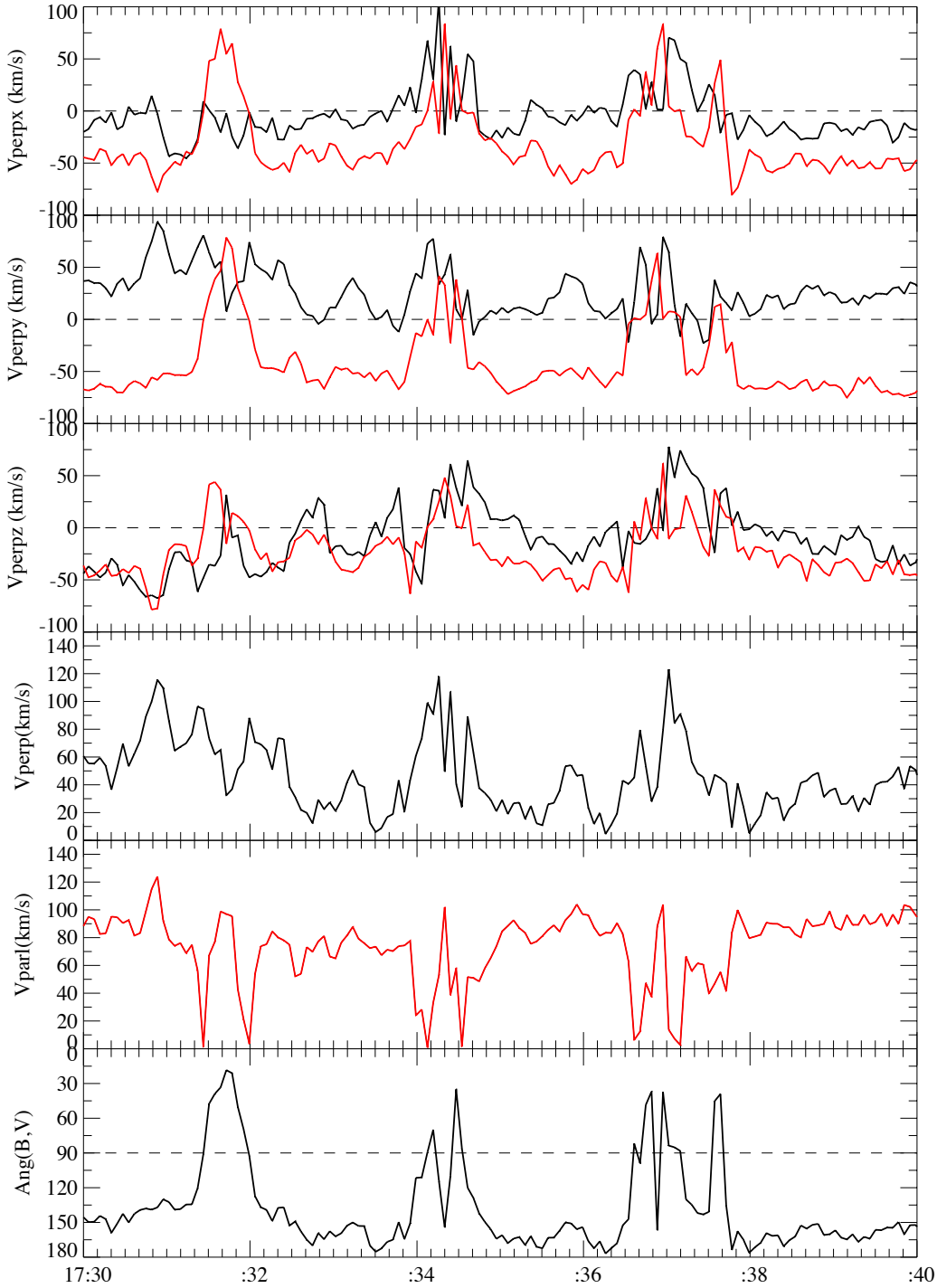

Figure 5-5: Perpendicular (black) and parallel (red) components of the bulk velocity and the angle between the the magnetic field and velocity during time interval 17:30−17:40 UT.

Figure 5-5 shows the components of the velocity perpendicular (black) and parallel (red) to the magnetic field and angle between the veloctity and magnetic field vectors. At the edges of each MD the flow was perpendicular to the field ($v_{\parallel} = 0$). At the center, the flow was closely aligned to the field (parallel or antiparallel) showcasing a vortex-like behavior.

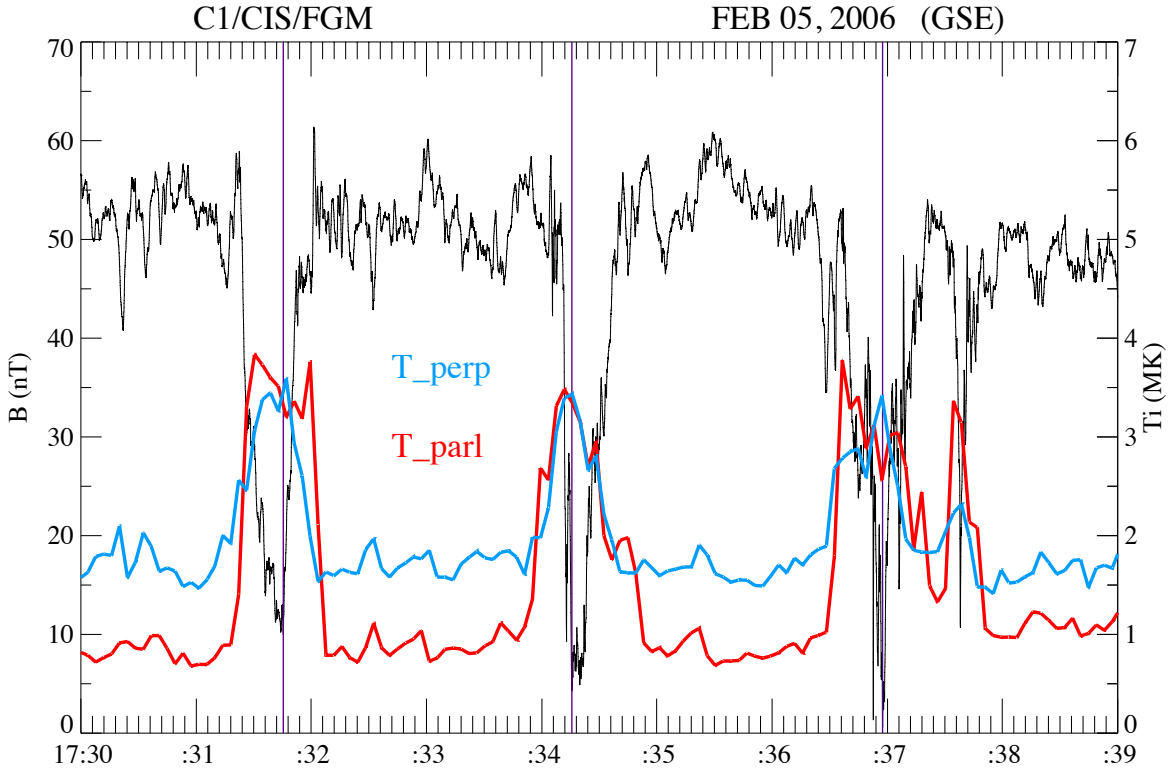

Figure 5-6: Total magnetic field with parallel and perpendicualr temperature for the time interval 17:30−17:39 UT

A closer look at the features in ion temperature are presented in Figure $5-6$. We note two significant trends in the behavior of the parallel (red) and perpendicular (blue) temperature of ions inside the MDs: (i) strong temperature rise in both $T_{\perp}$ and $T_{\parallel}$, and (ii) the temperature was isotropic. Additionaly, these MDs are embedded in a layer that

was characterized by a temperature anisotropy; the perpendicular temperature was ∼1 MK higher than the parallel component outside the MDs $T_\perp > T_\parallel$. Hence we concluded that an important characteristic of MDs was that the ion temperature is high and isotropic at the center.

Next, we shall study the field and flow phenomena observed by C3 during the same time interval.

5.5 Observations from C3

Figure 5-7 shows plasma and magnetic field data on C3 for the same time interval as C1 above. Top to bottom, the panels show the ion density, ion temperature, XYZ components of the magnetic field, total magnetic field, XYZ components of the velocity, and total bulk speed. The purple vertical lines still represent the times of the total magnetic field minima inside the deep MDs measured by C1. Recall that at 17:30:31 UT, C3 was southward and tailward of C1 (Figure 5-2(b)). At the beginning of the interval, although there is an abrupt change in polarity in the magnetic field components, the density and temperature changed gradually indicative of a boundary layer crossing. The spacecraft observes 3 clear dips in the magnetic field strength while crossing the boundary layer before 17:32:00 UT and another at 17:34:20 UT. These dips were not as drastic as the deep MDs observed by C1. Also, in this case the magnetic dips are accompanied by density rises (top panel). The dips in magnetic field observed by C3 are not due to mirror mode instability since the $\beta_\perp$ was very small (not shown).

Last four panels show that C3 observed a well defined, continuous flow from 17:30:30-17:36:10 UT with a peak value of ∼300 km/s. These flows are sunward, duskward and northward.

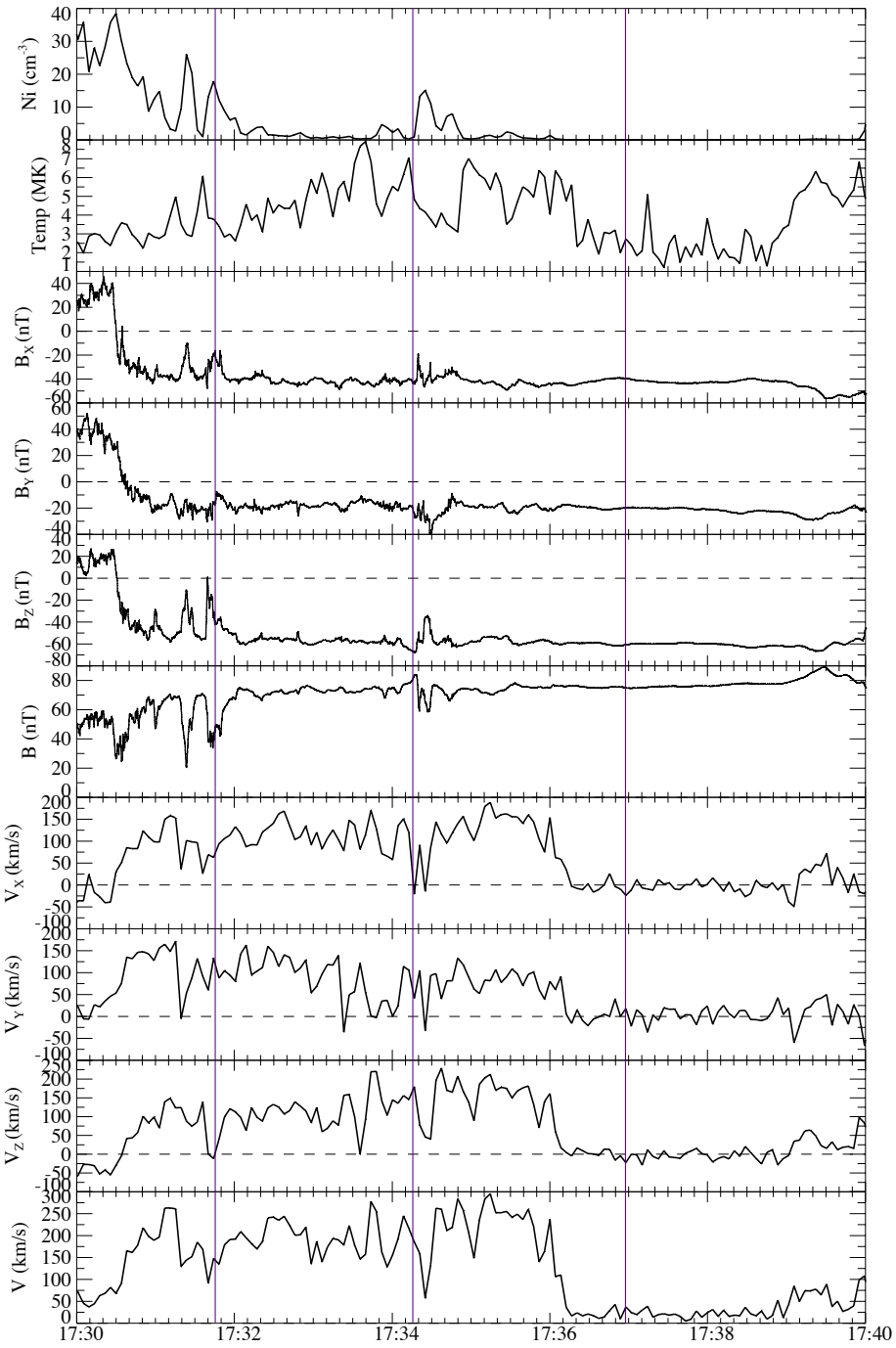

Figure 5-7: Plasma and magnetic field data on C3 for the period 17:30−17:40 UT.

5.6 Electron and ion behavior during the deep MDs

We now focus on the electron and ion behavior on C1, specifically the energization and directionality, during the same longer interval as Figure $5-3$. Behavior of heated electrons and ions help distinguish the distinct boundary layer regions near the MP associated with high latitude reconnection [*Onsager et al.*, 2001]. Electron data from the PEACE instrument [*Johnstone et al.*, 1997] and ion data from HIA instrument [*Reme et al., 1997*] instrument were used for this purpose. In Figure $5-8$ we show data from both the LEEA (Low Energy Electron Analyzer) and HEEA (High Energy Electron Analyzer) sensors, with typical respective energy ranges from 0.6 eV $-$ 1 keV and 35 eV $-$ 26 keV. The CIS-HIA instrument has an energy range of 5 eV$-$32 keV. First three panels show the electron energy flux spectrograms for electrons that are flowing parallel, anti-parallel and perpendicular to the magnetic field respectively. The last 3 panels repeat the spectrograms for ions. As in previous figures, the purple dashed vertical lines mark the times of the magnetic field minima of MD1, MD2, and MD3 observed by C1.

We will first study the regions before (R1) and after (R3) the layer with MDs. Throughout most of the interval, from 17:20 to 17:47:50 UT, C1 detected dense MSH$-$like plasma; the electron population was below $\sim$100 eV and ion population was below 800 eV. During the interval just before the MDs for example, from 17:25$-$17:30 UT labelled R1, the electron energy spectrogram was isotropic; the parallel and anti-parallel electron fluxes was balanced. Meanwhile, $T_{e,\perp} \approx 300$ eV and $T_{e,\parallel} \approx 200$ eV which are typical values for pristine MSH electrons. With $T_{\parallel} \leq T_{\perp}$ we confirm that C1 was in the MSH for most of the interval shown, specifially before observing the MDs. Additionally, C1 observed low electron flux at higher energies compared to the region just before the MP crossing, continues to confirm that C1 was in the MSH, magnetically disconnected from the Earth's field [*Onsager et al.,* 2001]

In comparison, towards the end of the interval near the current sheet crossing when C1 observed a flow reversal, marked R3 (not the focus of this chapter), electron flux at higher energies averaged over all directions, gradually increased. This increase was due to both anti-parallel and perpendicular electron flux increasing. This is a signature of C1 observing field lines magnetically connected to the earth either inside or outside the MP, or very near the diffusion region [*Onsager et al.,* 2001]. Also, this signature of enhanced energetic electrons is due to particle heating at the current sheet. Subsequently, the abrupt decrease in electron fluxes at energies below 300 eV and ion fluxes at energies below 5 keV confirms that at around 17:47:50 UT C1 moved from open field lines to closed fields lines of the MSP.

Note the behavior of the electrons and ions in the region marked R2; the layer in which the MDs were observed. The heated electron flux in the parallel direction was fluctuating but on average greater than the flux in both anti-parallel and perpendicular directions, i.e., there is an excess of the most energetic electrons flowing parallel to the field. The largest increase in electron energy compared to the MSH region was in the parallel direction. Although there were a few dropouts in the parallel flux, hot electrons flowing parallel to the magnetic field between the MDs was a noteworthy feature as seen better in the pitch angle figure next. Also, the polarity of the B_Z component was mostly positive during this interval which tells us that the SC was outside the MP current layer. We note that these features are of the MSBL which we confirm further using the pitch angle distribution and a schematic below.

Now let us focus on the three MDs (along the purple vertical lines). We instantly note the special behavior of the heated electrons compared to their counterparts in the other regions as pronounced humps in energy. There was an increase of heated electrons in all directions (parallel, anti-parallel and perpendicular), with the most prominent and clear increase in the parallel direction. Heated electrons rose to an energy of $\sim$500 eV in the

parallel direction, ∼150 eV in the anti-parallel direction, and ∼200 eV in the perpendicular direction. Most energetic electrons were field aligned.

The ion energy spectrograms show some similar features to the electrons (bottom three panels of Figure 5-8). During the MSBL interval (marked R2), there was a clear increase in the parallel ion fluxes. This was pronounced in the MDs themselves, reaching up to 4 keV. The antiparallel flux was depleted inside the MDs (yellow spikes) while there was a slight enhancement in the perpendicular direction (not as high as in the parallel direction). The heated ions were unidirectional (flowing along the magnetic field) at the center of the MDs.

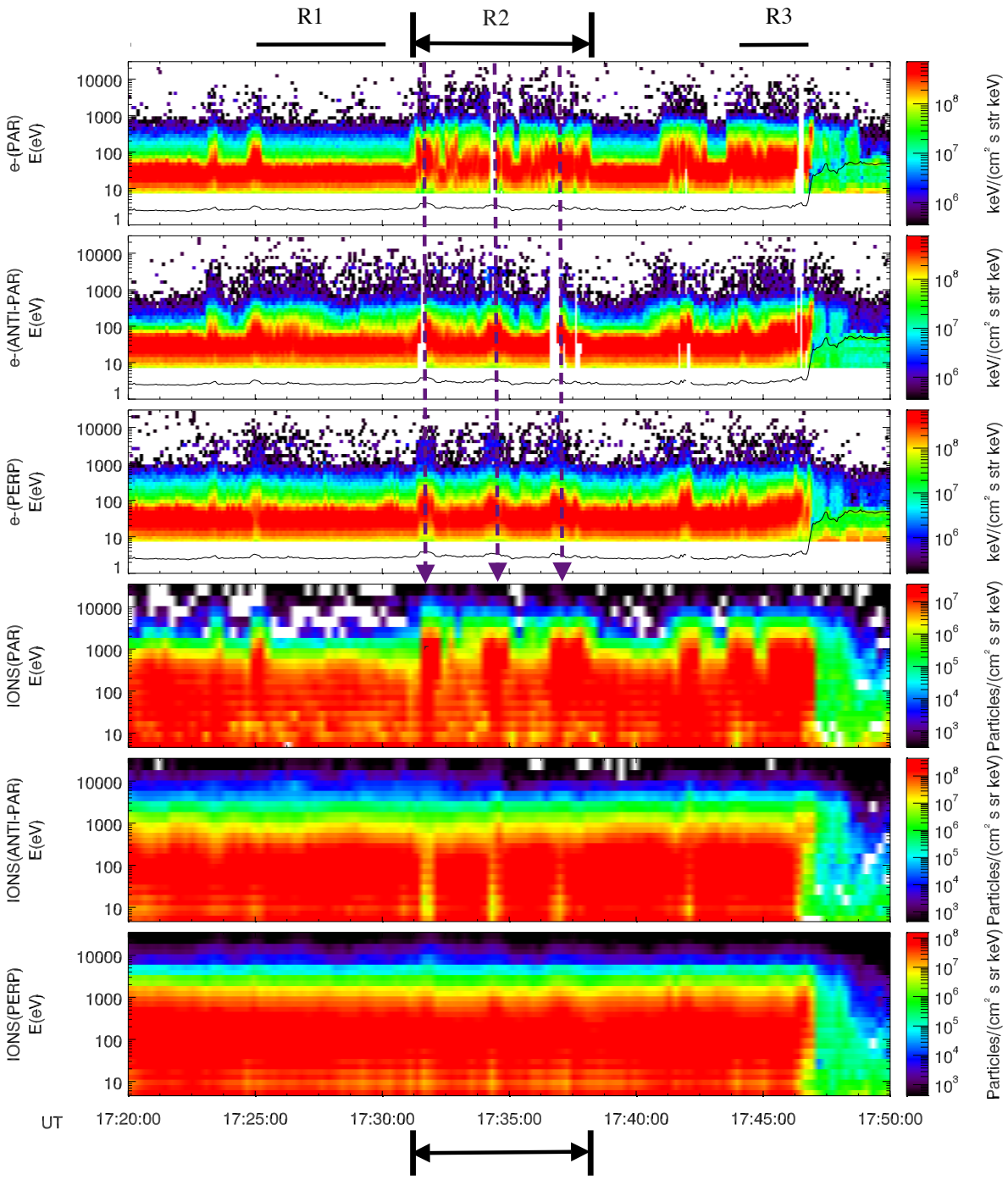

Figure 5-8: Electron and ion data from the CIS and PEACE instruments on C1 for the period 17:20−17:50 UT. Top 3 the panels show electron energy flux spectrograms for electrons flowing in parallel, anti-parallel and perpendicular direction to the magnetic field. Bottom 3 panels show the ion energy spectrograms in parallel, anti-parallel and perpendicular directions. The purple vertical lines indicate the magnetic minima in the MDs.

We will now take a closer look at the directionality of the electrons using the electron pitch angle distributions for three energy ranges, (i) low: 5−200 eV, (ii) high: 0.5 −1.5 keV and (iii) highest: 5−10 keV in Figure 5 − 9 for the interval 17:30−17:40 UT. Clear signatures are seen in the second panel. In the interval marked R2, electrons in the energy range 0.5 −1.5 keV are field aligned (pitch angle was less than 50^o). Inside the MDs (along the purple lines) the unidirectional streaming becomes isotropic. Less clear patterns are seen in the low and higher energy ranges.

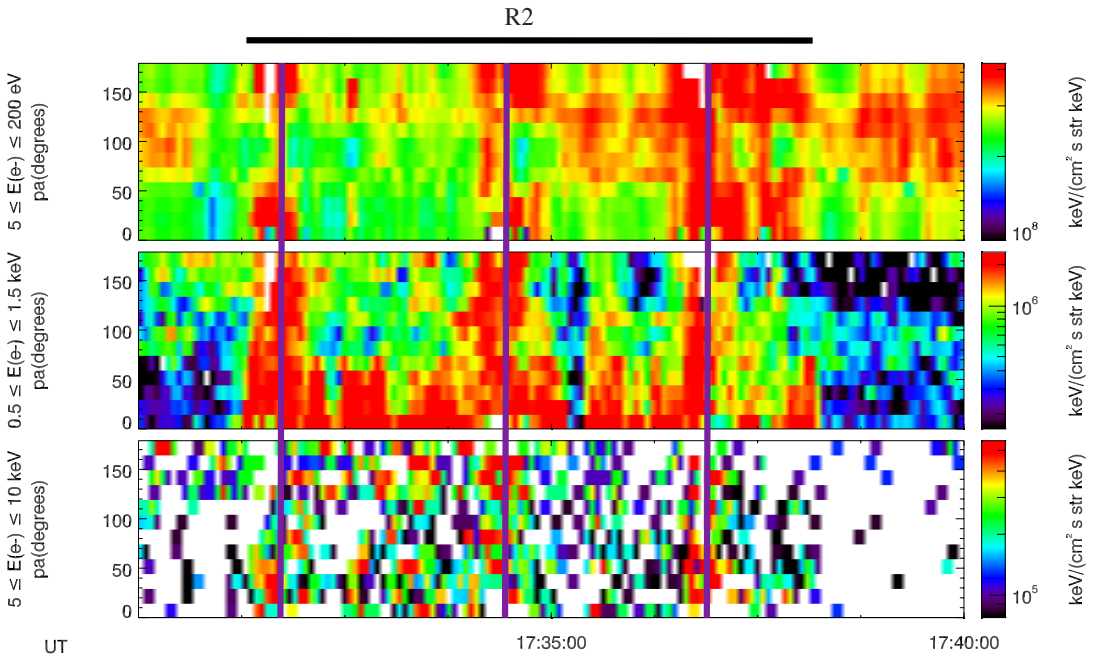

Figure 5-9: Electron pitch angle distribution for the energy range 5−200 eV, 500−1500 eV and 5−10 keV.

To visualize the different regions as inferred from the ion and electron data, we present a schematic of a situation where reconnection occurs at the southern hemisphere between the MSH (green) and MSP (blue) field lines in Figure 5−10. The dashed grey line represents the MP current layer. The orange lines represent the MSH field lines that have interconnected with the MSP field lines through reconnection poleward of the cusp. The orange field lines

outside the MP represents the MSBL (marked as R2 in Figure5-8 and Figure 5-9). The particle signatures that characterize different regions are illustrated schematically by the red arrows; with the length representing the magnitude of the parallel and antiparallel temperature of the heated electrons. C1 and C3 are marked at the time where C1 observed the MDs while C3 observed the sunward reconnection jet.

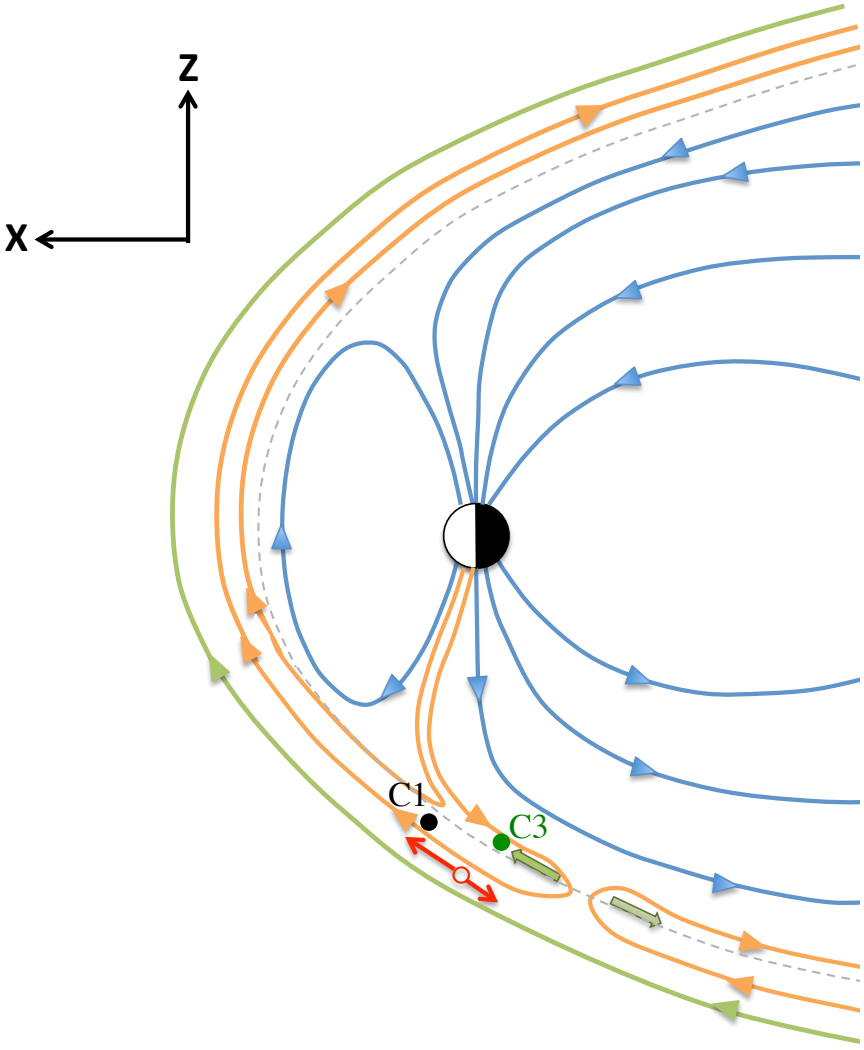

Figure 5-10: Schematic representation of the different regions encountered by C1 (black dot) and C3 (green dot) drawn from the perspective of reconnection occuring first in the Southern Hemisphere.

Assuming that reconnection has only occurred in the southern hemisphere, the MSBL is distinguished from other layers as follows; electrons and ions that flow parallel to the magnetic field are flowing out of the hot MSP and from the reconnection site where some heating has occurred. Whereas electrons flowing anti-parallel to the magnetic field are flowing from above, towards the southern hemisphere reconnection site, still having characteristics of the MSH plasma. Hence, $T_{e,\parallel} > T_{e,\perp}$[*Onsager et al.,* 2001]. The behavior of the plasma i.e., moving parallel to magnetic field, just outside the MDs confirms that C1 observed these prominent depressions in the magnetic field while traversing the MSBL.

C3 was inside the open MSP in its boundary layer and was observing high speed flows when C1 was observing the MDs in the MSBL. C1 and C3 were both in open field lines but the accelerated exhaust was not observed in C1 data. Relative positions of C1 and C3 (Figure 5-2) show that C1 was further away, so we infer from the data that C1 was in the MSBL close to the separatrix when the observations were made.

5.7 Summary and Discussion

5.7.1 Specific characteristics of these MDs

We summarize the characteristics resulting from observations of the large magnetic field depressions as follows.

Three depressions, up to a 99% decrease from the ambient magnetic field were observed, outside the MP, in the MSBL poleward of the southern cusp. One of the key differences from other studies related to prominent magnetic nulls is the fact that these MDs were not associated with increases in density. Ion temperature rose by a factor of 3 at the center of the MDs and was isotropic ($T_\perp = T_\parallel$).

C1 observed a pulsed flow pattern associated with the MDs. There was a rotation in all 3 components of the bulk flow resulting in a vortex-like structure, while the total velocity

changed very little. Outside the MDs, in the MSBL, there were heated electrons in the energy range 0.5 −1.5 keV flowing parallel to the field. Inside the MDs, the electron spectrograms showed enhancements in electron flux in all directions, but was most pronounced in the parallel direction. Through pitch angle distributions, we noted that heated electrons in the same energy range were isotropic, i.e., they showed no preference in direction with respect to the magnetic field.

We now consider possible generating mechanisms for these MDs at C1. The lack of electric field coverage during the interval considered is a strong constraint. A more thorough analysis is reserved for future work. Here, we suggest the most plausible mechanism for these magnetic depressions.

Magnetic mirror mode waves

Many studies consider magnetic holes to be a saturated state of the mirror mode instability typically attained at the inner MSH [*Tsurutani et al.*, 1982, 2011; *Winterhalter et al.,* 1994]. In linear mirror mode structures, the density rises when magnetic field drops, and drops when the magnetic field rises due to mirroring. A reason that argues against the mirror mode mechanism is the absence of a density rise associated with magnetic dips expected even in non-linear theory of mirror mode where they are saturated [*Soucek et al.*, 2008]. In addition, magnetic dips due to mirror mode instability typically appear in a mirror stable environment. However, as seen in the last panel of Figure 5-4, the surrounding environment the MDs appear in, is not mirror stable. Another reason is the rise in temperature; this is not a requirement for mirror mode waves.

Additionally, the mirror mode instability requires a high beta plasma and a temperature anisotropy where $T_{\perp}/T_{\parallel} > 1$. One may suspect that a saturation of the linear stage of the mirror mode instability could be at work. However, the mirror instability criterion was

satisfied outside the MDs but did not hold inside (Figure 5-4). Therefore, two reasons argue against the structure observed by C1 being mirror mode waves.

Kelvin Helmholtz Waves

A possibility in this specific region of observation are Kelvin-Helmholtz (KH) waves. C3 was seeing a $\sim$ 5 min long strong sunward outflow burst. The MSH flow is antisunward which results in a shear flow across the region considered and may be conducive to KH instability.

The high in temperature within the MDs questions the KH mechanism which is not expected in models of linear KH instability. However, *Treumann et al.*, [1999] stated, "Holes may also originate in nonlinear interactions between waves and plasma. For instance, large plasma eddies can be formed by the Kelvin-Helmholtz instability at the MP. This instability leads to the formation of plasma vortices where strong currents may flow at the edges of the vortex from the original magnetic field. Such a vortex would then appear as a structure similar to a hole. The formation of a magnetic hole through KH instability may depend on the configuration of the magnetic fields in the two counterstreaming plasma" (see also *Nykyri and Otto*, [2001]).

Following *Treumann et al.*, [1999], and *Nykyri and Otto*, [2001] and the fact that the plasma flow showcased a vortex-like structure, one may consider the following scenario. KH waves have become non linear and rolled over. Inside them the magnetic fields have become anti-parallel causing reconnection inside the rolled over configuration. This reconnection removes the magnetic field energy to heat the plasma. However, plausibility of this scenario requires further study with high resolution data.

Solitons

Another study associated with magnetic depressions was that of *Stasiewicz et al.*, [2003], where they showed that solitary structures detected at the MP boundary layer were slow mode magnetosonic solitons caused by the non-linear steepening of Alfvén waves. This soliton approach was initially introduced by *Baumgartel*, [1999] as an alternate mechanism for maintaining magnetic holes in an equilibrium plasma. This mechanism, too, required anticorrelation between magnetic field and density (See Figure 3 of *Stasiewicz et al.*, [2003]). The magnetic field depressions (up to 85%) were accompanied by enhanced plasma temperature. Current literature on solitons show that electric field measurements are needed. Unfortunately, due to the lack of electric field data we cannot examine this mechanism further.

Kinetic Alfvén waves

Our final scenario seems the most plausible to us. This was prompted by a study of magnetic holes by *Stasiewicz et al.*, [2001] also observed at high latitudes poleward of the cusp. The authors proposed that the magnetic holes, which they termed magnetic bubble layers (MBL), may be related to tearing mode instability driven by strong MP currents, and the smaller scale fluctuations represent Kinetic Alfvén Waves (KAW). They claimed that these KAWs were driven by macroscopic pressure and magnetic field gradients via Hall instability. Along with the strong depressions (98%) in the ambient magnetic field, characteristics of their MBL was as follows; (i) enhanced convective flow, $v_E = \mathbf{E} \times \mathbf{B}/\mathbf{B^2}$ which was highly variable (50-300 km/s), compared to the MSH flow (ii) higher energy ion and electrons, about twice their initial energy, (iii) the region inside the magnetic bubble island is hotter than the outside region, (iv) region of highest pressure and temperature was at the center of the magnetic bubble, (iv) mirror instability condition not fulfilled, (v) strong correlation

between two orthogonal components B_Z and E_Y which is characteristic of Alfvén waves, (vi) magnetic fluctuations were enhanced near the bubble boundary (vii) fluctuations due to hall instability was largest at the bubble boundary. They explained that the energized plasma in these holes were due to turbulance caused by KAWs.

While we do not have the ability to verify all these features, some of them are present in our case. We show Alfvénicity through the perpendicular components of the field and flow perturbations modified by $\sqrt{\mu_0 \rho}$. The background magnetic field was derived by smoothing the data. We find that for all three components, the perpendicular perturbation in velocity and magnetic field were out of phase with each other (not shown), i.e., the KAW are travelling along the magnetic field. The correlation coefficient in the X,Y,Z directions were -0.76, -0.83 and -0.75 respectively. These are good indications of Alfvénicity.

In addition, we considered length scales. The ion thermal gyroradius is proportional to the square root of the temperature and inversely proportional to the magnetic field. Taking the average magnetic field in the MD to be 20 nT and temperature to be 3.5×10^6 K (Figure 5-6), the ion gyroradius will be in the order of 10^4 km. We assume the MD structure is convecting with the flow of ~80 km/s. Observations show that the duration of the hole is on average $\sim$ 40 s. A rough estimate of the size of an MD would be in the order of a few times 10^3 km. Therefore the size of the MD would be in the same order or less than the ion gyroradius.

5.7.2 Future Work

This example will be submitted for publication. To do so, we have to strengthen the consideration related to the generating mechanisms to arrive at a more solid conclusion. Future work would be to use high resolution data including electric field measurements. This will allow us to consider the solition and KH mechanisms in more detail. This work

can be done by using data from the Magnetospheric Multiscale Mission (MMS) [*Burch et. al.*, 2016].

Chapter 6

Summary

6.1 Summary of Key Results

Asymmetries in density and magnetic field along with the presence of a guide field cause several structural deviations from the well accepted symmetric reconnection geometry. The outflow density, outflow speed, location of the X-line and S-line, structure of the Hall magnetic and electric field are some of the measurable quantities that are affected by the asymmetries. Motivated by the fact that the high latitude poleward of the cusp region presents a wide spectrum of asymmetries as well as guide fields, and is a less examined area of the MSP in the context of reconnection, we investigated MP crossings made by the Cluster spacecraft from 2001 to 2008 as well as in one Polar crossing in this specific region.

We identified a collection of 18 reconnection events at high latitudes poleward of the cusp that fulfilled three or more IDR criteria in Chapter 2. This included five crossings with jet reversals. The density asymmetry of these events ranged from 1 to 3 orders of magnitude. All simulations so far only consider a density asymmetry of 10. This study proves that it is important to consider large density asymmetries in future simulations. Guide field ranged from 6% to 74% of the reconnecting MSH magnetic field. Near the current sheet crossings, the total DC electric field ranged from 10 mVm to 72 mV/m. The minimum magnetic shear in the events was 117^o while the maximum was 174^o (almost anti-parallel). The adiabatic

parameter δ_i rose above unity in 12 out of 18 events (one of the events had no electric field data to calculate δ_i.)

We compared measured values against predictions of *Cassak and Shay* [2007, 2009]'s scaling relations. These scaling relations were derived with antiparallel magnetic fields, i.e., magnetic shear of 180^o. Hence, we chose crossings with magnetic shear greater than 150^o and compared measured outflow density and outflow jet speed with predictions (equation 1.3 and 1.4). The measured peak of the outflow density during the reconnection jet matched predictions better than the average value. Similarly, the outflow jet peak values scaled with predicted values. The average of both quantities fell below the predicted value. In cases with jet reversals, while *Cassak and Shay* [2007,2009] did not make a distinction between the two outflow jets, this study shows that the faster jet matches predictions better.

Non co-location of the X-line and S-line in the exhaust was generally observed for all events. This was deduced by the separation of the B_L reversal and the density gradient. We picked the point in the density gradient where the inflow velocity, $V_N \sim 0$, to be the S-line. We calculated the separation distance for two events.

In Chapter 3, we presented Polar observations of a reconnection layer during an inbound pass at high northern latitudes. The interplanetary field of 20 nT pointed strongly northward continuously for 13 h. Reverse polar cap convection observed repeatedly by the DMSP F13 satellite provided direct evidence of continued reconnection. This event was hallmarked by a density asymmetry of 140. Disturbances in fields and plasma were much more intense on the MSP side of the current sheet. The intense electric field fluctuations ($\geq$60 mV/m) were mainly in the component normal to the current sheet, E_N. A density cavity was observed at both separatrices. Isolated E_N peaks were observed at the density cavity regions.

Polar crossed the IDR on one side of the X-line, and observed sunward and southward

jets that were biased towards the MSP side of the current sheet. The field reversal at the CS occurred before the outflow jet, which we argue to be due to the large density asymmetry. The stagnation line was strongly shifted toward the MSP side of the CS. We compared observations with simulations which emphasize the density asymmetry and which also include a guide field, and found good agreement. Remaining discrepancies may be explained by a density asymmetry much larger than in simulations. This was to our knowledge the first study of a high-latitude reconnection layer with (1) a large density asymmetry and (2) steady and continuously strong interplanetary B_Z.

We considered effects of a guide field on the Hall field structure in Chapter 4 using five Cluster crossings from our events table. First, using two events with jet reversals and a guide field of 26% of the reconnecting $B_{L,MSH}$ we were able to study both sides of the X-line. The measured out-of-plane B_M is a superposition of the Hall field B_H and the guide field B_G. We observed that the B_M component near the CS crossing matched the expected polarity produced in 2D PIC simulations by *Pritchett and Mozer*, [2009]. The positive guide field in both case studies weakened the Hall field in the sunward outflow region and enhanced the tailward outflow region giving rise to sunward-tailward asymmetry about the X-line. Furthermore, we showed clear evidence that due to an electron velocity shear layer at the vicinity of the X-line, on the 'enhanced' side of the X-line, the Hall field was weakened and changed polarity. This feature was predicted in the simluations.

The expected Hall electric field E_N configuration was observed in the data. E_N was stronger on the MSP side and was directed towards the MSH. The outflow speed was much higher on the 'enhanced' side of the X-line, and the peak was localized towards the MSP separatrix. In agreement with the 2D simulation, the outflow jet on the 'weakened' side was weaker and measured for a longer duration in both case studies, indicating that the jet filled the entire outflow region.

Next, we picked out three Cluster crossings of one (enhanced) side of the X-line. These events had a large guide field in the range of 60-75% and small density asymmetries so as to isolate the effects of the guide field. We normalized the peaks in B_M with B_0 (average of the two reconnecting fields). Simulations with a larger guide field (100%) produced an enhacement of 90% of B_0 in B_M. We measured an enhancement of $\sim$40-60% in B_M showing consistency with asymmetric simulation studies with a guide field.

In Chapter 5, we presented a detailed study of three encounters of prominent magnetic depresssions (MDs) by the Cluster-1 spacecraft in the MSH boundary layer close to the separatrix with focus on the distinctive characteristics that were measured. A density rise is expected in most magnetic nulls but this was not the case in this event. The magnetic field decreased up to 99% from the ambient magnetic field at these MDs. Ion temperature rose by a factor of three and was isotropic at the center. The electron flux showed enhancements in all direction inside the MDs, and was most pronounced in the parallel direction indicating that most energetic electrons were field aligned. Simultaneously C3, tailward of C1, observed a long (6 minutes) burst of sunward and northward flow.

We compared the observed features with several possible generating mechanisms to understand a possible cause for such large magnetic depressions in the MSHBL. We considered magnetic mirror mode waves, Kelvin Helmholtz waves, solitons and kinetic Alfvén waves as possibilities. The lack of electric field during the event was a strong constraint for us to arrive at a solid conclusion. We concluded that the kinetic Alfvén waves seemed most plausible with available data. However, other events with the distinctive characteristics listed requires further analysis with high resolution data such as those obtained by MMS.

6.2 Future Work

For future work, we propose investigating properties of the DR in the presence of velocity shear. Velocity shear becomes significant in reconnection events occuring at high latitudes poleward of the cusp region. This is mainly due to bulk flow patterns of the MSH. When the upstream MSH bulk plasma flows around the MP, it gains a potentially sizable component parallel or antiparallel to the reconnecting magnetic field [*Gosling et al.,* 1991; *Fuselier et al.,* 2000], which in turn sets up a flow shear across the MP. In contrast, at the subsolar point, the flow is predominantly not aligned to the MSH magnetic field and is minimal; the bulk flow is out of the reconnection plane.

In symmetric reconnection in the presence of a velocity shear, the speed of the outflow jets due to reconnection scales with the local upstream Alfvén speed [e.g., *Sonnerup et al.,* 1990]. Previous classical models suggest that, in order for stable reconnection to occur, i.e., with a stationary X-line, where the reconnecting magnetic field goes to zero, the MSH flow speed at poleward of the cusp, v_{MSH} should be sub-Alfvénic. If the flow is super-Alfvénic, the X-line must propagate tailward, such that, in the frame of reference of the reconnection site, the flow is still sub-Alfvénic [*Cowley and Owen*, 1989; *Gosling et al.,* 1991]. In this model, if v_{MSH} is more than double the MSH Alfvén speed, $c_{A,MSH}$, reconnection could not occur.

The presence of a flow shear, slows down the reconnection process or even stops it completely. It has been shown analytically and numerically using MHD models that a super-Alfvénic flow shear completely suppresses reconnection, while reconnection continued to occur for sub-alfvénic flow shear [*Mitchell and Kan*, 1978; *Chen and Morrison*, 1990; *La Belle-Hamer et al.*, 1994]. Additionally, outflow speed [*Cassak,* 2011] and reconnection rate is shown to decrease in events with sub-Alfvénic flow shear [*Chen et al.,* 1997; *Li and Ma*, 2010; *Faganello et al.,* 2010; *Cassak and Otto,* 2011; *Voslion et al.,* 2011; *Zhang et al.,* 2011;

Wu et al., 2013].

Improvements to the existing theories brought about by the addition of density and magnetic field asymmetries, in addition to the flow shear, have been recently examined by *Doss et al., 2015*. In an antiparallel 2D asymmetric magnetic reconnection scenario, *Doss et al., 2015*, performed a theoretical analysis to predict 3 specific features related to the DR, using arbitrary reconnecting magnetic field strengths, densities, and upstream flow speeds. The speed at which the isolated X-line is convected by the flow, the reconnection rate, and the critical flow speed at which reconnection was suppressed were calculated under several assumptions. They also confirmed their results with two-fluid numerical simulations.

The features of the DR under asymmetric conditions discussed in previous chapters did not consider an upstream flow parallel or anti-parallel to the reconnecting magnetic field. However, since this becomes critical at high-latitudes, broadening the current study to include this external effect is important. Additionally, comparisons to other work that includes a guide field on top of a velocity shear by *Tanaka et al.,* [2010] would be a further extention to this study. Comparing such theoretical and simulation predictions with high resolution data from MMS is reserved for future work.

Bibliography

André, M., A. Vaivads, S. C. Buchert, A. N. Fazakerley, and A. Lahiff (2004), Thin electron-scale layers at the magnetopause, *Geophys. Res. Lett.*, *31*, L06502, doi:10.1029/2003 GL019252.

Aubry, M. P., C. T. Russell, and M. G. Kivelson (1970), Inward motion of the magnetopause before a substorm *J. Geophys. Res.*, *75*, 34.

Avanov, L.A., V.N. Smirnov, J. H. Waite, S. A. Fuselier, and O. L. Vaisberg (2001), High-latitude magnetic reconnection in sub-Alfvénic flow: Interball Tail observations on May 29, 1996. *J. Geophys. Res.*, *106*, doi: 10.1029/2000JA000460.

Axford, W. I. (1984) Magnetic Field Reconnection, in Magnetic Reconnection in Space and Laboratory Plasmas (ed E. W. Hones), American Geophysical Union, Washington, D. C., doi: 10.1029/GM030p0001

Balogh, A., C. M. Carr, M. H. Acuna, M. W. Dunlop, T. J. Beek, P. Brown, K. H. Fornacon, E. Georgescu, K. H. Glassmeier, J. Harris, G. Musmann, T. Oddy, and K. Schwingenschuh (2001), The cluster magnetic field investigation: overview of in-flight performance and initial results, *Ann. Geophys.*, *19*, 1207–1217.

Baumgärtel, K. (1999), Soliton approach to magnetic holes, J. Geophys. Res., 104(A12), 28295–28308, doi:10.1029/1999JA900393.

Birn, J., et al. (2005), Forced magnetic reconnection, *J. Geophys. Res.*, *32*, L06105, doi:10.1029/2004GL022058.

Birn, J., M. Hesse, and K. Schindler (2006a), Entropy conservation in simulations of magnetic reconnection, *Phys. Plasmas*, *13*, 092117.

Birn, J., J. E. Borovsky, and M. Hesse (2008), Properties of asymmetric magnetic reconnection, *Phys. Plasmas*, *15*, 032101; doi: 10.1063/1.2888491092117.

Borovsky, J. E., M. Hesse,(2007), The reconnection of magnetic fields between plasmas with different densities: Scaling relations, *Phys. Plasmas*, *14*, 102309, doi: 10.1063/1.2772619

Birn, J., and E. Priest (2007), *Reconnection of magnetic fields*, Cambridge University Press, Cambridge.

Birn, J., J. E. Borovsky, M. Hesse, and K. Schindler (2010), Scaling of asymmetric reconnection in compressible plasmas, *Phys. Plasmas*, *17*,052108, doi:10.1063/1.3429676.

Burch, J. L., T. E. Moore, R. B. Torbert, B. L. Giles (2016), Magnetospheric Multiscale

overview and science objectives, *Space Sci. Rev.*, *199*, 5–21, doi:10.1007/s11214-015-0164-9.

Cassak, P. A., M. A. Shay (2007), Scaling of asymmetric magnetic reconnection: General theory and collisional simulations, *Phys. of Plasmas*, *14*, 102114.

Cassak, P. A., M. A. Shay (2009), Structure of the dissipation region in fluid simulations of asymmetric magnetic reconnection, *Phys. of Plasmas*, *16*, 055704.

Chen, L.-J., A. Bhattacharjee, P. A. Puhl-Quinn, H. Yang, N. Bessho, et al. (2007), Observation of energetic electrons within magnetic islands, *Nature, Physics*, doi:10.1038/nphys777.

Cowley, S. W. H., (1982), The causes of convection in the Earth's magnetosphere: A review of developments during IMS, *Rev. Geophys.*, *20*, 531-565.

Cowley, S. W. H., (1984), Evidence for the occurrence and importance of reconnection between the Earths magnetic field and the interplanetary magnetic field, in: AGU Geophysical Monograph 30, edited by: Hones, E. W., 375–378, American Geophysical Union.

Crooker, N. U., Dayside merging and cusp geometry, *J. Geophys. Res.*, *84*, 951, 1979.

Crooker, N. U., (1992), Reverse convection, *J. Geophys. Res.*, *97*, A12, 19,363-19,372.

Deng, X. H., and H. Matsumoto (2001), Rapid magnetic reconnection in the Earth's magnetosphere mediated by whistler waves, *Nature*, *410*, 557.

Doss, C. E., C. M. Komar, P. A. Cassak, F. D. Wilder, S. Eriksson, and J. F. Drake (2015), Asymmetric magnetic reconnection with a flow shear and applications to the magnetopause, *J. Geophys. Res. Space Physics*, *120*, 7748–7763, doi:10.1002/2015JA021489.

Drake, J. F., M. Swisdak, H. Che, and M. A. Shay (2006), Electron acceleration from contracting magnetic islands during reconnection, *Nature*, *443*, doi:10.1038/nature05116.

Dungey, J. W., (1961), Interplanetary magnetic field and auroral zones, *Phys. Rev. Lett.*, *6*, 47.

Dungey, J. W., (1963),The structure of the exosphere or adventures in velocity space, in *Geophysics, The Earth's Environment*, edited by C. DeWitt et al., 526, Gordon and Breach, New York.

Eastwood, J. P., T.D. Phan, F. S. Mozer, M. A. Shay, M. Fujimoto, et. al. (2007), Multipoint observations of the Hall electromagnetic field and secondary island formation during magnetic reconnection, *J. Geophys. Res.*, *112*, A06235, doi:10.1029/2006JA012158.

Eastwood, J. P., T.D. Phan, F. S. Mozer, M. A. Shay, M. Fujimoto, et. al., (2010), Average properties of the magnetic reconnection ion diffusion region in the Earth's magnetotail: The 2001–2005 Cluster observations and comparison with simulations, *J. Geophys. Res.*, *115*, A08215, doi:10.1029/2009JA014962.

Eastwood, J.P., T. D. Phan, M. Øieroset, M. A. Shay, K. Malakit, et. al. (2013), Influence

of asymmetries and guide fields on the magnetic reconnection D in collisionless space plasmas, *Plasma Phys. Control. Fusion*, *55*,124001, doi:10.1088/0741-3335/55/12/124001.

Escoubet, C. P., A. Pedersen, R. Schmidt, and P. A. Lindqvist (1997), Density in the magnetosphere inferred from ISEE 1 spacecraft potential, *J. Geophys. Res.*, *102*, A8, 17595–17609, doi:10.1029/97JA00290.

Escoubet, C. P., M. Fehringer, and M. Goldstein (2001), The Cluster Mission, *Ann. Geophys.*, 19, 1197–1200, doi:10.5194/angeo-19-1197-2001.

Fairfield, D. H., and L. J. Cahill Jr. (1966), Transition region magnetic field and polar magnetic disturbances, *J. Geophys. Res.*, *71*, 1, 155–169, doi:10.1029/JZ071i001p00155.

Fairfield, D. H., and J. D. Scudder (1985), Polar rain: solar coronal electrons inthe earth's magnetosphere, *J. Geophys. Res.*, *90*, A5, 4055-4068.

Fujimoto, M., M. S. Nakamura, I. Shinohara et al. (1997), Observations of earthward streaming electrons at the trailing boundary of a plasmoid, *Geophys. Res. Lett.*, *24*, 2893, doi:10.1029/97GL02821.

Fuselier, S. A., K. J. Trattner, S. M. Petrinec, C. J. Owen, and H. Rème (2005), Computing the reconnection rate at the Earth's magnetopause using two spacecraft observations, *J. Geophys. Res.*, *110*, A06212, doi:10.1029/2004JA010805.

Giovanelli, R. G. (1946), A Theory of Chromospheric Flares, *Nature*, *158*, 81–82.

Gonzalez, W. D., F. S. Mozer (1974), A quantitative model for the potential resulting from reconnection with an arbitrary interplanetary magnetic field, *J. Geophys. Res.*, *79*, 28, 4186-4194.

Gonzalez, W. D., and E. Parker (2016), Magnetic Reconnection, Concepts and Applications, *Astrophysics and Space Science Library*, Springer International Publishing, *427*, doi:10.1007/978-3-319-26432-5.

Gosling, J. T., M. F. Thomsen, S. J. Bame, and R. C. Elphic (1991), Observations of reconnection of interplanetary and lobe magentic field lines at the high-latitude magentopause, *J. Geophys. Res.*, *96*, 14,097.

Gosling, J. T., M. F. Thomsen, G. Le, and C. T. Russell (1996), Observations of magnetic reconnection at the lobe magnetopause, J. *Geophys. Res.*, *101*, 24,765-24,773.

Gosling, J. T., R. M. Skoug, D. K. Haggerty, and D. J. McComas (2005), Absence of energetic particle effects associated with magnetic reconnection exhausts in the solar wind, *Geophys. Res. Lett.*, *32*, L14113, doi:10.1029/2005GL023357.

Gosling, J. T. (2007), *Encyclopedia of the Solar System (Second Edition)* by L. McFadden, T. Johnson, P. Weissman, *Academic Press*, 99-116.

Gustafsson, G., R. Boström, B. Holback, G. Holmgren, A. Lundgren, K. Stasiewicz, et. al.(1997), The electric field and wave experiment for the cluster mission, *Space Sci.*

Rev., *79*, 137–156.

Haaland, S.E., B U ́O Sonnerup, M W Dunlop, A Balogh, E Georgescu, H Hasegawa, B Klecker, G Paschmann, P Puhl-Quinn, H Rème, H Vaith, and A. Vaivads (2004). Four-spacecraft determination of magnetopause orientation, motion and thickness: com- parison with results from single-spacecraft methods. *Annales Geophysicae*, *22*, 4, 1347–1365.

Harvey, P., et al. (1995), The Electric Field Instrument on the Polar satellite, *Space Sci. Rev.*, *71*, 583.

Heelis, R. A., P. H. Reiff, J. D. Winningham, and W. B. Hanson (1986), Ionospheric convection signatures observed by De 2 during northward interplanetary magnetic field, *J. Geophys. Res.*, *91*, A5, 5817–5830, doi:10.1029/JA091iA05p05817.

Hesse, M., and K. Schindler (1988), A theoretical foundation of general magnetic reconnection, *J. Geophys. Res.*, *93*, A6, 5559–5567, doi:10.1029/JA093iA06p05559.

Hudson, P. D., (1970), Discontinuities in an anisotropic plasma and their identification in the solar wind, *Planet. Space Sci.*, *18*, 1611–1622.

Johnstone, A. D., C. Alsop, S. Burge, P. J. Carter, A. J. Coates, A. J. Coker, A. N. Fazakerley, M. Grande, R. A. Gowen, C. Gurgiolo, B. K. Hancock, B. Narheim, A. Preece, P. H. Sheather, J. D. Winningham, and R. D. Woodliffe (1997), Peace: A plasma electron and current experiment, *Space Sci. Rev.*, *79*, 1-2, 351–398, doi:10.1023/A:1004938001388.

Kessel, R. L., S.H. Chen, J. L. Green, S. F. Fung, S. A. Boardsen, et. al. (1996), Evidence of high-latitude reconnection during northward IMF: Hawkeye observations, *Geophys. Res. Lett.*, *23*, 583-586.

Khrabrov, A. V., and B. U. Ö. Sonnerup (1998), Orientation and motion of current layers: Minimization of the faradary residue, *Geophys. Res. Lett.*, *25*, 13, 2373, doi:10.1029/98GL51784.

Khotyaintsev, Yu. V., A. Vaivads, A. Retinó, M. Andrè et al. (2006), Formation of Inner Structure of a Reconnection Separatrix Region, *Phys. Rev. Lett.*, doi:10.1103/PhysRevLett.97.205003

Kleva, R. G., J. F. Drake, and F. L. Waelbroeck (1995), Fast reconnection in high temperature plasmas, *Physics of Plasmas*, *2*, 23-34, doi:10.1063/1.871095.

Lepping, R. P., et al. (1995), The Wind magnetic field investigation, *Space Sci. Rev.*, *71*, 207.

Levy, R. H., H.E. Petschek, and G. L. Siscoe (1964), Aerodynamic Aspects of the Magnetospheric Flow, *AIAA Journal*, *2*, 12.

Lopez, R. E., (1987), Solar cycle invariance in solar wind proton temperature relationships, *J. Geophys. Res.*, *92*, A10, 11, 189-11, 194.

Luhmann, J. G., R. J. Walker, C. T. Russell, N. U. Crooker, J. R. Spreiter, and S. S. Stahara (1984), Patterns of potential magnetic field merging sites on the dayside magnetopause, *J. Geophys. Res.*, *89*, A3, 1739 – 1742, doi: 10.1029/JA089iA03p01739.

Lybekk, B., A. Pedersen, S. Haaland, K. Svenes, A. N. Fazakerley, A. Masson, M. G. G. T. Taylor, and J.-G. Trotignon (2012), Solar cycle variations of the cluster spacecraft potential and its use for electron density estimations, *J. Geophys. Res.*, *117*, A01217, doi:10.1029/2011JA016969.

Maezawa, K., (1976), Magnetospheric convection induced by the positive and negative Z components of the interplanetary magnetic field' quantitative analysis using polar cap magnetic records, *J. Geophys. Res.*, *81*, 2289-2303.

Malakit, K., M. A. Shay, P. A. Cassak, and C. Bard (2010), Scaling of asymmetric magnetic reconnection: Kinetic particle-in-cell simulations, *J. Geophys. Res.*, *115*, A10223, doi:10.1029/2010JA015452.

Marklund, G. T., L. G. Blomberg, C. G. Fälthammar, R. E. Erlandson, and T. A. Potemra (1990), Signatures of the high-altitude polar cusp and dayside auroral regions as seen by the Viking electric field experiment, *J. Geophys. Res.*, *95*, 5767–5780, doi:10.1029/JA095iA05p05767.

Maynard, N. C., C. J. Farrugia, W. J. Burke, D. M. Ober, F. S. Mozer, H. Rème, M. Dunlop and K. D. Siebert (2012), Cluster observations of the dusk flank magnetopause near the sash: Ion dynamics and flow-through reconnection, *J. Geophys. Res., 117*, A10201, doi:10.1029/2012JA017703, 2012.

McComas, D. J., S. J. Bame, P. Barker, W. C. Feldman, J. L. Phillips, P. Riley, and J. W. Griffee (1998), Solar Wind Electron Proton Alpha Monitor (SWEPAM) for the Advanced Composition Explorer, *Space Science Reviews*, *86*, 563-612.

Mozer, F. S., S. D. Bale, and T. D. Phan (2002), Evidence of Diffusion Regions at a Subsolar Magnetopause Crossing, *Phys. Rev. Lett*, *89*, 015002, doi:10.1103.

Mozer, F. S., and A. Retinò (2007), Quantitative estimates of magnetic field reconnection properties from electric and magnetic field measurements, *J. Geophys. Res.*, *112*, A10206, doi:10.1029/2007JA012406.

Mozer, F. S., V. Angelopoulos, J. Bonnell, K. H. Glassmeier, and J. P. McFadden (2008a), THEMIS observations of modified Hall fields in asymmetric magnetic field reconnection, *Geophys. Res. Lett.*, *35*, L17S04, doi:10.1029/2007GL033033.

Mozer, F. S., P. L. Pritchett, J. Bonnell et al. (2008b), Observations and simulations of asymmetric magentic field reconnection, *J. Geophys. Res.*, *113*, A00C03, doi:10.1029/2008JA013535.

Muzamil, F. M., C. J. Farrugia, R. B. Torbert, P. R. Pritchett, F. S. Mozer, J. D. Scudder, C. T. Russell, P. E. Sandholt, W. F. Denig, and L. Wilson III (2014), Structure of a reconnection layer poleward of the cusp: Extreme density asymmetry and a guide field, *J. Geophys. Res. Space Physics*, *119*, 7343–7362, doi:10.1002/2014JA019879.

Nagai, T., I. Shinohara, M. Fujimoto et al. (2001), Geotail observations of the Hall current system: Evidence of magnetic reconnection in the magnetotail, *J. Geophys. Res.*, *106*, 25,929, doi:10.1029/2001JA900038.

Nakamura, M., M. Scholer (2000), Structure of the magnetopause reconnection layer and of flux transfer events: Ion kinetic effects, *J. Geophys. Res.*, *105*, A10, 23179-23191.

Nykyri, K. and A. Otto (2001), Plasma transport at the magnetospheric boundary due to reconnection in Kelvin-Helmholtz vortices, *Geophys. Res. Lett.*, *28*, 3565–3568, doi:10.1029/2001GL013239.

Ogilvie, K. W., et al. (1995), SWE, A comprehensive plasma instrument for the Wind spacecraft, *Space Sci. Rev.*, *71*, 55.

Øieroset, M., T. D. Phan, M. Fujimoto, R. P. Lin and R. P. Lepping (2001), In situ detection of collisionless reconnection in the Earth's magnetotail, *Nature*, *412*, 414-417.

Onsager, T. D., J.D. Scudder, M. Lockwood, and C. T. Russel4 (2001), Reconnectionat the high-latitude magnetopause during northward interplanetary magnetic field conditions, *J. Geophys. Res.*, *106*, A11, 25,467–25,488.

Parker, E. N. (1957), Sweet's mechanism for merging magnetic fields in conducting fluids, *J. Geophys. Res.*, *62*, 4, 509–520.

Parker, E. N. (1963), The Solar-Flare Phenomenon and the Theory of Reconnection and Annihiliation of Magnetic Fields, Astrophysical Journal Supplement, *8*, 177, doi:10.1086/190087.

Paschmann, G., B. U. *Ö*. Sonnerup, I. Papamastorakis et al. (1979), Plasma acceleration at the Earth's magnetopause: evidence for reconnection, *Nature*, *282*, 5736, 243-246.

Paschmann, G., W. Baumjohann, N. Sckopke et al. (1986), The magnetopause for large magnetic shear – AMPTE/IRM observations, *J. Geophys. Res.*, *91*, 11 099–11 115.

Paschmann, G., J M Quinn, R B Torbert, H Vaith, C E McIlwain, G Haerendel, O H Bauer, T Bauer, W Baumjohann, W Fillius, M F örster, S Frey, E Georgescu, S S Kerr, C A Kletzing, H Matsui, P Puhl-Quinn, and E C Whipple (2001),The Electron Drift Instrument on Cluster: overview of first results, *Annales Geophysicae*, *19*, 10/12, 1273–1288, doi: 10.5194/angeo-19-1273-2001.

Pedersen, A., B. Lybekk, M. Andre, A. Eriksson, A. Masson, F. S. Mozer, P.-A. Lindqvist, P. M. E. Decreau, I. Dandouras, J. A. Sauvaud, A. Fazakerley, M. Taylor, G. Paschmann, K. R. Svenes, K. Torkar, and E. Whipple (2008), Electron density estimations derived from spacecraft potential measurements on cluster in tenuous plasma regions, *J. Geophys. Res.*, 113, A07S33, doi:10.1029/2007JA012636.

Petschek, H. E. (1964), in *AAS/NASA Symposium on the Physics of Solar Flares*, edited by W. N. Ness (NASA, Washington, DC, 1964), p. 425.

Phan, T., H. U. Frey, S. Frey, L. Peticolas, S. Fuselier et al. (2003), Simultaneous Cluster and IMAGE observations of cusp reconnection and auroral proton spot for northward IMF, *Geophys. Res. Lett.*, *30(10)*, 1509, doi:10.1029/2003GL016885.

Phan, T. D., J. F. Drake, M. A. Shay, F. S. Mozer, and J. P. Eastwood (2007), Evidence for an Elongated (60 Ion Skin Depths) Electron Diffusion Region during Fast

Magnetic Reconnection *Physical Review Letters*, *99*, 25, 255002, doi: 10.1103/PhysRevLett.99.255002.

Priest, E. R., and T. G. Forbes (2002), The magnetic nature of solar flares, *The Astronomy and Astrophysics Review*, *10*, 4,313–377, doi: 10.1007/s001590100013.

Pritchett, P. L., (2001), Geospace Environment Modeling magnetic reconnection challenge: Simulations with a full particle electromagnetic code, *J. Geophys. Res.*, *106*, A3, 3783–3798.

Pritchett, P. L. (2008), Collisionless magnetic reconnection in an asymmetric current sheet, *J. Geophys. Res.*, *113*, A06210, doi:10.1029/2007JA012930.

Pritchett, P. L., and F. S. Mozer (2009), Asymmetric magnetic reconnection in the presence of a guide field, *J. Geophys. Res.*, *114*, A11210, doi:10.1029/2009JA014343.

Pritchett, P. L. (2013),The influence of intense electric fields on three-dimensional asymmetric magnetic reconnection, *Phys. of Plasmas*, *20*, 061204, doi: 10.1063/1.4811123.

Reiff, P. H. (1982), Sunward convection in both polar caps, *J. Geophys. Res.*, *87*, A8, 5976-5980, doi: 10.1029/JA087iA08p05976.

Reiff, P. H., T. W. Hill, and J. L. Burch (1977), Solar wind plasma injection at the dayside magnetospheric cusp, *J. Geophys. Res.*, *82*, 4, 479–491, doi:10.1029/JA082i004p00479.

Rème, H., J. M. Bosqued, J. A. Sauvaud, A. Cros, J. Dandouras, C. Aoustin, J. Bouyssou et. al. (1997), The Cluster Ion Spectrometry (CIS) experiment, *Space Science Reviews*, *79*, 1, 303-350.

Rème, H., C. Aoustin, J. M. Bosqued, I. Dandouras, B. Lavraud, J. A. Sauvaud, A. Barthe, J. Bouyssou, T. Camus et. al. (2001), First multispacecraft ion measurements in and near the earth's magnetosphere with the identical Cluster Ion Spectrometry (CIS) experiment, *Ann. Geophys.*, *19*, 1303– 1354, doi:10.5194/angeo-19-1303-2001.

Retinò , A., M. B. Cattaneo, M. F. Marcucucci, A. Vaivads et al (2005), Cluster multispacecraft observations at the high-latitude duskside magnetopause: implications for continuous and component magnetic reconnection, *Ann. Geophys.*, *23*, 461-473.

Retinò , A., A. Vaivads, M. Andre, F. Sahraoui et al (2006), Structure of the separatrix region close to a magnetic reconnection X-line: Cluster observations , *Geophys. Res. Lett.*, *33*, L06101, doi:10.1029/2005GL024650.

Richardson, I. G., H.V. Cane (2010), Near-earth interplanetary coronal mass ejections during solar cycle 23 (1996 – 2009): Catalog and summary of properties, *Solar Phys*, *264*, 189–237, doi 10.1007/s11207-010-9568-6.

Rogers, B. N., R. E. Denton, J. F. Drake, and M. A. Shay (2001), Role of Dispersive Waves in Collisionless Magnetic Reconnection, *Phys. Rev. Lett.*, *87*, 195004, doi:10.1103/PhysRevLett.87.195004.

Russell, C. T., and R. C. Elphic (1978), Initial ISEE magnetometer results: magnetopause observations, *Space Sci. Rev.*, *22*, 681-715.

Russell, C. T., M. M. Mellott, E. J. Smith, and J. H. King (1983), Multiple spacecraft observations of interplanetary shocks: Four spacecraft determination of shock normals, *J. Geophys. Res. Space Physics*, *88*, A6, 4739–4748, doi: 10.1029/JA088iA06p04739.

Russell, C. T., R. C. Snare, J. D. Means, D. Pierce et al. (1995), The GGS/Polar magnetic fields investigation, in *The Global Geospace Mission*, ed. by C. T. Russell, p. 563, Kluwer Academic Publishers, Dordrecht.

Safrankova, J., Z. Nemecek, D. G. Sibeck et al. (1998), Two point observation of high latitude reconnection, *Geophys. Res. Lett.*, *25*,4301-4304.

Schindler, K., M. Hesse, and J. Birn (1988), General magnetic reconnection, parallel electric fields, and helicity, *J. Geophys. Res.*, *93*, A6, 5547–5557, doi:10.1029/JA093iA06p05547.

Schoeffler, K. M., J. F. Drake, and M. Swisdak (2001), The effects of plasma beta and anisotropy instabilities on the dynamics of reconnecting magnetic fields in the heliosheath, *The Astrophysical Journal*, *743*, 1, doi:10.1088/0004-637X/743/1/70.

Scudder, J. et al., (1995), Hydra- A 3-D electron and ion hot plasma instrument for the Polar spacecraft of the GGS mission, in The Global Geospace Mission, C.T. Russell, ed., p. 459 *J. Geophys. Res.*.

Scudder, J. D., R. D. Holdaway, R. Glassberg, and S. L. Rodriguez (2008), Electron diffusion region and thermal demagnetization, *J. Geophys. Res.*, *113*, A10208, doi:10.1029/2008JA013361.

Scudder, J., R. D. Holdaway, W. S. Daughton et al. (2012), First Resolved Observations of the Demagnetized Electron-Diffusion Region of an Astrophysical Magnetic-Reconnection Site, *Physical Rev. Lett.*, *108*, doi: 10.1103/PhysRevLett.108.225005.

Shay, M. A., J. F. Drake, R. E. Denton, and D. Biskamp (1998), Structure of the dissipation region during collisionless magnetic reconnection, *J. Geophys. Res.*, *103*, 9165–9176.

Shinohara, I., and S. Kokubun (1996), Statistical properties of particle precipitation in the polar cap during intervals of northward interplanetary magnetic field, *J. Geophys. Res.*, *101*, A1, 69-82.

Smith, C. W., J. L'Heureux, N.F. Ness, M.H. Acuña, L.F. Burlaga and J. Scheifele (1998), The ACE Magnetic Fields Experiment, *Space Science Reviews*, *86*, 1, 613–632, doi:10.1023/A:1005092216668.

Song, P., and C. T. Russell (1992), Model of the formation of the low-latitude boundary layer for strongly northward interplanetary magnetic field, *J. Geophys. Res.*, *97*, 1411.

Sonnerup, B. U. *Ö.*, (1974), The Reconnecting Magnetosphere, in: ASSL Vol. 44, Magnetospheric Physics, 23–33, 1974.

Sonnerup, B. U. Ö., (1979), Magnetic Field Reconnection, in Solar System Plasma Physics Volume III, edited by L. T. Lanzerotti, C. F. Kennel, and E. N. Parker, 47– 108, Elsevier, New York.

Sonnerup, B. U. Ö., G. Paschmann, I. Papamastorakis et al (1981), Evidence for magnetic field reconnection at the earth's magnetopause, *J. Geophys. Res.*, *86*, A12, 10049-10067.

Song, P., and C. T. Russell, (1992), Model of the formation of the low-latitude boundary layer for strongly northward interplanetary magnetic field, *J. Geophys. Res.*, *97*, 1411-1420.

Soucek, J., E. Lucek, and I. Dandouras (2008), Properties of magnetosheath mirror modes observed by Cluster and their response to changes in plasma parameters, *J. Geophys. Res.*, *113*, A04203, doi:10.1029/2007JA012649.

Southwood, D., and Kivelson, M.G. (1993), Mirror instability. I - Physical mechanism of linear instability, *J. Geophys. Res.*, *98*, A6, 9181-9187.

Speiser, T. W. (1965), Particle trajectories in model current sheets: 1. analytical solutions, *J. Geophys. Res.*, *70*, 17, 4219–4226, doi:10.1029/JZ070i017p04219.

Stasiewicz, K., C. E. Seyler, F. S. Mozer, G. Gustafsson, J. Pickett and B. Popielawska (2001) Magnetic Bubbles and Kinetic Alfvén Waves in the High-Latitude Magnetopause Boundary, *J. Geophys. Res.*, *106*, A12, 29503–29514, doi:10.1029/2001JA900055.

Stasiewicz, K., P. K. Shukla, G. Gustafsson, S. Buchert, B. Lavraud, B. Thidé, and Z. Klos (2003), Slow Magnetosonic Solitons Detected by the Cluster Spacecraft, *Phys. Rev. Lett.*, *90*, 085002.

Swisdak, M., B. N. Rogers, J. F. Drake, and M. A. Shay, (2003), Diamagnetic suppression of component magnetic reconnection at the magnetopause, *J. Geophys. Res.*, *108*, A5, 1218, doi:10.1029/2002JA009726.

Szita, S., A. N. Fazakerley, P. J. Carter, A. M. James, P. Travnicek, et. al. (2001), Cluster peace observations of electrons of spacecraft origin, *Ann. Geophys.*, *19*, 1721–1730, doi:10.5194/angeo-19-1721-2001.

Tanaka, K. G., A. Retinò , Y. Asano, M. Fujimoto, I. Shinohara, A. Vaivads et al (2008), Effects on magnetic reconnection of a density asymmetry across the current sheet, *Ann. Geophys.*, *26*, 2471-2483.

Trattner, K. J., J. S. Mulcock, S. M. Petrinec, and S. A. Fuselier, (2007), Probing the boundary between antiparallel and component reconnection during southward interplanetary magnetic field conditions, *J. Geophys. Res.*, *112*, A08210, doi:10.1029/2007JA012270.

Treumann, R.A., L. Brostrom, J. LaBelle, N. Sckopke (1990), The plasma wave signature of a "magnetic hole" in the vicinity of the magnetopause *J. Geophys. Res.*, *95*, 19099-19114 doi:10.1029/JA095iA11p19099.

Tsurutani, B. T., E. J. Smith, R. R. Anderson, K. W. Ogilvie, J. D. Scudder, D. N.

Baker, and S. J. Bame (1982), Lion roars and nonoscillatory drift mirror waves in the magnetosheath, *J. Geophys. Res.*, *87*, A8, 6060–6072, doi:10.1029/JA087iA08p06060.

Tsurutani, B. T., G. S. Lakhina, O. P. Verkhoglyadova, E. Echer, F. L. Guarnieri et. al. (2011), Magnetosheath and heliosheath mirror mode structures, interplanetary magnetic decreases, and linear magnetic decreases: Differences and distinguishing features, *J. Geophys. Res.*, *116*, A02103, doi:10.1029/2010JA015913.

Turner, J. M., L. F. Burlaga, N. F. Ness, J. F. Lemaire (1977), Magnetic holes in the solar wind *J. Geophys. Res.*, *82*, 1921 - 1924, doi:10.1029/JA082i013p01921.

Twitty, C., T. D Phan, G. Paschmann et al. (2004), Cluster survey of cusp reconnection and its IMF dependence, *Geophys. Res. Lett.*, *31*, L19808, doi:10.1029/2004GL020646.

Vaivads, A., A. Retinò, M. André (2006), Microphysics of Magnetic Reconnection, *Space Science Reviews*, *122*, 19–27, doi: 10.1007/s11214-006-7019-3.

Vasyliunas, V. M. (1975), Theoretical models of magnetic field line merging, *Rev. Geophys.*, *13*, 1, 303–336, doi:10.1029/RG013i001p00303.

Wang, S., L. M. Kistler, C. G. Mouikis, and S. M. Petrinec (2015), Dependence of the dayside magnetopause reconnection rate on local conditions, *J. Geophys. Res. Space Physics*, *120*, 6386–6408, doi:10.1002/2015JA021524.

Wilder, F. D., S. Eriksson, K. J. Trattner, P. A. Cassak, S. A. Fuselier, and B. Lybekk (2014), Observation of a retreating x line and magnetic islands poleward of the cusp during northward interplanetary magnetic field conditions, *J. Geophys. Res. Space Physics*, *119*, 9643–9657, doi:10.1002/2014JA020453.

Winterhalter, D., M. Neugebauer, B. E. Goldstein, and E. J. Smith (1994), Ulysses field and plasma observations of magnetic holes in the solar wind and their relation to mirror-mode structures, *J. Geophys. Res. Space Physics*, *99*, A12, 23,371-23,381.

Wygant, J. R., et al. (2005), Cluster observations of an intense normal component of the electric field at a thin reconnecting current sheet the tail and its role in the shock-like acceleration of the ion fluid into the separatrix region, *J. Geophys. Res.*, *110*, A09206, doi:10.1029/2004JA010708.

Yamada, M. (1999), Review of controlled laboratory experiments on physics of magnetic reconnection, *J. Geophys. Res.*, *104*, A7, 14529–14541, doi:10.1029/1998JA900169.

Yamauchi, M., R. Lundin, L. Eliasson, and O. Norberg (1996), Meso-scale structures of radiation belt/ring current detected by low-energy ions, *Adv. Space Res.*, *17*, 2, 171–174, doi: 10.1016/0273-1177(95)00531-I.

Zakharov, L. and B. Rogers (1992), Two-fluid magnetohydrodynamic description of the internal kink mode in tokamaks, *Physics of Fluids B: Plasma Physics*, *4*, 10, 3285-3301, doi:10.1063/1.860384.